

Combined Electromagnetic Suspension and Propulsion for Positioning with sub-Micrometer Accuracy

Y. H. CHAN,
S. C. CHAN,
S. C. CHAN

Department of Mechanical Engineering

The Hong Kong Polytechnic University

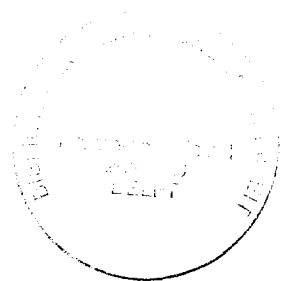
Combined Electromagnetic Suspension and Propulsion for Positioning with sub-Micrometer Accuracy

PROEFSCHRIFT

ter verkrijging van de graad van doctor,
aan de Technische Universiteit Delft,
op gezag van de Rector Magnificus Prof. ir. K.F. Wakker,
in het openbaar te verdedigen ten overstaan van een commissie,
door het College van Dekanen aangewezen,
op maandag 27 november 1995 te 10.30 uur

door Frank AUER
werktuigkundig ingenieur

geboren te Leimuiden



Dit proefschrift is goedgekeurd door de promotor:
Prof. dr. ir. H.F. van Beek

Samenstelling promotiecommissie:

Rector Magnificus, voorzitter
Prof. dr. ir. H.F. van Beek, TU Delft, promotor
Prof. dr. ir. M.P. Koster, U-Twente
Prof. dr. ir. O.H. Bosgra, TU Delft
Prof. dr. ir. P. Kruit, TU Delft
Prof. dr. ir. K. van der Werff, TU Delft
Dr. ir. J. van Eijk, Philips CFT
Prof. ir. H.A. Crone, TU Delft

Published and distributed by:

Delft University Press
Stevinweg 1
2628 CN Delft
The Netherlands

Telephone + 31 15 2783254
Fax + 31 15 2781661

CIP-DATA KONINKLIJKE BIBLIOTHEEK, DEN HAAG

Auer, F.

Combined Electromagnetic Suspension and Propulsion for Positioning with sub-Micrometer Accuracy / F. Auer. - Delft : Delft University Press. - III.

Thesis Delft University of Technology. - With ref. - With summary in Dutch.

ISBN 90-407-1193-3

NUGI 841

Keywords: Active Magnetic Bearing (AMB) / Linear Motor / sub-Micrometer Accuracy

Copyright © 1995 by F. Auer

All rights reserved.

No part of the material protected by this copyright notice may be reproduced or utilized in any form or by any means, electronic or mechanical, including photocopying, recording or by any information storage and retrieval system, without permission from the publisher: Delft University Press, Stevinweg 1, 2628 CN Delft, The Netherlands.

Printed in The Netherlands

LIST OF SYMBOLS	IX
1 INTRODUCTION	1
1.1 High accuracy positioning and guiding	1
1.1.1 Static errors	3
1.1.2 Dynamic errors	5
1.2 Goal of this research	8
1.3 Layout of this thesis	10
2 MAGNETIC SUSPENSION AND PROPULSION	13
2.1 Introduction	13
2.2 History of and trends in magnetic bearings	13
2.3 History and state of the art of linear electro-motors	15
2.4 Classification of magnetic forces	17
2.5 Selection of the forces and their implementation in the SPU	21
3 MAGNETIC SUSPENSION	25
3.1 Introduction	25
3.2 Theoretical model of the reluctance force	25
3.3 Theoretical background of the magnetic bearing actuator	28
3.4 Stabilization of magnetic bearings	32
3.5 Accuracy analysis of the magnetic reluctance force	39
3.5.1 Relative Permeability of air	39
3.5.2 Number of windings	39
3.5.3 Cross-sectional area of the magnetic pole	39
3.5.4 The current	40
3.5.5 Magnetic flux paths	41
3.6 Practical limitations of the magnetic reluctance force of the SPU	43
3.6.1 Maximum magnetomotive force	43
3.6.2 Maximum magnetic field density	47
3.7 Magnetic properties of materials for magnetic bearings	48
3.8 Linearization methods for magnetic bearings	53

3.9	Performance limitations of magnetic bearings	55
3.9.1	Static bearing load capacity	55
3.9.2	Static and dynamic stiffness	56
3.9.3	Damping	56
3.9.4	Position accuracy	56
4	MAGNETIC PROPULSION	59
4.1	Introduction	59
4.2	The Lorentz force	60
4.3	Secondary coil position within the SPU	61
4.4	Stabilization of the propulsion system	65
4.5	Accuracy analysis of the Lorentz force	66
4.5.1	Length of the current carrying conductor	67
4.5.2	Number of secondary windings	67
4.5.3	Primary currents and air-gaps	67
4.6	Mutual interaction between suspension and propulsion	68
4.6.1	The influence of the propulsion on the suspension	68
4.6.2	The influence of the suspension on the propulsion	69
4.7	Practical limitations to the propulsion force of the SPU	70
5	SPU COMPONENTS	75
5.1	Introduction	75
5.2	Position sensors	76
5.2.1	Inductive sensors	77
5.2.2	Eddy current sensors	78
5.2.3	Capacitive sensors	79
5.2.4	Optical sensors	81
5.3	Form standards	84
5.4	Sensor-less magnetic bearing	86
5.5	Overview of sensors	87
5.6	Power amplifiers	89
5.6.1	Linear amplifiers	92
5.6.2	Switching power amplifiers	93
5.7	Digital control	95

6	SUSPENSION AND PROPULSION UNIT: THE EXPERIMENTAL SET-UP	99
6.1	Introduction	99
6.2	Design of the experimental set-up	99
6.3	Mathematical model	102
6.4	Controller design	105
6.5	Simulation and measurement results	106
6.6	Propulsion	110
6.7	Experimental results of the propulsion force	111
7	APPLICATION OF THE SPU: 6 DEGREES OF FREEDOM PROPULSION AND SUSPENSION	113
7.1	Introduction	113
7.2	Experimental set-up	114
7.3	Dynamic equations of motion	117
7.4	Sensor system layout	119
7.5	Control of the six degrees of freedom	120
7.6	Measurement results for the suspension	122
7.7	Measurement results for the propulsion	127
8	SCALING FACTORS AND DESIGN RULES	135
8.1	Introduction	135
8.2	Scaling factors for the SPU	135
8.2.1	Geometric scaling factors	135
8.2.2	Electric circuit scaling factors	136
8.2.3	Magnetic circuit scaling factors	138
8.2.4	Control scaling factors	139
8.2.5	Overview of the scaling laws	140
8.3	Mechanical design rules for the SPU	141
8.3.1	Focus points	141
8.3.2	Rules for designing the SPU	141

9	CONCLUSIONS AND RECOMMENDATIONS	145
9.1	Conclusions	145
9.2	Recommendations	147
10	REFERENCES	149

APPENDICES

A: Mathematical derivation of the closed loop transfer functions	A.1
B: Placement of the integration action in the controller	B.1
C: Derivation of the transformation matrices	C.1

SUMMARY	S.1
---------	-----

SAMENVATTING	S.5
--------------	-----

ACKNOWLEDGEMENTS

CURRICULUM VITAE OF THE AUTHOR

List of Symbols

A	= cross-sectional area of central magnetic pole	[m ²]
A	= cross-sectional area of the sensor	[m ²]
B_{air}	= magnetic field density in the air-gap	[T]
B	= magnetic field density	[T]
b	= width of magnetic pole	[m]
C	= measured capacitance between two electrodes	[F]
d	= depth of magnetic pole	[m]
$d_{isolation}$	= thickness of isolation layer	[m]
E	= electric field	[V/m]
E_{lin}	= efficiency of the linear amplifier	[-]
f	= switching frequency	[Hz]
f_b	= closed-loop bandwidth	[Hz]
f_c	= loop-gain cross-over frequency	[Hz]
$F_{1,2,3}$	= suspension forces for all three SPU's	[N]
F_c	= gravity force	[N]
F_{ex}	= external forces	[N]
F_0	= premagnetization force	[N]
F_L	= Lorentz force	[N]
F_{lu}	= Lorentz force generated in upper air-gap	[N]
F_{ld}	= Lorentz force generated in lower air-gap	[N]

F_{mag1}	= magnetic force in upward direction	[N]
F_{mag2}	= magnetic force in downward direction	[N]
H_{air}	= magnetic field strength in the air-gap	[A/m]
$H_{z,\psi,\xi}$	= transfer functions for Z , ψ and ξ	[V/m]
$H_c(s)$	= controller transfer function	[V/V]
I	= current through coil	[A]
I_0	= primary coil stationary current	[A]
I_d	= lower primary coil current	[A]
I_u	= upper primary coil current	[A]
I_r	= current ripple	[A]
I_{sec}	= secondary coil current	[A]
$I_{z,\psi,\xi}$	= virtual currents for Z , ψ and ξ	[A]
$I_{x,y,\phi}$	= virtual currents controlling X , Y and Φ	[A]
J	= mass moment of inertia	[kgm ²]
J_{max}	= maximum current density	[A/m ²]
k	= thermal conductivity	[msK/J]
K_C	= force-displacement factor negative stiffness	[N/m]
K_{di}	= distance between integration and derivation	[-]
K_I	= force-displacement factor	[N/A]
K_m	= magnetic circuit constant	[Hm]
K_{mot}	= magnetic constant or motor constant	[N/A]
l	= length of the conductor inside the magnetic field	[m]
l_f	= force lever	[m]
l_{iron}	= the total length of the flux path in iron	[m]
L	= inductance	[H]
L_{supp}	= length of support lever	[m]
L_1	= length of sensor lever	[m]
L_2	= length of force lever	[m]

L_c	= length of center of gravity lever	[m]
m	= mass of the suspended rotor	[kg]
m	= mass of lever	[kg]
m	= mass of rotor	[kg]
M_c	= parasitic moment of gravity force	[Nm]
M_d	= lead action index	[-]
M_i	= lag action index	[-]
M_{magz}	= moment caused by magnetic fields	[Nm]
N	= number of primary windings	[-]
N_{sec}	= number of secondary windings	[-]
P	= proportional gain	[-]
p_1	= open-loop pole	[s ⁻¹]
p_2	= open-loop pole	[s ⁻¹]
Q	= charge	[C]
q_{copper}	= cross-sectional area of copper	[m ²]
q_{total}	= space occupied by one winding	[m ²]
r_{copper}	= copper radius	[m]
r_{total}	= total wire radius	[m]
R	= Ohmic resistance	[Ω]
s	= Laplace operator	[s ⁻¹]
S_d	= lower air-gap	[m]
S_u	= upper air-gap	[m]
S_o	= nominal air-gap	[m]
t	= time	[s]
T	= temperature	[°K]
v	= velocity of moving charge	[m/s]
v	= velocity of suspended object	[m/s]
V	= voltage	[V]

V_{supp}	= supply voltage	[V]
W	= magnetic energy	[W]
x	= position of the rotor	[m]
x_{sens}	= measured sensor position	[m]
x_1	= upper air-gap	[m]
x_2	= lower air-gap	[m]
β	= relative damping	[-]
ϵ	= permittivity	[F/m]
φ	= rotation	[rad]
Φ	= magnetic flux	[Wb]
τ_d	= derivative time constant	[s]
τ_i	= integration time constant	[s]
λ	= wavelength of light	[m]
$\mu_{r,air}$	= relative permeability of air	[-]
$\mu_{r,iron}$	= relative permeability of iron	[-]
μ_0	= permeability of vacuum	[H/m]
ρ	= specific resistance	[Ωm]
χ_m	= magnetic susceptibility	[-]

1 Introduction

1.1 High accuracy positioning and guiding

Positioning objects with sub-micrometer accuracy along a long range is one of the most demanding tasks in precision engineering. Not only must the positioning have high accuracy, but low friction and low (or no) wear of the guidance are also important. The guidance of the object along all degrees of freedom must be within the required limits of accuracy.

A good example of a sub-micrometer accuracy positioning system can be found with a wafer stepper. In a wafer stepper two perpendicular motions must be achieved within a plane (called the X and the Y motion). The other degrees of freedom must be kept within very tight tolerance bands, typically in the order of tens of nanometers. The guidance of the wafer-stage may not show any wear for this would degrade the accuracy of the system and worn off particles will contaminate the wafer. Recent developments have shown that a good alternative for air-bearing guides is needed in modern wafer steppers [37]. Magnetic bearings may just be that alternative.

Another field of research where nanometer accuracy manipulations along a long stroke (up to millimeters) is desired is the biomedical research. New projects on molecular manipulation of DNA cells ask for a very high accuracy, combined with a good isolation of vibrations of the environment and good controllable actuator characteristics.

Positioning along a long range with high accuracy is becoming increasingly important in the areas of:

- scanning microscopy,
- photo etching,
- micro technology, and
- photo plotting.

When, for example, the positioning accuracy of the linear slide of Figure 1.1 is analyzed, six possible errors, related to the five degrees of freedom in the bearing direction and one degree of freedom in the motion direction, can be distinguished. Each error corresponds to one of the three perpendicular directions and their rotations. These errors all contribute to the inaccuracy of the position of the slide.

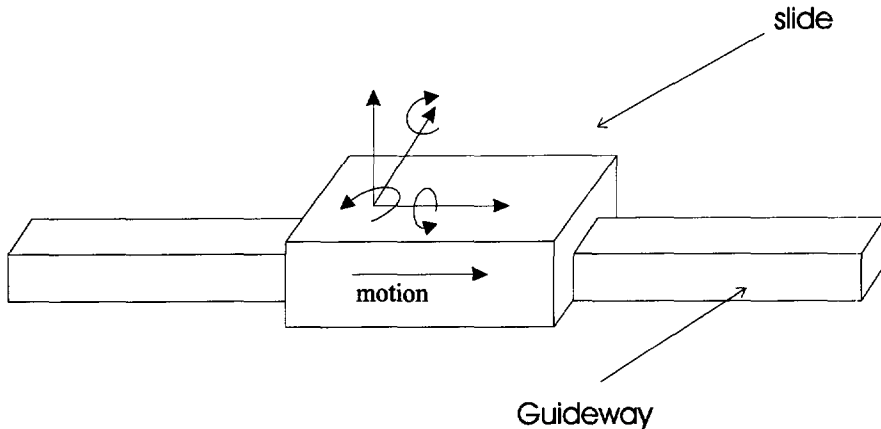


Fig. 1.1 Schematic view of a linear slide. Five possible bearing errors can be distinguished: one for each fixed degree of freedom of the slide and one error in motion direction. Bearing elements, that allow the slide to move along the guideway, are placed between the slide and the guideway and must minimize the bearing errors.

The position errors of the slide can be divided into two types: Static errors and dynamic errors. Each type will be discussed below.

1.1.1 Static errors

Static errors are errors caused by error sources that are stationary. This means that these errors do not change in time, or do change very slowly. Static errors can be divided into:

- errors in the bearing direction, caused by manufacturing errors in the guideway and wear of the bearings, and
- errors in the propulsion direction, caused by stick-slip.

The errors in the bearing direction are most often caused by the limited fabrication accuracy of the guideway or by bad performance of the bearing elements. The bearing elements are situated between the slide and the guideway. These bearing elements can either be passive bearings, or active bearings (bearings with an automatic error-detection and correction mechanism).

Passive bearings

Most bearings in use in positioning devices are passive bearings. The conventional bearings, such as roller bearings and sliding bearings, but also the more complex aerostatic and hydrostatic bearings, are all examples of passive bearings. A lot of effort has been put into passive bearings, in order to get them to function as accurately as possible.

Research performed by Sebestyen [54] indicates that there exists a limit in the achievable positioning accuracy when passive bearings are used. The positioning accuracy depends on the quality of the bearings and the quality of the guidance. Therefore, the manufacturing accuracy of all the bearing parts and the guideway should be high, in order to get high accuracy.

Conventionally machined parts allow for a minimum bearing inaccuracy of a few μm . If special attention is paid to the manufacturing process, this inaccuracy decreases to 1 μm , or better, depending on the effort taken. The parts become very expensive, and special care should be taken in order to preserve the quality of these parts. Extremely accurate manufacturing processes can lead to nanometer inaccuracy of the bearing combined with a short stroke in propulsion direction, as can be concluded from Monteiro [47].

Generally, the bearing accuracy of a passive bearing can not be better than the accuracy of the components of which it is built up. Air bearings are an exception: air bearings average out small irregularities in the guideway.

Active bearings

Modern research in precision engineering has indicated that the problems related to the accuracy of positioning in passive bearings can be overcome by active bearings. Active bearings measure the actual position of the bearing element and relate it to a reference frame. This reference can be fixed to the guideway or to any other arbitrary body. The position errors measured will result in an action of an actuator, thus correcting the position.

Active bearings are expensive for they need a sensor, a controller and most of the time a power amplifier. The complexity of active bearings results in virtually no off the shelf designs and the need of better understanding of the mechanics and dynamics at the user end. Research has shown that the accuracy of active bearings can be orders of magnitude better than the accuracy of the machined parts it is made of [63]. The inaccuracy of the guideways can be measured and is compensated for. Good designs show no dependency on the quality of the guideway, but only on the accuracy of the sensors used.

Sebestyen [54] has shown that active bearings for linear motion become competitive with passive bearings if accuracies better than 1 μm are to be achieved. Investing in passive bearings with accuracies below 1 μm is not useful, according to Sebestyen.

The positioning accuracy of the slide in propulsion direction depends on:

- the accuracy of the propulsion system, and
- the amount of stick-slip present in the bearings.

The fact that the positioning accuracy in the propulsion direction depends on the accuracy of the propulsion system (including the sensor) is no great surprise. A lot of designs have been made of propulsion systems that show good accuracy. Important is to note (de Lange [38]) that linear propulsion systems with long stroke and high accuracy are always designed as a servo system. There exist some open-loop linear motors (piezo stacks and magnetostrictive drives), but they have a very limited stroke. Open-loop systems with long stroke also exist (i.e. the stepper motor), but they have low positioning accuracy.

Stick slip in the bearing elements also influences the positioning accuracy in the propulsion direction. The lack of a good model of stick slip, and the unpredictable behavior of friction hinders high accuracy positioning. Evidence of this can be found in the fact that most high accuracy positioning systems use air bearings (no stick slip and very low friction) or magnetic bearings (no contact, so

no friction or stick slip). Eisenhaure [22] shows that positioning with atomic accuracy in the propulsion direction can be achieved with magnetically suspended devices. Therefore, although magnetic bearings are a very complex type of bearing, their applications gain rapidly in the specific field of high accuracy positioning. Evidence of this trend can be found in [57] and in [44].

1.1.2 Dynamic errors

Beside the static error sources mentioned above, dynamic error sources can be identified. Dynamic errors are caused by vibrations originating from two sources:

- external vibration sources, and
- internal vibration sources.

External vibrations, i.e. vibrations of the building or the workplace on which the magnetic bearing is located, can be divided in different classes. Each class corresponds to a specific environment, where vibrations of a certain level are allowed. These classes are shown in Figure 1.2.

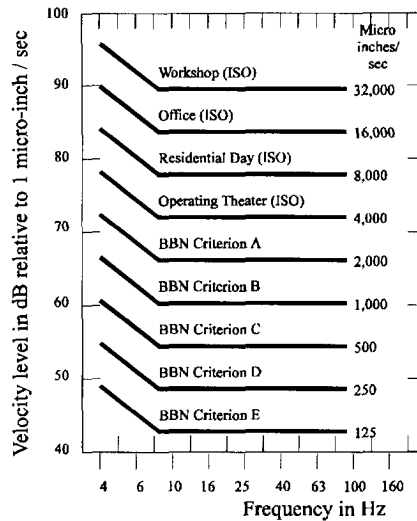


Fig. 1.2 Classes of vibrations. The vibrations are measured in RMS level of the vibration speed, usually measured in μips ($1 \mu\text{ips} = 1 \text{ micro inch per second}$). Taken from [2].

Figure 1.2 shows a classification of vibrations measured on a scale of the velocity level of the environment. The harmonic motion with a frequency ω can be described by:

$$\begin{aligned} y &= A \cdot \sin(\omega \cdot t) \\ \dot{y} &= A\omega \cdot \cos(\omega \cdot t) \\ \ddot{y} &= A\omega^2 \cdot \sin(\omega \cdot t) \end{aligned} \quad (1.1)$$

where

- y = the position of the environment,
- \dot{y} = the velocity of the environment,
- \ddot{y} = the acceleration of the environment,
- A = the amplitude of the movement,
- ω = the frequency of movement, and
- t = time.

A representation of a mass-spring-damper system can be presented in Figure 1.3. All the degrees of freedom of the slide shown in Figure 1.1 can be represented mathematically by such a mass-spring-damper system. The two error-sources are shown in Figure 1.3 as a moving floor, y , (external vibration) and as a force, F , (internal vibration), working on the slide.

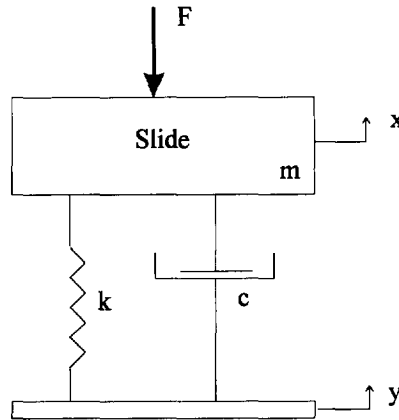


Fig. 1.3 Mass-spring-damper system representation of one degree of freedom of the linear slide. The external vibration is caused by the moving floor, y , and the internal error source is represented by the force F .

The influence of the external vibrations of the floor, y , on the position of the slide, x , can be calculated with:

$$\frac{x}{y} = \sqrt{\frac{1 + \left(2 \cdot \beta \cdot \frac{\omega}{\omega_0}\right)^2}{\left(1 - \frac{\omega^2}{\omega_0^2}\right)^2 + \left(2 \cdot \beta \cdot \frac{\omega}{\omega_0}\right)^2}} \quad (1.2)$$

$$\text{where } \omega_0 = \sqrt{\frac{k}{m}} \text{ and } \beta = \frac{c}{2 \cdot m \cdot \omega_0}.$$

The position error, ε , is defined as the difference between the motion of the reference frame, i.e. the ground, and the slide:

$$\varepsilon = x - y \quad (1.3)$$

which leads to

$$\frac{\varepsilon}{y} = \sqrt{\frac{1 + \left(2 \cdot \beta \cdot \frac{\omega}{\omega_0}\right)^2}{\left(1 - \frac{\omega^2}{\omega_0^2}\right)^2 + \left(2 \cdot \beta \cdot \frac{\omega}{\omega_0}\right)^2}} - 1 \quad (1.4)$$

Together with a constant vibration-speed level of a typical environment of \dot{y}_{typical} , the following calculation can be made:

$$\dot{y} = \dot{y}_{\text{typical}} \cdot \cos(\omega \cdot t) \quad (1.5)$$

combined with equation (1.1) and (1.4), leads to:

$$\varepsilon = \frac{\dot{y}_{\text{typical}}}{\omega} \cdot \left\{ \sqrt{\frac{1 + \left(2 \cdot \beta \cdot \frac{\omega}{\omega_0}\right)^2}{\left(1 - \frac{\omega^2}{\omega_0^2}\right)^2 + \left(2 \cdot \beta \cdot \frac{\omega}{\omega_0}\right)^2}} - 1 \right\} \quad (1.6)$$

Equation (1.6) is shown in Figure 1.4, with a \dot{y}_{typical} level corresponding to 32,000 micro inches per second ($= 8.125 \cdot 10^{-4}$ m/s). Figure 1.4 clearly shows that a bandwidth (or eigenfrequency) of approximately 100 Hz is necessary to achieve sub-micrometer accuracy.

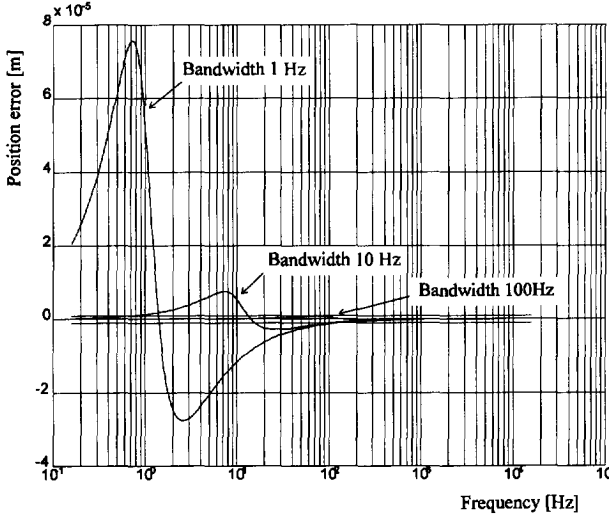


Fig. 1.4 Three calculations of the position error as a function of the frequency of the environmental vibration of 32,000 micro inches per second and the eigenfrequency ω_0 (1 Hz, 10 Hz and 100 Hz, respectively) of the mass-spring-damper system. A damping coefficient β of 0.7 has been assumed.

Internal forces that are generated by the payload placed on the slide will also result in a position inaccuracy. The influence is given by:

$$\frac{x}{F} = \frac{I}{\sqrt{\left(1 - \frac{\omega^2}{\omega_0^2}\right)^2 + \left(2 \cdot \beta \cdot \frac{\omega}{\omega_0}\right)^2}} \quad (1.7)$$

A static load for example, caused by an uncertainty or measurement error in the payload, can amount to say 1 N. Substituting this in Equation (1.7), together with $\omega = 0$ (static force) and a maximum displacement of 1 μm , results in a required minimum stiffness of 10^6 N/m .

1.2 Goal of this research

The general goal of this research was established in close co-operation with Philips Centre for manuFacturing Technology (CFT), of the Nederlandse Philips

Bedrijven B.V. The aim is to design a function element applicable in high accuracy positioning devices. The function element must be capable of performing two specific tasks or functions. These functions are:

- contact free suspension or bearing of a mass in 1 degree of freedom, without any constraints on the other degrees of freedom, and
- contact free propulsion of that mass in 1 degree of freedom, perpendicular to the suspended degree of freedom.

The two degrees of freedom must allow for micrometer accuracy performance in both directions.

The characteristics of the function element must include a static stiffness of 10^6 N/m and a bandwidth of 100 Hz in all degrees of freedom. With these specifications the influence of external vibrations will be kept within the required 1 μ m accuracy limit.

The function element, that has to satisfy the requirements mentioned is called the Suspension and Propulsion Unit (short: SPU), and must be an autonomous element. This means that more than one SPU can be applied in a combination into, for example, a linear slide, or an XY Φ positioning table.

In the beginning of this research the following choice was made: The working principle of the SPU will be based on the working principle of magnetic levitation. Other approaches can be based on conventional bearing methods, but these are not researched here. Research done at the three major research centers for magnetic bearings (ETH Zurich, Schweitzer *et al*, the University of Virginia, Allaire *et al*, and the Tokyo University of Technology, Higuchi *et al*) on rotating magnetic bearings gave confidence in the achievability of the goal of this research.

The goal set by Philips CFT and the Laboratory for Micro Engineering results in an active magnetic bearing design integrated with a linear motor. Both the bearing direction, as well as the propulsion direction, are designed as closed loop servo systems, with a magnetic circuit, sensors, power amplifiers and a controller.

The aim of this work is to introduce active magnetic bearings with linear propulsion into the precision engineering environment. This introduction can best be done by building a high accuracy XY Φ stage with magnetic bearings and linear propulsion. Together with this aim, a design strategy must be presented, both for the design of the SPU and for the design of the controller. A link between the required specifications of a particular design and the design itself

will facilitate future integration of magnetic bearings in the precision engineering environment.

1.3 Layout of this thesis

Chapter 1 describes the goal of this research and defines the specifications of high accuracy positioning systems.

Chapter 2 will give a classification of magnetic forces suitable for suspension and propulsion together with an overview of the history and the state of the art of magnetic bearings and linear motors. A description of the various types of forces and a motivation of the choice made for this research will be given.

Chapter 3 discusses the design of the magnetic bearing. The magnetic actuator that forms the heart of the system will be thoroughly analyzed. Attention is paid to the design of a classical PID controller for the bearing. This Chapter also gives practical information about the magnetic circuit, the magnetic materials and the limitations on the achievable performance of magnetic bearings.

Chapter 4 elaborates on the propulsion aspects of the function element and shows how linear propulsion is added to a magnetic bearing in a unique way. The uniqueness results from the use of one magnetic field both for the suspension and for the propulsion. This way the Suspension and Propulsion Unit or SPU is completed.

The three additional components of the Suspension and Propulsion Unit will be discussed in Chapter 5. These elements are the sensors, the amplifiers and the digital controller hardware and software. An overview is given of all sensor-types that perform a contact free position measurement and are suitable for the magnetic suspension or propulsion.

Chapter 6 discusses the experimental setup of one SPU, while Chapter 7 shows how three SPU's can be combined into an $XY\Phi$ positioning system with micrometer accuracy. Measurements on these experimental set-ups show good resemblance with respect to the simulated performance.

Chapter 8 gives a set of design rules that can be used to design and build SPU's of various sizes. The rules will result in a stable system that can be used as a starting point for the development of contact free positioning systems. More insight on the applicability of SPU's is gained when scaling factors are analyzed. This is also part of this Chapter.

The last Chapter will discuss conclusions and will give some recommendations for further development of the SPU.

2 Magnetic suspension and propulsion

2.1 Introduction

The Laboratory for Micro Engineering at the Delft University of Technology has started research in magnetic bearing and magnetic propulsion for linear movement in 1991. The research has lead to the development of a unique element for combined suspension and propulsion. This thesis describes the working principle, the first experiments and the first results of this element. The Suspension and Propulsion Unit (short: SPU) was presented at three major conferences on magnetic bearings (MAG'93 [3], MAG'94 [4] and MAG'95 [6], [7]) and at a conference on new actuators (ACTUATOR'94 [5]).

This chapter starts with two historical overviews: an overview of magnetic bearings and an overview of linear motors. Following the two historical overviews, a classification will be made of electromagnetic force types, and their implementation in the SPU.

2.2 History of and trends in magnetic bearings

The idea of completely contact-free support of a ferromagnetic body by means of magnetic forces is very old. The first patent on magnetic bearings was granted in 1830. A first technical design concept featuring a mechanical control was patented in 1912. Several other approaches turned out to be unfeasible due to lacking technological support, like fast control and power electronics.

The realization of a first active magnetic bearing goes back more than 50 years to 1938 when an electro-magnetic suspension was built by Kemper. His goal was proving that magnetically levitated vehicles are feasible as a new means of transportation. This bearing was designed for linear movement or translations.

In 1946 several experiments were carried out by Beams at the University of Virginia, Charlottesville USA. Beams employed magnetic suspension as a means to carry out extensive experiments on physical properties in areas of isotope separation, biophysics, materials science and gravitational physics. His magnetic bearing was designed to support a rotating mass.

Beams set the current world record for high speed rotation at four million revolutions per second. These speeds were necessary to investigate the behavior of superficial layers on very small balls.

The research of Beams was continued by Gilpin at the University of Virginia, who extended the experiments of Beams. Gilpin built his first rotating machinery with magnetic bearings in 1958.

Space research brought considerable progress in magnetic bearing technology in the late sixties and seventies. Fields of application were mainly momentum flywheels for satellite stabilization. Typical advantages of magnetic bearings for momentum flywheel applications is the low drag torque and the unproblematic use under vacuum conditions. Many companies and universities started with this new technology in this era:

- Tokyo institute of Technology (Japan)
- National Aerospace Laboratory (Japan)
- Hitachi, Toshiba (Japan)
- NASA (USA)
- Sperry (USA)
- MIT (USA)
- MT (USA)
- Draper Lab. (USA)
- LRBA-CNES-SEP (France)
- S2M (France)
- Aerospatiale (France)
- Royal aircraft establishment (England)

In the early eighties Russia also started with research on magnetic bearings, typically for satellite flywheel stabilization and energy storage systems.

The experience gained with magnetic bearings in space technology and the rapid progress in electronics in the seventies (integrated circuits, power electronics) rendered magnetic bearings ready for industrial use. First applications were carried out mainly by the French company Société de Mécanique Magnétique (S2M) in the field of turbo machinery and high speed machining. Now S2M is the world leader on magnetic bearings for industry. Due to their

unique properties, magnetic bearings proved to be exceedingly interesting for application in high-speed rotating machinery.

In 1980, theoretical interest in the fundamentals of magnetic bearing technology grew rapidly. Concentrating on rotating machinery, important research work was done in Munich, Duisburg, Darmstadt, Zurich, Univ. of Maryland, Univ. of Bath, Univ. of Virginia, MIT and the University of Tokyo.

Recently, three trends in active magnetic bearings can be noticed:

- Analog control is abandoned in favor of digital control. The more complex control strategies necessary for the better control of magnetic bearings is now possible thanks to the rapid growth in Digital Signal Processing.
- High rotor speeds are becoming more and more important in rotating magnetic bearing technology. Thanks to the special qualities of magnetic bearings, related to their contact free operation and mechatronic design approach, very high rotor speeds ($>50,000$ rpm) are now feasible.
- High accuracy positioning is achieved using magnetic bearings for linear suspension. This trend is caused by the ever increasing requirements on accuracy in IC fabrication technologies and, in general, by all precision engineering problems. A long stroke combined with a high accuracy becomes more and more important.

The trend toward high accuracy positioning with magnetic bearings for suspension, but also with magnetic bearings as an actuator for positioning, has recently been confirmed by the companies manufacturing IC-lithography steppers. These companies claim that the future of wafer steppers is toward magnetically suspended and magnetically propelled systems showing sub-micrometer accuracy in all degrees of freedom.

2.3 History and state of the art of linear electro-motors

Man has been fascinated by electricity ever since he first discovered it. This fascination may even go back to the very beginning, when man was first confronted with lightning. The same fascination played an important role in the life of Michael Faraday. Faraday discovered the principle of electromagnetic induction in 1831.

In 1832, Faraday demonstrated the first homo-polar electromagnetic generator. This generator demonstrated the principle of electromagnetic induction: A copper disk rotating in a constant magnetic field produces an electrical current.

In 1841, Wheatstone built the first linear induction motor. But the focus of the industry in that era was toward steam and steam engines, not electricity, so his invention soon disappeared into a museum.

In 1888, Tesla introduced a 3-phase induction machine. He probably could not have imagined, that this type of motor (rotary and linear) would be the most commonly used electromotor this decade.

Linear electromotors were invented a long time ago. Nevertheless, they did not appear in industry until 1946, when a lot of effort was spent on the Elektropult. The Elektropult is a linear induction motor capable of accelerating an aeroplane off a war-ship.

The interest in linear electromotors can be shown in a graph. Figure 2.1 shows this graph with the investment in linear motors plotted against time. The peak just after the second world war is evident. The rise in investment in the seventies is mainly caused by the research and experiments done in magnetically levitated transportation. Especially the research done by Laithwaite [37] has contributed to the development of linear motors.

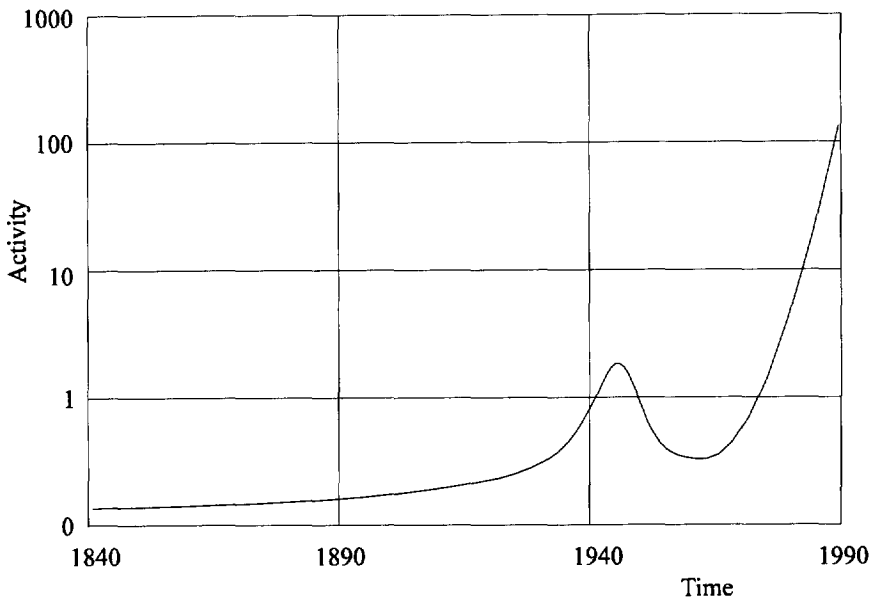


Fig. 2.1 Investment (relative value) against time in linear motors. Notice the investments just after the second world war, when the Elektropult was built. Taken from [34].

Research efforts made after the seventies, inspired by the inventions of Laithwaite, has motivated many researchers to look into linear motors. Evidence of the vast growth in linear motor developments can be found in [1] and [34].

It is permitted to state that every thinkable magnetic effect has been exploited by now to build a linear motor. Every type of magnetic force has led to some type of linear motor, as will be discussed in Section 2.4.

2.4 Classification of magnetic forces

Magnetic forces are forces exerted on a body by means of a stationary or alternating magnetic field. The physical cause of magnetic forces can be traced back to the moving of electric charge. Books on magnetic fields and forces are: [19], [41] and [48].

Magnetic forces can be divided into two classes: Forces derived from the energy stored in the magnetic field (reluctance force) and forces exerted on a moving charge in a stationary magnetic field (Lorentz force).

The reluctance force is derived from the energy stored in the magnetic field which can be converted to mechanical energy. The reluctance force F_R is obtained from the principle of virtual work:

$$F_R = \frac{\partial W}{\partial s} \quad (2.1)$$

with the field energy w and the virtual displacement ∂s . A magnetic force of this type always arises perpendicular to the surface of media of different relative permeability μ_r . For ferromagnetic materials with $\mu_r \gg 1$ the forces can become very large, thus fulfilling an essential prerequisite for technical use.

The Lorentz force F_L , acting on an electric charge Q , results according to the basic law:

$$F_L = Q(E + v \times B) \quad (2.2)$$

with the electric field, E , and the charge, Q , moving at the velocity v in a magnetic field with flux density B . All quantities are represented as vectors or vector fields. The effect of the energy density of E can be neglected in macroscopic arrangements, compared to the effect of the magnetic field B . In Equation (2.2) the product of charge and velocity is replaced by the current I , leading to

$$F_L = I \times B \quad (2.3)$$

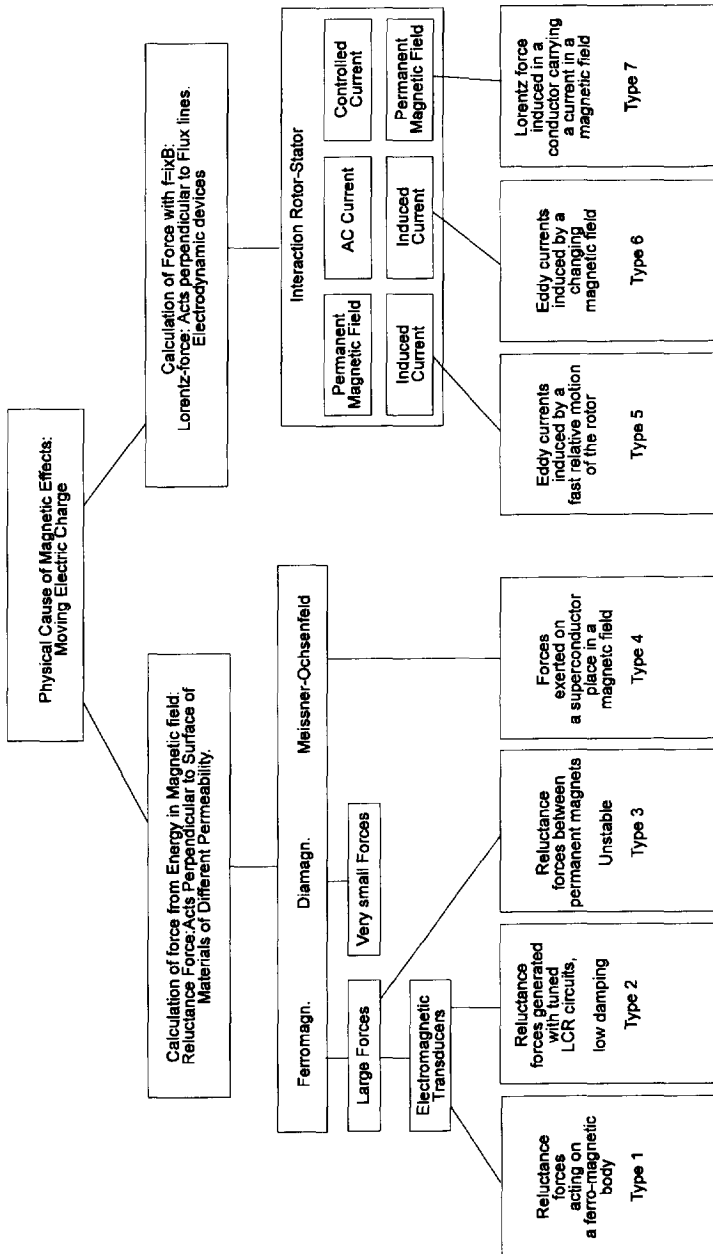


Fig. 2.2 Classification of magnetic forces for suspension.

This force always arises orthogonal to the flux lines, and is therefore parallel to the surface emitting the magnetic field B .

A survey of magnetic forces was made and a classification is shown in Figure 2.2. The classification shows seven methods of implementation of the two basic magnetic force types.

This Section will discuss the seven methods of implementation shown in Figure 2.2, and their application in suspension and propulsion systems.

Type 1: Reluctance forces acting on a ferromagnetic body

The implementation of reluctance forces acting on a ferromagnetic body can be controlled very well. The forces can be very large, depending only on the energy put into the system. The implementation is frequently used to build active magnetic bearings. The fact that the force acts along a small air-gap and perpendicular to the surface of the medium containing the flux, makes it highly suitable for magnetic bearings. Examples of these classical magnetic bearings can be found in magnetic suspension of multi-ton trains [36] as well as in suspension of a rotor with a mass of a few gram [11]. Work on magnetic bearings with type 1 forces is found in [53], [59] and [28]. Evidence of high accuracy precision bearings is found in [64], [65] and [35]. Implementation of reluctance forces in linear motors can be found in [34]: a linear stepper motor and a linear reluctance motor. Both linear motors show a force parallel to the surface of the motor, caused by a toothed structure of the stationary and the moving part and by the fact that the reluctance force wants to align the teeth. A very strong normal force is the inevitable side effect.

Type 2: A tuned LCR circuit

A tuned LCR circuit consists of a coil with self inductance L , a resistor R and a capacitor C . An LCR circuit can be tuned at a certain resonance frequency. The influence of the size of the air-gap on the self-inductance L , causes the resonance frequency to change. A reluctance to change the eigenfrequency results in a stabilization of the force on the rotor and therefore a stabilization of the air-gap. Building a bearing based on this principle can be done. Forces are high, but the damping and the stiffness are very poor. Additional information can be found in [30], [29] and [31]. No linear motors are found operating on the basis of this principle.

Type 3: Forces exerted by permanent magnets

Permanent magnets exert forces upon ferromagnetic materials and upon other permanent magnets. Forces between permanent magnets only can be attractive or repulsive. Earnshaw [21] and Braunbeck [17] showed that a stable suspension with just permanent magnets can not be built. However, a configuration can be thought of where permanent magnets are used to support a few degrees of freedom, while the other degrees of freedom are controlled in another way. Such systems are called hybrid systems, and can be found in [49], [45] and [58]. A mechanical control of permanent magnet position can also lead to a stable suspension. This is shown in [52].

Type 4: The Meissner-Ochsenfeld effect

Superconducting materials show some very remarkable effects in combination with magnetic fields. A well known example is the Meissner-Ochsenfeld effect: A piece of superconducting material will float above a permanent magnet. An example of a magnetically supported train using superconductors is described in [51]. Linear motors using superconductors are reported in [34]. Application of superconductors in small-scale projects has not been found.

Type 5: Eddy currents in combination with a stationary magnetic field

Electrodynamic levitation occurs when eddy currents are induced through a fast relative motion between stator and rotor. Repulsive forces can be high, but very high flux densities are needed. Application of this effect is found in magnetically levitated trains, in combination with superconducting materials [50]. Application of this type in small-scale projects has not been found.

Type 6: Eddy currents induced with alternating magnetic fields

By alternating a magnetic field, eddy currents will be induced in a conducting object inside the magnetic field. The eddy currents interact with the magnetic field, thus creating a force. The direction of the force is such that it can be used to suspend or to propel. Magnetic eddy current bearings have been researched, [55] and [12], but have proven to have a major set-back: the suspended object becomes very hot. Linear motors using eddy currents are very common. The linear induction motor has been realized in many designs. [24], [42] and [60] report extensively about them.

Type 7: Current carrying conductor in a stationary magnetic field

This is a very straightforward implementation of a Lorentz force. A conductor carrying a current within a stationary magnetic field, is the last type of magnetic force generation discussed here. The force can be used for bearing of a rotating system, as well as for generating a propulsion force. A linear motor conceived with this type of force is called a linear DC motor. The stationary magnetic field is usually provided by a permanent magnet. De Lange [38] reports on the aspects of linear DC motors. Precise positioning with sub-micrometer accuracy is described in [61] and [37].

2.5 Selection of the forces and their implementation in the SPU

It is clear that the research described in this thesis focuses on accuracy of suspension and propulsion. The manner in which magnetic suspension and propulsion have to be achieved can be chosen freely. It is obvious that a close examination of the seven methods of implementation is needed.

Type 1: Reluctance forces acting on a ferromagnetic body are very well suited for magnetic suspension. This was proven by the three major research centers for active magnetic bearings in the world at this moment. I.e.:

- Tokyo University of Technology (professor Higuchi),
- University of Virginia (professor Allaire), and
- ETH Zurich (professor Schweitzer).

The suspension function of the SPU in this research is based on the Type 1 implementation of the reluctance force.

The use of reluctance forces for propulsion is also possible. The linear stepper motor and the linear reluctance motor are good examples of this. If, however, the working principle of the stepper motor is analyzed one disturbing feature comes into the picture. The accuracy of the toothed slot pattern on the stepper motor (and in the reluctance motor) is directly related to the accuracy of the positioning. Together with the fact that a force perpendicular to the propulsion direction of the motor is generated that varies along its stroke, makes this type of motors less suitable for high accuracy positioning.

Type 2: A tuned LCR circuit is not very well suited for magnetic suspension. The following disadvantages cling to the working principle:

- Bad controllability of the damping, and
- low stiffness of the bearing.

The use of a tuned LCR circuit for linear positioning has not been reported. The whole concept seems inappropriate for use in the SPU.

Type 3: Forces exerted by permanent magnets can not lead to a stable magnetic suspension. This can be proven with a mathematical derivation. Earnshaw [21] showed that the use of just permanent magnets can not lead to a stable suspension in combination with materials with $\mu_r > 1$. Materials with diamagnetic properties ($0 < \mu_r < 1$) or superconducting materials ($\mu_r = 0$) can be used in combination with permanent magnets. They can form a stable suspension, as was shown mathematically by Braunbeck [17].

Permanent magnets in combination with electromagnets can be used to form so called hybrid magnetic bearings. This research has not used hybrid magnetic bearings, although it is recognized that they form a good alternative for the magnetic bearing configuration that has been designed.

Type 3 implementation of reluctance forces used for propulsion is conceivable, but a toothed pattern is needed, like the reluctance motor. Therefore, type 3 implementation of reluctance forces is not useful for high accuracy positioning.

Type 4: The use of superconducting materials look very promising both for suspension and propulsion. The materials developed for superconduction show a steady increase in critical temperature. The critical temperature is the temperature at which the material becomes superconducting, and the electrical resistance drops to zero. The current state of the art indicates that materials with a critical temperature of 70 K exist nowadays.

Although this development looks very interesting, research at the Laboratory for Micro Engineering does not include superconduction. Therefore, no research was done in this field, and this type of force will not be used here.

The low critical temperature also hinders the use of superconducting materials in consumer products where magnetic bearings might be used in the future. Industrial applications of superconducting materials can be found, but not yet in great quantities.

Type 5 and Type 6 implementation of Lorentz forces both use eddy currents induced in the supported mass. The required accuracies for both suspension and propulsion seem to be achievable here. However, another problem arises. Eddy currents introduce heat. Since the supported mass is suspended contact free, the dissipation of heat generated in the supported mass will be very difficult. When positioning with high accuracy is considered, temperature changes will have to be kept to a minimum. The thermal gradients, in combination with different

coefficients of expansion will result in inaccurate positioning. Type 5 and type 6 implementations were not further researched for this reason.

Type 7: Lorentz forces generated by a conductor carrying a current within a stationary magnetic field can be used for both suspension and propulsion. The stationary magnetic field can be supplied by a permanent magnet or by means of an electromagnet.

Suspension by means of Lorentz forces is not common. This force type is most commonly used for propulsion in linear DC motors, rather than as a means of providing suspension.

Linear DC motors use the stationary magnetic field of a permanent magnet. These permanent magnets are usually located on the stationary part of the motor. The current carrying conductor is located on the moving part. The other way around (stationary coils and moving magnets) is also possible.

Linear DC motors are always implemented as a servo controlled motor. The position is measured, and a feedback loop is used in combination with a controller (usually PID) to give the motor the characteristics required. One of the remarkable features of linear DC motors is that the positioning accuracy can be as good as the accuracy of the position measurement performed by the sensor of the servo system.

Summary

This Section has shown that the Suspension and Propulsion Unit can best use:

- electromagnetic reluctance forces for suspension, and
- Lorentz forces for propulsion.

The design of the SPU is based upon a conventional active magnetic bearing unit (which will be discussed in Chapter 3) with a Lorentz force linear DC motor incorporated into it (which will be discussed in Chapter 4).

3 Magnetic Suspension

3.1 Introduction

In this Chapter the theoretical model of a magnetic bearing for linear suspension, using electromagnetic reluctance forces (implementation Type 1, Chapter 2) is analyzed. The analysis of the force is the most important part of the theoretical model. The analysis is given for a one degree of freedom system only.

Another important part of this Chapter describes a set of steps for designing the controller needed for the stabilization of the magnetic suspension. A close look at physical limitations is taken in order to properly understand the real-world problems in relation with the simplified model.

Throughout this Chapter, the stationary part of the magnetic bearing, connected to the real world, will be called stator. The suspended part will be called rotor. It is recognized that the rotor does not actually rotate in a linear motion, but the name is chosen for its compatibility to other work on magnetic bearings, for instance at the ETH Zurich, see [62], [27], [10], [56] and [39]. Other authors have suggested names like Flotor or Translator, but these names do not seem to persist.

3.2 Theoretical model of the reluctance force

A possible electromagnetic circuit for generating a reluctance force is shown in Figure 3.1. The E-shaped core contains a coil wound around the central magnetic pole. The I-shaped core is attracted by the E-core by means of the reluctance force F_R .

The calculation of the magnetic reluctance force generated by an electromagnetic E-I core combination (Figure 3.1) is given with the following assumptions:

- The magnetic field exhibits no stray flux so it is confined within the air-gap of the electromagnetic circuit. This assumption is true for small air-gaps.
- The magnetic field is distributed homogeneously in the air-gap. This is a reasonable assumption for homogenous materials.
- No eddy-currents occur, caused by changing magnetic fields, in any part of the magnetic circuit. When a lamelated material is used for the magnetic circuit this assumption is reasonably true.

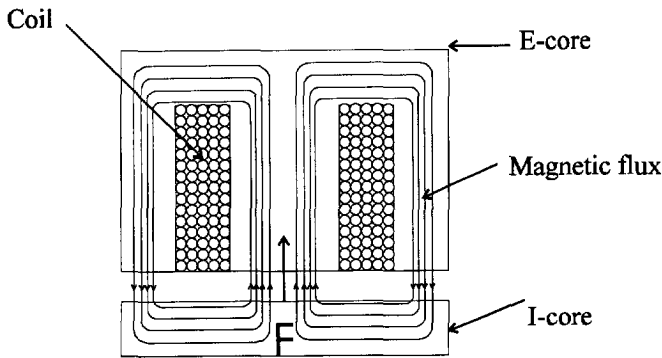


Fig. 3.1 Basic electromagnetic circuit showing the coil that generates the flux, the electromagnetic circuit (E-core and I-core) and the flux lines. The energy stored in the air-gap results in a reluctance force F .

Given these restrictions, the electromagnetic reluctance force is calculated as follows:

The energy in the air-gap equals:

$$W = B_{air} \cdot H_{air} \cdot A \cdot x \quad (3.1)$$

where

- W = the magnetic energy,
- B_{air} = the magnetic field density in the air-gap,
- H_{air} = the magnetic field strength in the air-gap,
- A = the cross-sectional area of central magnetic pole, and
- x = the air-gap.

With

$$B_{air} = \mu_0 \cdot \mu_{r,air} \cdot H_{air} \quad (3.2)$$

Equation (3.1) is changed into:

$$W = \frac{B_{air}^2 \cdot A}{\mu_0 \cdot \mu_{r,air}} \cdot x \quad (3.3)$$

The force generated with a magnetic circuit can be found as:

$$F_R = \frac{\partial W}{\partial x} = \frac{B_{air}^2 \cdot A}{\mu_0 \cdot \mu_{r,air}} \quad (3.4)$$

By substituting

$$B_{air} = \frac{\Phi}{A} \quad (3.5)$$

where

Φ = the magnetic flux,

in Equation (3.4), results in a reluctance force described by:

$$F_R = \frac{\Phi^2}{\mu_0 \cdot \mu_{r,air} \cdot A} \quad (3.6)$$

The magnetic flux Φ equals the amount of flux in the iron parts, so:

$$\Phi = B_{iron} \cdot A = B_{air} \cdot A \quad (3.7)$$

and using

$$B_{iron} = \mu_0 \cdot \mu_{r,iron} \cdot H_{iron} \quad (3.8)$$

the magnetic field strength can be calculated:

$$H_{iron} = \frac{\Phi}{A \cdot \mu_0 \cdot \mu_{r,iron}} \quad (3.9a)$$

and

$$H_{air} = \frac{\Phi}{A \cdot \mu_0 \cdot \mu_{r,air}} \quad (3.9b)$$

Calculating the line-integral along the magnetic circuit:

$$N \cdot I = \oint_c \mathbf{H} \cdot d\mathbf{l} \quad (3.10)$$

where

N = the number of windings of the coil, and

I = the current through the coil,

results in:

$$N \cdot I = H_{air} \cdot 2 \cdot x + H_{iron} \cdot l_{iron} \quad (3.11)$$

with

l_{iron} = the mean length of the flux path in the iron part.

Substituting Equation (3.9a) and Equation (3.9b) in Equation (3.11) yields:

$$N \cdot I = \frac{\Phi \cdot l_{iron}}{A \cdot \mu_0 \cdot \mu_{r,iron}} + \frac{\Phi \cdot 2 \cdot x}{A \cdot \mu_0 \cdot \mu_{r,air}} \quad (3.12)$$

Solving for Φ in (3.12) and substituting Φ in Equation (3.6) yields:

$$F_R = \frac{\mu_0 \cdot N^2 \cdot A \cdot I^2}{\mu_{r,air} \left(\frac{2x}{\mu_{r,air}} + \frac{l_{iron}}{\mu_{r,iron}} \right)^2} \quad (3.13)$$

Equation (3.13) defines the magnetic reluctance force for the circuit drawn in Figure 3.1, under the restrictions mentioned in the beginning of this Section. The electromagnetic reluctance force forms the center of the magnetic bearing working principle and should therefore be controlled very accurately. An accuracy analysis of the magnetic reluctance force is given in Section 3.5. A detailed derivation of the magnetic reluctance force can be found in [8].

3.3 Theoretical background of the magnetic bearing actuator

The combination of two electromagnetic E-I cores placed opposite to each other will result in the magnetic actuator shown in Figure 3.2. This actuator forms the heart of a magnetic bearing.

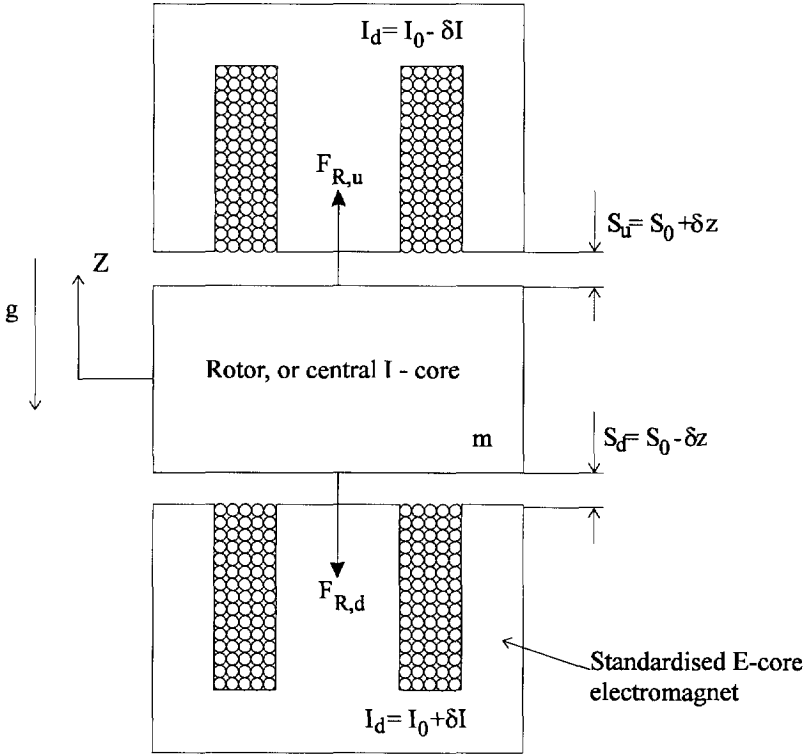


Fig. 3.2 Basic layout of a magnetic bearing for linear suspension. Two E-core electromagnets exert forces upon a central I-core. The Figure shows the air-gaps, $S_u = S_0 + \delta z$ and $S_d = S_0 - \delta z$, the coils with currents $I_u = I_0 - \delta I$ and $I_d = I_0 + \delta I$, and the I-core with mass m .

As was shown in Section 3.2, the force F_R on the ferromagnetic body can be calculated with (3.13). If a simplification is used, that is $\mu_{r,iron} \gg \mu_{r,air}$, then Equation (3.13) can be simplified to:

$$F_R = \frac{1}{4} \mu_0 \mu_{r,air} N^2 A \cdot \frac{I^2}{S^2} = K_M \cdot \frac{I^2}{S^2} \quad (3.14)$$

where

K_M = the magnetic circuit constant.

Figure 3.2 shows that two forces are exerted upon the rotor by the two E-core electromagnets. These forces are called $F_{R,u}$ and $F_{R,d}$. Both forces can be

calculated with Equation (3.14). The corresponding air-gaps are S_u and S_d , while the corresponding currents are I_u and I_d . Using Newton's first law of mechanics, the following equation of motion can be found for the mass m :

$$\begin{aligned} m \cdot \ddot{z} &= m \cdot g - F_u + F_d \\ &= m \cdot g - K_M \cdot \frac{I_u^2}{S_u^2} + K_M \cdot \frac{I_d^2}{S_d^2} \end{aligned} \quad (3.15)$$

The remaining five degrees of freedom of the actuator are not taken into account.

If small variations around a central position are considered, Equation (3.13) can be linearized. The first order linearization of F around $I = I_0$ and $S = S_0$ is:

$$\begin{aligned} F &= F(I_0, S_0) + \frac{\partial F}{\partial S} \bigg|_{I=I_0, S=S_0} \cdot \delta S + \frac{\partial F}{\partial I} \bigg|_{I=I_0, S=S_0} \cdot \delta I \\ &= K_M \cdot \frac{I_0^2}{S_0^2} - \frac{2K_M I_0^2}{S_0^3} \cdot \delta S + \frac{2K_M I_0}{S_0^2} \cdot \delta I \\ &= F_0 - K_C \cdot \delta S + K_I \cdot \delta I \end{aligned} \quad (3.16)$$

where

- F_0 = the premagnetisation force,
- K_C = the force-displacement factor, or negative stiffness, and
- K_I = the force-current factor.

The geometrical layout of the magnetic bearing dictates:

$$\begin{aligned} S_u &= S_0 + \delta z \\ S_d &= S_0 - \delta z \end{aligned} \quad (3.17)$$

For the implementation of the linearized currents the following is chosen:

$$\begin{aligned} I_u &= I_0 - \delta I \\ I_d &= I_0 + \delta I \end{aligned} \quad (3.18)$$

This implementation will lead to a force-current relationship for the total force on the rotor as shown in Figure 3.3. The total force on the rotor has a linear range from $\delta I = I_0$ to $\delta I = -I_0$.

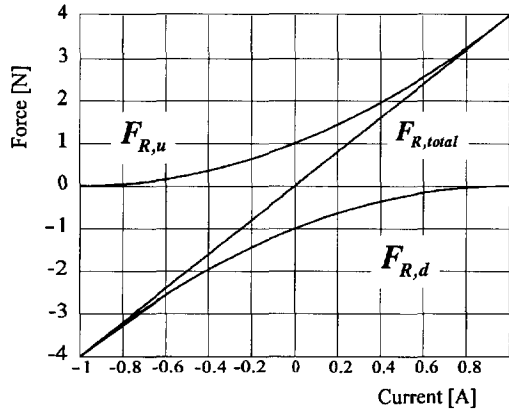


Fig. 3.3 A linear relationship between force and current is created by implementing the currents using Equation (3.18). The linear range varies from $\delta I = I_0$ to $\delta I = -I_0$.

Note that different implementation methods and linearization methods can be chosen here. They will be discussed in the Section 3.8.

Substituting Equation (3.16) through Equation (3.18) in Equation (3.15) gives the linearized differential equation for the magnetic bearing:

$$m \cdot \delta \ddot{z} = m \cdot g + 2K_c \cdot \delta z + 2K_I \cdot \delta I \quad (3.19)$$

This equation is called the magnetic actuator equation of motion and forms the basis of any magnetic bearing based upon magnetic reluctance actuators. This equation of motion is often written in the frequency domain notation using Laplace transform. It is then called a transfer function:

$$\delta z = \frac{m \cdot g}{m \cdot s^2 - 2K_c} + \frac{2K_I}{m \cdot s^2 - 2K_c} \cdot \delta I \quad (3.20)$$

The Laplace parameter s must be distinguished from the air-gap S .

Clearly two parts can be distinguished in this transfer function. A constant part caused by the gravitational force $m \cdot g$ and a variable part controllable with the current δI . The former is usually treated as a disturbance force and is left out of the transfer function. The second part is used in the next Section on stabilization.

3.4 Stabilization of magnetic bearings

The transfer function of Equation (3.20) has two poles, p_1 and p_2 . These poles are:

$$p_{1,2} = \pm \sqrt{\frac{2K_c}{m}} \quad (3.21)$$

The positive pole causes the actuator to be open-loop unstable. Therefore, a feedback control system is needed to stabilize the actuator.

The instability of the magnetic actuator can be explained with a theory originally developed by Earnshaw [21]. He proved that a system with just permanent magnets can not be stable. The system described by Equation (3.20) behaves like a permanent magnet system. The coil carrying I_0 can be replaced by a permanent magnet, thus resulting in a Type 3 force system (Section 2.4).

The instability caused by the positive pole must be corrected with a feedback loop and a controller. The state of the magnetic bearing must be measured and the choice of the specific state used in feedback will determine the type of the controller.

This thesis will present a controller based on the classical PID control with position feedback. The PID controller will be designed using the conventional methods described in [67] and [18].

The PID controller has the appearance of a Lead-Lag filter, also called tame PID controller. This approach will reduce the unwanted amplification of high frequency noise and the infinite amplification of a DC offset. The controller will be designed by first stabilizing the actuator with a PD controller. Integrating action or I-action will be added later on, if more static stiffness is desired.

The choice of the PID controller is not entirely arbitrary. Research done by [20] on the control of magnetic bearings clearly shows the benefits of a tame PID controller in combination with active magnetic bearings with position feedback.

The transfer function of a Lead filter, or tame PD controller, can be described as:

$$H_c(s) = P \cdot \frac{M_d(\tau_d s + 1)}{\tau_d s + M_d} \quad (3.22)$$

with

- M_d = the lead action index,
 τ_d = the derivative time constant, and
 P = the proportional gain.

When the Lead filter transfer function is multiplied with the process transfer function, the loop-gain function is obtained. A block diagram representing the magnetic bearing with feedback control is shown in Figure 3.4. In the Figure two extra components appear: The sensor and the amplifier. Assuming a constant transfer function of K_a and K_{sens} for amplifier and sensor, respectively, results in the following equation for the loop-gain function:

$$H_{lg}(s) = H_c(s) \cdot K_a \cdot H_p(s) \cdot K_{sens} \quad (3.23)$$

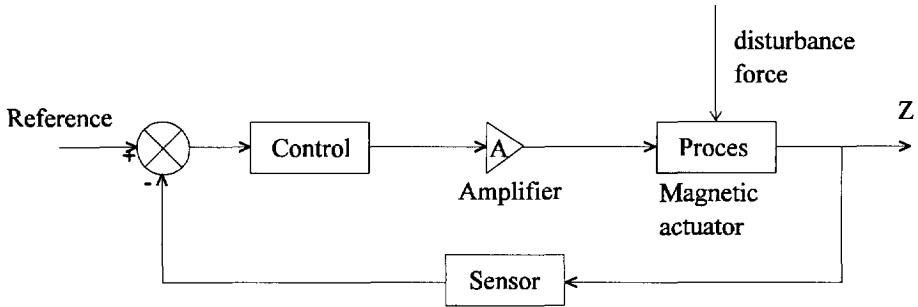


Fig. 3.4 Block diagram representing the closed loop active magnetic bearing.

Since the system is open-loop unstable, the frequency domain analysis may only be used if the stability is checked with Root Loci or Nyquist diagrams. The design of the controller is based on the desired shape of the loop gain function. The following steps have to be taken:

Choose a bandwidth f_b and a damping coefficient β for the closed loop transfer function. The choice of the closed-loop bandwidth and the damping is dictated by the application of the SPU. The 1 μm accuracy band of the SPU for example dictates a closed loop bandwidth of 100 Hz. Several other applications of the SPU can be thought of and each one leads to a specific set of specifications. A vibration isolation system built with SPU's will dictate a low bandwidth and a high damping for example.

Calculate the corresponding cross-over frequency f_c of the loop-gain transfer function with chosen bandwidth f_b by:

$$f_c = f_b \cdot \frac{(\sqrt{4\beta^2 + 1} - 2\beta^2)^{1/2}}{(1 - 2\beta^2 + \sqrt{2 - 4\beta^2(1 - \beta^2)})^{1/2}} \quad (3.24)$$

where

- f_c = the loop-gain cross-over frequency,
- f_b = the closed-loop bandwidth, and
- β = the relative damping.

Calculate the required phase margin, α_m , using:

$$\alpha_m = \tan^{-1} \left(\frac{2\beta}{(\sqrt{4\beta^2 + 1} - 2\beta^2)^{1/2}} \right) \quad (3.25)$$

Calculate the lead action index, M_d , according to:

$$M_d = \frac{1 + \sin \alpha_m}{1 - \sin \alpha_m} \quad (3.26)$$

Calculate the time constant, τ_d , of the controller using

$$\tau_d = \frac{1}{2\pi f_c} \sqrt{M_d} \quad (3.27)$$

Calculate the appropriate gain for the PD controller. The gain of the loop-gain function must be 1 at the crossover frequency, so the proportional gain of the controller can be calculated as:

$$P = \frac{1}{\text{mag}(H_{lg}(f_c))|_{P=1}} \quad (3.28)$$

Designing a PD controller with this strategy will result in a stable closed loop servo system. If the static stiffness of the closed loop system is not satisfactory, a Lag filter can be added to the controller. The transfer function of the Lead-Lag filter will then become:

$$H_c(s) = P \cdot \frac{(\tau_i s + M_i)}{(\tau_i s + 1)} \frac{M_d(\tau_d s + 1)}{\tau_d s + M_d} \quad (3.29)$$

where

M_i = the lag action index, and

τ_i = the integration time constant.

From Figure 3.4 two transfer functions for the closed loop process are derived: One process transfer function and one compliance transfer function. These functions are:

$$H_{cl}(s) = \frac{H_c(s) \cdot K_a \cdot H_p(s)}{1 + H_c(s) \cdot K_a \cdot H_p(s) \cdot K_{sens}} \quad (3.30)$$

and

$$C(s) = \frac{1/(ms^2 - K_c)}{1 + H_c(s) \cdot K_a \cdot H_p(s) \cdot K_{sens}} \quad (3.31)$$

Substituting Equation (3.29) as controller transfer function and Equation (3.20) as the open-loop transfer function in Equation (3.30) and Equation (3.31) results in:

$$H_{cl}(s) = \frac{a_0 + a_1 s + a_2 s^2}{b_0 + b_1 s + b_2 s^2 + b_3 s^3 + b_4 s^4} \quad (3.32)$$

and

$$C(s) = \frac{c_0 + c_1 s + c_2 s^2}{b_0 + b_1 s + b_2 s^2 + b_3 s^3 + b_4 s^4} \quad (3.33)$$

Both Equations, (3.32) and (3.33), are derived in appendix A.

The static stiffness of the magnetic bearing is of great interest. This static stiffness can be found with:

$$F(0) = 1/C(0) = P \cdot 2K_i \cdot K_a \cdot K_{sens} \cdot M_i - 2K_c \quad (3.34)$$

Equation (3.34) can be used to calculate M_i :

$$M_i = \frac{F(0) \cdot 2K_c}{P \cdot 2K_i \cdot K_a \cdot K_{sens}} \quad (3.35)$$

The distance between τ_d and τ_i is critical. The relation between τ_d and τ_i can be defined as:

$$K_{di} = \frac{\tau_i}{\tau_d} \quad (3.36)$$

Adding a lag action to the controller will result in some phase-loss at the cross-over frequency. [20] advises a maximum phase-loss of 5 degrees, but applications can be thought of where a different amount can be allowed.

The factor K_{di} can be read from the Figures in Appendix B, assuming a known phase-loss at the cross-over frequency, and a known M_i .

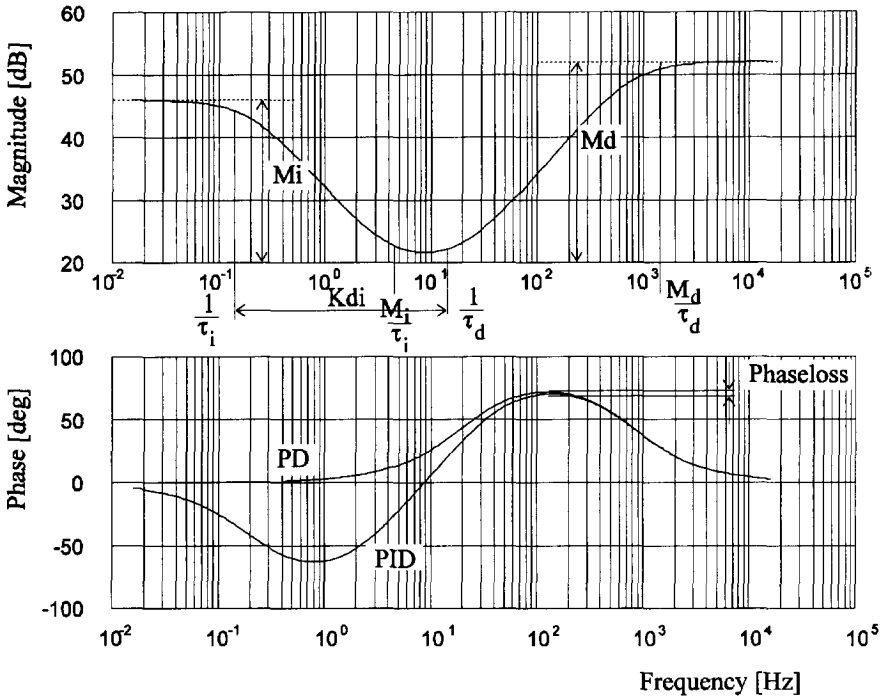


Fig. 3.5 Result of the design strategy for the tame PID controller. All parameters of a lead-lag filter, $\tau_i, \tau_d, M_i, M_d, K_{di}$ and P , are shown.

Figure 3.5 shows a schematic design of the Lead-Lag filter, also called tame PID controller. The parameters $\tau_i, \tau_d, M_i, M_d, K_{di}$ and P are shown.

If a magnetic bearing is implemented with the controller designed with this strategy, a stable system with the required specifications will be the result. If, however, an instability still occurs, it will be the result of one of the causes discussed below.

Most problems in an unstable magnetic bearing system are caused by unmodelled high frequency oscillations. The supported structure, or the support of the bearing itself may contain resonance frequencies. If the resonances are within the required bandwidth of the closed loop servo system, the model of the system must be upgraded in order to incorporate these frequencies and a completely new controller strategy must be used. [44] comments on this problem. These frequencies will cause resonance in the Bode plot of the loop gain function. This effect is shown in Figure 3.6. If the amplitude of the resonance frequency crosses the 0 dB line, then the structure will resonate at this frequency. This will cause bad system performance, or even instability. There are two alternative solutions to this problem. Either the loop gain must be decreased at the resonance frequency (extra filters or lower gain) or the resonance mechanism must be included in the model. This will give a better control over the resonance (provided it is controllable) but also a more complex controller.

The magnetic bearing may also become unstable due to eddy currents in the magnetic circuit. Eddy currents will introduce extra phase lag at high frequencies. This is not accounted for in the process transfer function. The phase margin created with the PD control will diminish, leaving insufficient damping, or instability. Again two alternatives are present to deal with eddy currents. Either the material should be laminated, thus preventing eddy currents to occur, or extra phase lead should be introduced using a PDD controller or a higher M_d .

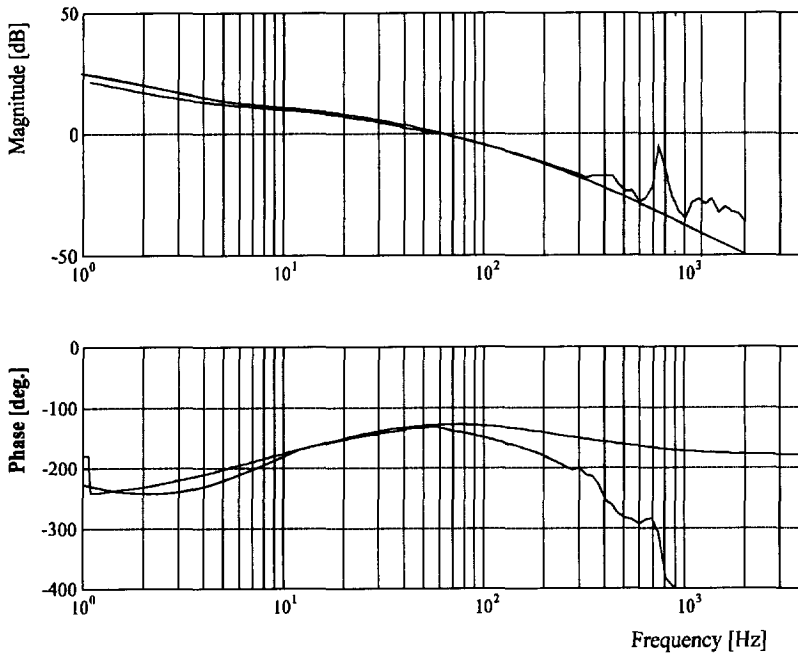


Fig. 3.6 Unmodelled high frequency oscillations. A magnetic bearing will start to vibrate at an unmodelled high frequency oscillation when the magnitude of the gain at this frequency is larger than 1. Unmodelled high frequency oscillations are usually caused by eigenfrequencies of the support structure or by eigenfrequencies of the supported mass.

If the controller is built using digital control hardware, caution should be taken with the controller design. Since the controller will work at discrete intervals, limited in speed, an anti-aliasing filter should be added to the system. This filter is usually a second order Butterworth filter or a Chebychev filter. Both filters introduce extra phase lag close to their bandwidths. The controller itself will introduce phase lag close to its sampling frequency. A rule of thumb is that controllers with half the sampling frequency can be built thus enabling closed loop control up to 1/5 of the sampling frequency.

Other limitations to the system like sensor bandwidth and amplifier bandwidth are not analyzed here. It is clear that both the sensor and the amplifier must have a bandwidth that is high enough.

3.5 Accuracy analysis of the magnetic reluctance force

The electromagnetic reluctance force depends on many parameters. Some parameters will not change during operation, others will. In order to correctly analyze the accuracy of the electromagnetic reluctance force, the following simple mathematical analysis can be used.

Equation (3.13) can be written as:

$$\frac{\Delta F}{F} = \frac{\Delta \mu_0}{\mu_0} - \frac{\Delta \mu_{r,air}}{\mu_{r,air}} + 2 \frac{\Delta N}{N} + \frac{\Delta A}{A} + 2 \frac{\Delta I}{I} - 2 \frac{\Delta \left(\frac{2x}{\mu_{r,air}} + \frac{(l_{iron1} + l_{iron2})}{\mu_{r,iron}} \right)}{\left(\frac{2x}{\mu_{r,air}} + \frac{(l_{iron1} + l_{iron2})}{\mu_{r,iron}} \right)} \quad (3.37)$$

Equation (3.37) shows that the relative error of each variable in the magnetic circuit has an effect on the relative error of the magnetic reluctance force. The plus and minus signs are of no importance, since the errors can be positive or negative. All the terms of Equation (3.37) will be analyzed, except μ_0 , for μ_0 is a physical constant that will not change.

3.5.1 Relative Permeability of air: $\mu_{r,air}$

The relative permeability of air depends on the air pressure, the air temperature and the air humidity. Research done by Bonse [15] shows that the permeability of air may change up to a factor of 10^{-4} . This way the force F is influenced by a factor of 10^{-4} as well.

3.5.2 Number of windings: N

The number of windings N will not change during operation of a magnetic actuator or a magnetic bearing. A counting error during manufacturing will therefore be the only possible source of error.

3.5.3 Cross-sectional area of the magnetic pole: A

The cross-sectional area A of the magnetic pole is not simply the geometric cross-sectional area. When the magnetic core is laminated, the isolation on each sheet of iron does not contribute to the cross-sectional area of the magnetic pole. This leads to a smaller area than geometrically measured.

Another effect is found when the magnetic circuit is heated. Ohmic resistance in the coil will lead to power dissipation and a rise in temperature of the magnetic circuit. This rise in temperature results in a change of the cross sectional area A . Assuming a linear expansion coefficient for steel of $12\text{e-}^6 \text{ K}^{-1}$ and a temperature rise of 10 K during operation, then the relative change of the cross-sectional area will be 1.44e-^8 .

3.5.4 The current I

The current directly influences the magnetic force. Any change in the current will therefore result in changes in the magnetic force. The current is provided by an amplifier. Two types of amplifiers can be used: A switching amplifier or a linear amplifier.

The switching amplifier is cheap, efficient and robust, but will always generate a ripple in the current supplied. A current ripple of 10% is not uncommon. The ripple depends on the inductance of the load. This means that the ripple may change during operation of the actuator. Adding a shunt inductance to the coil of the magnetic circuit will reduce the current ripple and is recommended by the amplifier manufacturers.

The linear amplifier shows a much more accurate behavior. There is no current ripple present. The linear amplifier is less efficient than the switching amplifier, more expensive and more sensitive to short circuiting and magnetomotive feedback. Magnetomotive feedback occurs when the inductance of a magnetic circuit changes very drastically. A changing magnetic field will induce a high voltage in the coil, thus feeding energy back into the amplifier.

When a magnetic bearing is designed without any constraints on accuracy, then the switching amplifiers are commonly used. High efficiency and low cost are then the most important aspects. If, however, the accuracy of magnetic positioning becomes important, then linear amplifiers should be used. A trade-off has to be made between cost and accuracy. More information on amplifiers is given in Chapter 5.

3.5.5 Magnetic flux paths: $\frac{2 \cdot x}{\mu_{r,air}}$ and $\frac{l_{iron}}{\mu_{r,iron}}$

The contribution of the magnetic flux paths, divided by their relative permeability, is the last term to be analyzed. Fluctuations in $\mu_{r,air}$ were analyzed before. The fluctuations in $\mu_{r,iron}$ will be discussed below.

The relative permeability of iron, $\mu_{r,iron}$, is usually set at a high value, between 5000 and 100,000. If this is done, then the influence of $l_{iron}/\mu_{r,iron}$ becomes negligible compared to $2 \cdot x/\mu_{r,air}$, and the whole contribution of the iron to the magnetic force is neglected. If the relative permeability decreases (at saturation of the iron or at high temperatures) or materials with a low μ_r are used, then the influence can not be neglected. The influence on the magnetic force increases and an estimate of the length of the iron flux path should be made.

The length of the flux path in iron can be large compared to the length of the flux path in air. It is not simply the geometric length of the magnetic circuit. Figure 3.7 shows the E-I magnetic circuit with two possible flux paths: $l_{iron,max}$ and $l_{iron,min}$.

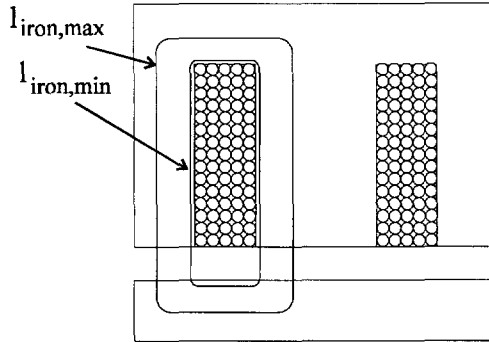


Fig. 3.7 E-I magnetic circuit with two possible average flux paths, $l_{iron,max}$ and $l_{iron,min}$. At low magnetic field densities, the magnetic flux will tend to follow the shortest path, $l_{iron,min}$. If the magnetic field density increases, then the average flux path will also increase, until $l_{iron,max}$ is achieved at saturation flux densities.

When the magnetic field density in the iron parts of the magnetic circuit is low, then the flux will tend to follow the shortest path possible. This is a well known feature of flux. When the magnetic field density increases, the danger of

saturation will cause the flux to spread out. The average flux path will grow, and finally reach $l_{iron,max}$. The length of the flux-path $l_{iron,max}$, which equals the mean of the geometric flux path, will be reached at the saturation field density.

The influence of the air-gap on the magnetic force is next to be analyzed. The air-gap is the average length of the flux paths in air. This means that leak flux should be taken into account. A good magnetic circuit design will keep leak flux to a minimum. Figure 3.8 shows a good design of a magnetic circuit versus a bad design. The two designs of Figure 3.8 were analyzed using a finite element analysis system for electromagnetic fields. By keeping the air-gap within 10% of the magnetic pole width, the stray flux will be minimized and the air gap equals the geometric distance between stator and rotor. This is shown in Figure 3.8.a. The design of Figure 3.8.b shows a poor magnetic circuit design. The length of the flux-paths in air is very difficult to determine. Measurement of the force is necessary in order to determine a working force-current relationship for this set-up.

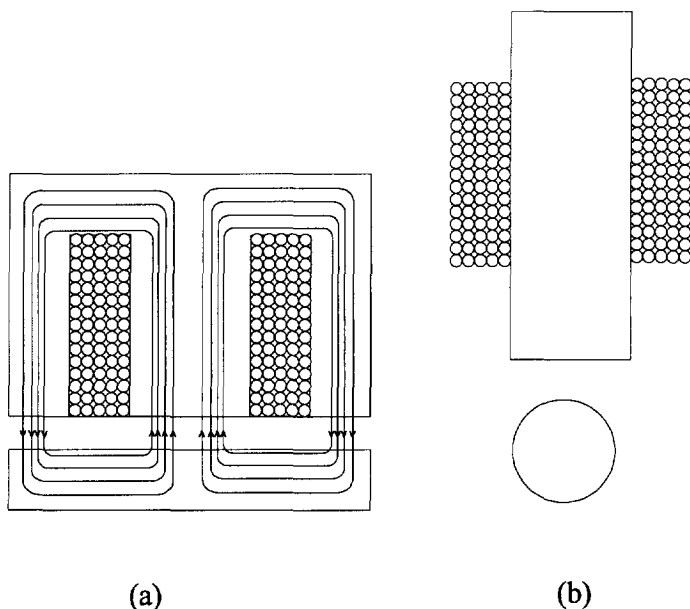


Fig. 3.8 Two side views of magnetic circuit designs: (a) was used in a magnetic bearing set-up and has a well defined magnetic circuit. (b) was used in a floating ball set-up [69] and has a poorly defined magnetic circuit.

Taking the abovementioned into account, the following recommendations can be made:

- Keep the air-gap x small compared to the pole-width of the magnetic circuit (typically below 10%). This will reduce the influence of stray magnetic flux and therefore eases the calculation of the magnetic force.
- Keep the magnetic induction well below the saturation level of the iron used as magnetic conductor. This will assure a relatively constant $\mu_{r,iron}$ and a constant I_{iron} along the working range of the actuator. The value for I_{iron} can be estimated from computer simulations or from a force calibration of the set-up.
- Invest in good magnetic materials. This will result in good system behavior, for the value of the parameters in Equation (3.13) will be known more accurately, compared to the case where poor magnetic materials are used.

3.6 Practical limitations to magnetic reluctance forces of the SPU

The magnetic reluctance force can be calculated using Equation (3.13) derived in Section 3.2. All variables in this Equation are not only subject to close inspection regarding the influence on the accuracy of the force, but should also be examined with regard to their practical limitations. These practical limitations will be discussed in this Section.

3.6.1 Maximum magnetomotive force

The magnetomotive force, given by the product $N \cdot I$, forms the first factor to limit the maximum magnetic force. Assuming that a certain space around the central magnetic pole is reserved for the coil, the following calculation can be made:

Assume a cross-sectional area of Q , reserved for the coil. The number of windings that fits in this area can be calculated with:

$$N = \frac{Q}{q_{total}} \quad (3.38)$$

where

q_{total} = the practical cross sectional area occupied by one winding, consisting of the winding, the electrical isolation and of open areas between windings.

The total area occupied by one winding is shown in Figure 3.9. Assuming a square distribution of the wires, as shown in Figure 3.9.a, is allowed. A hexagonal close packing distribution, as shown in Figure 3.9.b, will not occur. The fact that different layers of the coil have opposite propagation directions (Figure 3.9.c) opposes this distribution. [33] shows that so-called "orthocyclic winding" leads to the winding distribution of Figure 3.9.6. However, the special equipment necessary to achieve orthocyclic winding is not commonly available and the winding scheme of Figure 3.9.a will be the most common scheme. The distribution of the wires in a square, as shown in Figure 3.9.a is the practical solution.

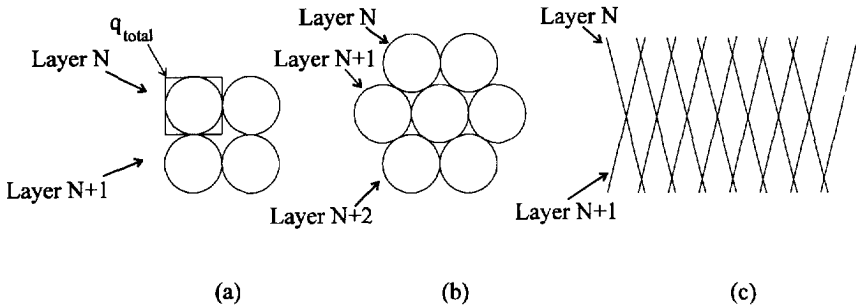


Fig. 3.9 Two possible wire distributions are shown in cross-section: a square distribution (a) and a hexagonal distribution (b). Figure (c) shows that the opposite propagation directions of the different layers of the coil prohibit a hexagonal distribution and permit the square distribution.

The maximum current flowing through a thread can be estimated with the rule of thumb that the maximum current density through a wire should not exceed 10A/mm^2 . This way, burning of the isolation of the wires is prevented. The current can be calculated with:

$$I_{max} = J_{max} \cdot q_{copper} \quad (3.39)$$

where

J_{max} = the maximum current density = 10 A/mm².

q_{copper} = the cross-sectional area of copper.

The following relationship exists for the total wire radius:

$$r_{total} = r_{copper} + d_{isolation} \quad (3.40)$$

where

r_{total} = the total wire radius,

r_{copper} = the copper radius,

$d_{isolation}$ = the thickness of isolation layer.

and

$$q_{copper} = \pi \cdot r_{copper}^2 \quad (3.41)$$

The maximum magnetomotive force is given by:

$$(N \cdot I)_{max} = \frac{Q \cdot J_{max} \cdot \pi \cdot r_{copper}^2}{4 \cdot (r_{copper} + d_{isolation})^2} \quad (3.42)$$

Assuming an isolation thickness of 50 micrometer, a graph, shown in Figure 3.10, shows the value for $(N \cdot I)_{max} / Q \cdot J_{max} \cdot \pi/4$.

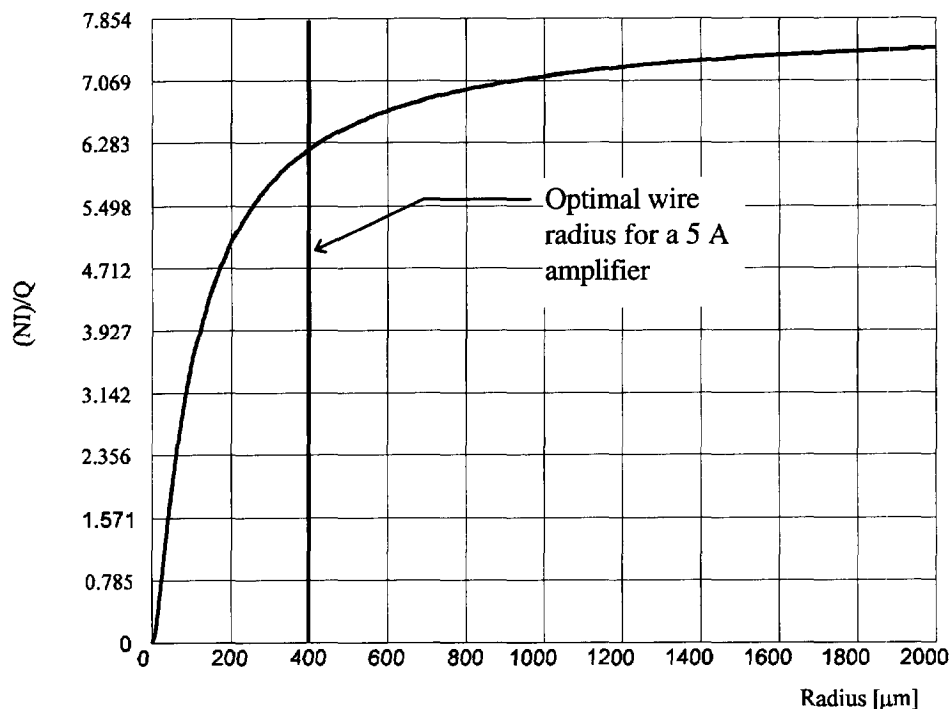


Fig. 3.10 The relationship between maximum magnetomotive force $(N \cdot I)_{\max} / Q \cdot J_{\max} \cdot \pi/4$ and the copper radius of a wire, assuming an isolation thickness of $50 \mu\text{m}$, and a maximum current density of 10 A/mm . The vertical line shows the limitation created by an amplifier with 5 A maximum output current.

The graph of Figure 3.10 suggests to take the diameter of the wire as large as possible. The current I will then be as large as possible.

The current through the coils of a magnetic bearing is provided by an amplifier. Limitations of every amplifier include maximum output current and maximum output voltage. The voltage is needed to drive the current through the coil, and can be calculated with:

$$V = I \cdot R + L \cdot \frac{dI}{dt} + K \cdot v \quad (3.43)$$

where

- V = the voltage needed to drive the current through the coil,
 I = the current,
 R = the ohmic resistance,
 L = the inductance of the coil,
 K = a constant, and
 v = the velocity of suspended object.

The inductance, L , of the coil is represented by:

$$L = \frac{\mu_0 \cdot N^2 \cdot A}{\frac{2 \cdot x}{\mu_{r,air}} + \frac{l_{iron}}{\mu_{r,iron}}} \quad (3.44)$$

The last factor in Equation (3.43) is commonly neglected in magnetic bearings, leaving the resistance voltage drop and the inductance voltage drop. In most magnetic bearing designs, the contribution of $I \cdot R$ is typically below 10% and the contribution of $L \cdot dI/dt$ is about 90%. Using this fact, a choice can be made for the number of windings.

Equation (3.43) clearly shows that L should be kept low. This implies (Equation 3.44) that N should be kept low too. A low N means a large diameter of the wire and thus a high current. Power amplifiers have a limited current output, thus enforcing a limited maximum wire diameter and a minimum number of windings. The optimum is found when the current through the wire matches the maximum amplifier current.

3.6.2 Maximum magnetic field density

The second limitation is formed by the maximum field density of the magnetic circuit. The magnetic field density can be calculated with:

$$B = \frac{\Phi}{A} = \frac{\mu_0 \cdot N \cdot i}{\frac{2x}{\mu_{r,air}} + \frac{(l_{iron1} + l_{iron2})}{\mu_{r,iron}}} \quad (3.45)$$

This Equation shows that a high $\mu_{r,iron}$, will make it easier to achieve a high magnetic field B . But the maximum magnetic field density is limited by the saturation field density, B_{sat} , of the magnetic circuit. Depending on the material used, low B_{sat} of 0.5 T or high B_{sat} of 2.4 T will be achieved. The relative permeability $\mu_{r,iron}$ is not constant, but will drop to 1 at B_{sat} .

Rewriting (3.6) using (3.7) leads to:

$$F_R = \frac{B^2 \cdot A}{\mu_0 \mu_{r,air}} \quad (3.46)$$

This Equation clearly shows that the maximum force is limited by the maximum magnetic field density of the magnetic circuit. A high $\mu_{r,iron}$ will diminish the current needed to achieve a high field density and it will bind the magnetic flux to the magnetic circuit. This guarantees that the flux will cross the air-gap at the correct place.

The next Section will discuss the relationship between the relative permeability of the magnetic circuit, $\mu_{r,iron}$, and the maximum magnetic field density, B_{max} .

The last practical limitation to the magnetic force is caused by eddy currents. The limitation caused by eddy currents takes effect only at relatively high frequencies. It therefore limits the dynamic characteristics of the force generation.

When the magnetic field changes, a current will be induced in a conductor in the magnetic field. This effect results in a force of Type 6, Chapter 2. The eddy current generates heat, and thus consumes energy provided by the magnetic field. The force F_R will therefore be smaller, and a phase lag will be introduced. This is of great importance when the force is to be used to stabilize the magnetic bearing. The eddy currents will flow in a plane perpendicular to the magnetic flux. The best way to assure that eddy currents will be small is by making the electric resistance of the circuit high. This can be done by laminating the magnetic circuit, or by choosing a non-conducting material like ferrite, which is specially developed for this purpose.

More information on practical limitations can be found in [46].

3.7 Magnetic properties of materials for magnetic bearings

When a homogenous material is placed in a homogenous magnetic field with strength H , a magnetic field density will be generated in this material according to:

$$B = \mu_0 \cdot \mu_r \cdot H \quad (3.47)$$

It seems that the material assists the field H in building a flux density B . This "assistance" is called magnetic polarization J :

$$J = (\mu_r - 1) \cdot \mu_0 \cdot H = \chi_m \cdot \mu_0 \cdot H \quad (3.48)$$

where

χ_m = magnetic susceptibility.

Materials with $\chi_m < 0$ are called diamagnetic materials. These materials are rare and not useful in this research. Materials with $\chi_m > 0$ are called paramagnetic materials and are of great interest for magnetic bearings. In some paramagnetic materials $\chi_m \gg 0$. These materials with $\mu_r \gg 1$ are called ferromagnetic materials and they are commonly used in magnetic circuits.

In ferromagnetic materials the atomic moments (causing the magnetic polarization) are coupled and are arranged parallel in domains. Each domain, called Weiss domain, contributes to the polarization. The transition zones between the Weiss domains, where the atomic moments change direction, are called Bloch walls.

The behavior of paramagnetic materials is usually visualized in a B-H diagram. Figure 3.11 shows such a diagram. When an unmagnetized ferromagnetic material is placed within a magnetic field with an increasing magnetic field strength, H , the flux density B increases along the initial curve. The Bloch walls shift and the Weiss domains grow. Domains having their privileged direction parallel to the field direction expand, at the expense of the others.

If H keeps increasing, the flux density also keeps increasing, until all the Weiss domains have obtained the same direction. Once all the magnetic dipoles are parallel to the outer magnetic field, saturation is achieved, and B only increases with a slope μ_0 . This is shown in Figure 3.11.

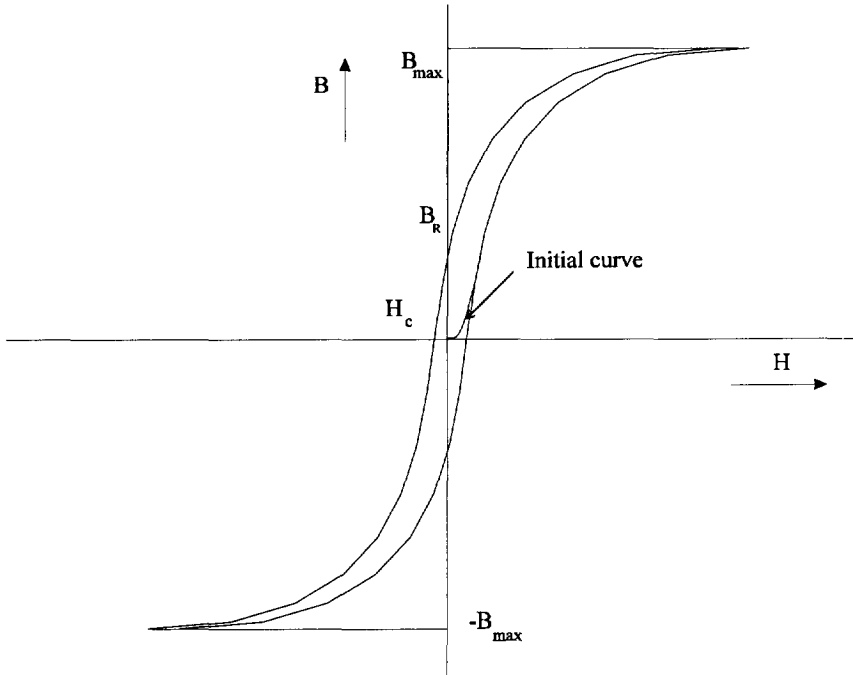


Fig. 3.11 B-H curve of a magnetic material, showing the saturation effects that occur at high field strengths. The initial curve shows the B-H relationship when the material is magnetized for the first time. The coercivity H_c and the remanent magnetism B_r are a measure for the hysteresis of the magnetic material.

When the outer field is reduced, the flux density does not run along the initial curve, but follows a hysteresis loop. Before reaching $H = 0$, some of the Bloch walls will shift, thus allowing Weiss domains with different orientation. The magnetic polarization, J , is reduced, but not entirely canceled out. Some remanent magnetism will remain at $H = 0$. This is called the remanence, B_r . If H is increased in the opposite direction, more Bloch wall shifts and reorientation of Weiss domains will occur. The magnetic field density drops until at some point it reaches zero. The magnetic field strength at which this happens is called coercive field strength H_c , or coercivity. With increasing intensity of the field, the material is magnetized until saturation occurs in the opposite direction. By

resetting the field to zero and by increasing it subsequently in the original direction, saturation is achieved again and the hysteresis loop has been formed.

When a magnetic actuator is built, one needs ferromagnetic material to guide the magnetic field. Several magnetic materials have been developed, each for specific reasons. The three most important properties that magnetic material should have for magnetic actuators are:

- high magnetic saturation level,
- high relative permeability, and
- low hysteresis, or low coercitive field strength.

The materials with low hysteresis are also called soft magnetic materials, while materials with a lot of hysteresis are called hard magnetic materials. Hard magnetic materials are commonly used for permanent magnets. Figure 3.12 shows an overview of magnetic materials. More information can be found in [70].

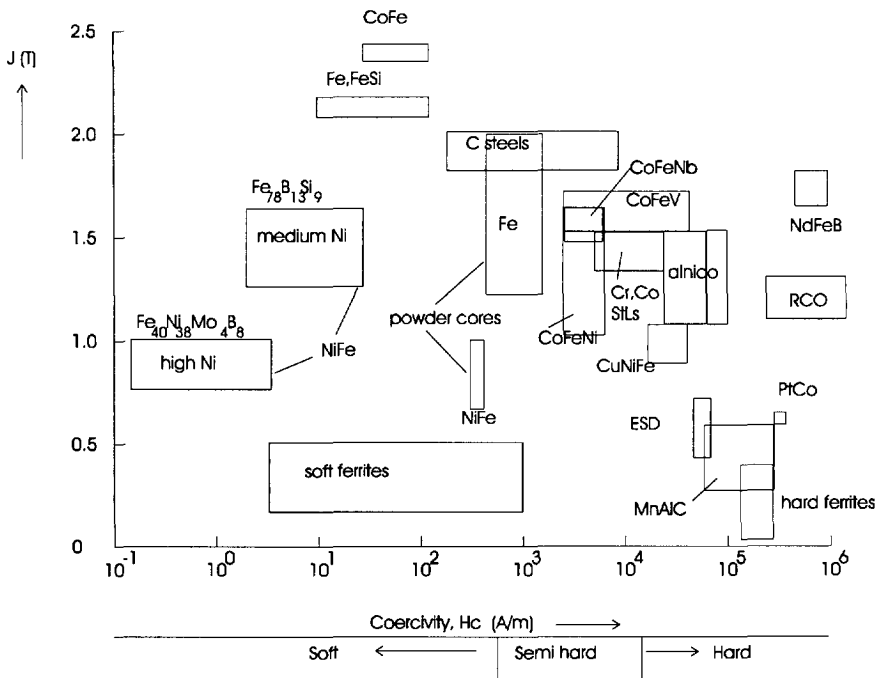


Fig. 3.12 Overview of magnetic materials, taken from [43], showing Coercivity and magnetic polarization. Soft materials are used for magnetic circuits. Hard materials are commonly used for permanent magnets.

Hard magnetic materials are not suited for magnetic bearings. The high hysteresis will cause poor controllability of the magnetic circuit. This can be understood when taking the example, of the magnetic field density in the bearing being reduced to zero, after having been at a high relative value. Decreasing the magnetic field strength to zero by decreasing the current through the coil to zero, will not result in a zero magnetic field density B , and therefore not in a zero force F . Increasing a negative current, until H_c is obtained, will result in zero force. This means that energy is lost caused by the hysteresis of the B-H curve.

Soft magnetic materials are better suited for the magnetic circuit of a magnetic bearing. A high relative permeability μ_r will assist the magnetic field in order to obtain a high magnetic field density. The magnetic resistance of a magnetic circuit, given by

$$R = \frac{l}{A \cdot \mu_0 \cdot \mu_r} \quad (3.49)$$

will be low at a high μ_r . This will confine the flux to the circuit and thus reduce stray flux-losses.

The level of magnetic saturation is also important, especially when high forces are to be obtained. When designing a magnetic circuit for a magnetic bearing, it is usually recommended to design for a working point at $B_{max} / 2$. This will result in good linear behavior of the magnetic actuator and enough room for obtaining forces of different levels. An overview of soft magnetic materials for magnetic bearings has been given by [25].

Important properties for common magnetic bearing materials are given in table 3.1.

material	rel. permeability	saturation flux density
SiFe	2000-6000	1.2-1.8 T
CoFe	2000-7000	2.0-2.4 T
NiFe	30,000-100,000	0.8-1.5 T

Table 3.1. Overview of properties of common magnetic bearing materials.

3.8 Linearization methods for magnetic bearings

The magnetic bearing non-linearities originate from:

- the force not being proportional to the current (square function),
- the magnetic flux density being subjected to saturation,
- the magnetic field density showing hysteresis, depending on the magnetic material,
- the occurrence of high frequency eddy currents, and
- the amount of leakage of the flux depending on the air-gap size.

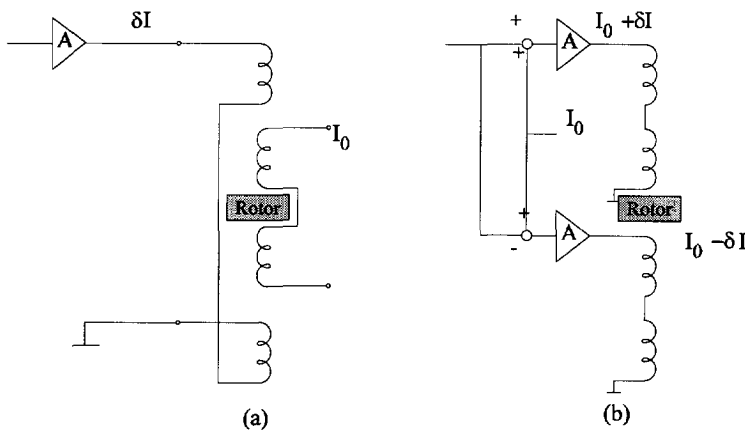


Fig. 3.13 Two implementation methods of the first-order linearisation of the magnetic bearing force (Class A control). (a) shows the stationary current flowing through coils, separated from the control current. The coils are differentially wound in order to get the correct implementation. Only one amplifier is needed together with a stationary current source.

(b) shows an implementation where the upper and the lower coil are both fed with their own current amplifier. Using this strategy two amplifiers are necessary.

Linearization of magnetic bearings is needed if one wants to use classical control strategies. The first-order linearisation, discussed in Section 3.4, results in a stationary current I_0 (working point) and a control current δI . Two possible implementation methods of the first order linearisation (commonly called Class A control) are shown in Figure 3.13.

The first method shown in Figure 3.13.a, uses a set of differentially wound coils. The coil of the magnetic actuator is divided in two parts. One part carries the stationary current, and one part carries the control current. By combining stationary current carrying coil of upper and lower half, and doing the same for the control current carrying coils, the configuration of Figure 3.13.a is obtained. This layout has two advantages:

- only one amplifier is needed, and
- the absolute values of the currents in upper and lower coils are always identical, thus eliminating a source of error.

The second implementation of the first order linearisation is shown in Figure 3.13.b. Implementation is achieved here by calculating or adding the appropriate currents for the upper and lower half of the magnetic actuator and sending them through the respective coils. The result is that two amplifiers are needed and that offsets or different gains of the amplifiers will result in inaccurate implementation of the linearisation method.

A third implementation will be mentioned here, called Class B control. It has been described in [62] and [20] and uses a non-linear control strategy. The nonlinear behavior of the magnetic force is linearized by taking the square root of the control signal. Thus, a linear force-current relationship is obtained. The influence of the air-gap on the force is taken out by multiplying the control signal with the square of the position measured. Thus, the force-displacement relationship is linearized. Figure 3.14 shows how this implementation results in the use of two amplifiers, leaving the same disadvantages as for the second implementation method shown in Figure 3.13.b.

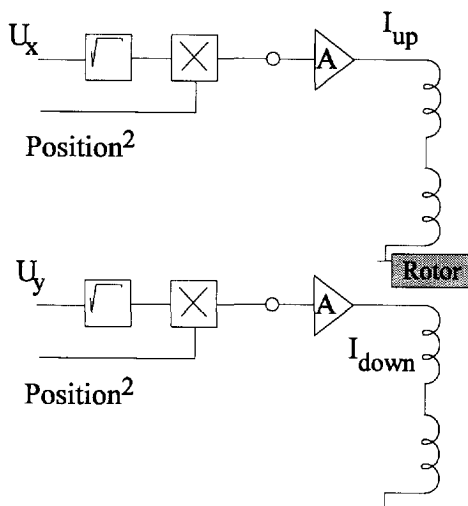


Fig. 3.14 Nonlinear implementation method of the electromagnetic reluctance force (class B control). The square-root linearises the force-current relationship and the multiplier linearises the force-displacement relationship.

The SPU uses Class A control. The choice is quite obvious: The SPU needs a constant bias magnetic field for propulsion. This field is provided only if Class A control is used. The implementation of Class A control is done with a set of differentially wound coils, for this requires one amplifier only.

3.9 Performance limitations of magnetic bearings

Before designing a magnetic bearing unit it is advisable to understand its limitations. This paragraph will describe some aspects of magnetic bearings related to those limitations.

3.9.1 Static bearing load capacity

Virtually any load can be supported by magnetic bearings. The limitations are formed by the maximum field density that can be achieved and the cross-section of the magnetic poles, as was shown in Section 3.6. It is common practice to reserve 50% of the maximum magnetic field density for the static load, and 50 % for the dynamic compensations. If generating the static part of the magnetic field

poses a problem, permanent magnets can be used for this. Examples of loads as small as a few gram up to multi-ton loads have been described in [11] and [59], respectively.

3.9.2 Static and dynamic stiffness

The static and dynamic the stiffness of the magnetic bearing are defined by the controller layout and characteristics. If an Integrating action is incorporated into the controller, an infinite static stiffness can be reached. In this case the maximum stiffness of the system will not be determined by the magnetic bearing, but by the support structure surrounding it. The dynamic stiffness cannot be designed to be infinite. It will have its lowest value near the closed-loop system bandwidth, and it is mainly characterized by the controller. If the design is aimed at getting a high dynamic stiffness, stiffnesses up to 10^8 N/m can be achieved. More information on the dynamic stiffness can be found in [16].

At the other end, the question can be asked how low the stiffness can be. Since the uncontrolled stiffness is negative, this seems to be no problem. If very low stiffness is sought, typically just above zero, more problems can be expected then when a high stiffness design is aimed at. First of all a layout should be designed where the mass of the suspended object can be compensated for. The force supporting the load should be almost independent of the position (implying zero stiffness). Secondly, the system should remain stable, even if small changes occur in the environment, which may occur due to all kinds of effects. This will not be researched here, but some basic calculations can be found in [9].

3.9.3 Damping

The damping of a magnetic bearing is obtained from the controller characteristics. This implies that it can take any value desired, from negative, through zero to positive.

3.9.4 Position accuracy

Since magnetic bearings depend on a closed loop servo system to achieve stability, the performance of position sensor and amplifier will directly affect the accuracy of the system. Slocum [57] writes: *"With new high-speed digital signal processor technology and better sensors for fine position sensing, there is no reason why nanometer and better accuracy cannot be obtained if one wanted to pay for it."* This theorem was tested with success at the Laboratory for Micro

Engineering [66]. High position accuracy was achieved, under laboratory conditions. Position accuracy of 5 nm was achieved while a vibration isolation was applied, along with suitable sensors.

4 Magnetic propulsion

4.1 Introduction

The usual approach to the design of a suspension and propulsion system can be summarized as:

- design the suspension, and
- add the propulsion.

The two functions are usually designed or purchased independently. This is the easiest way and will allow a fast design process. Care should be taken that unwanted mutual interaction between the suspension and propulsion systems does not degrade the overall system performance.

A more unconventional approach to designing a suspension and propulsion system is when both aspects are integrated into one design. A good model of the overall system is necessary, for the design will be more complex, since more degrees of freedom have to be considered.

A literature search yielded two designs of suspension and propulsion systems that were integrated. One design combines Lorentz forces into a suspension and propulsion system for rotating motors [10]. The other design combines a linear stepper motor with a magnetic bearing [37], where reluctance forces are used to achieve suspension and propulsion.

This thesis presents a design of a Suspension and Propulsion Unit where suspension and propulsion are integrated into one element. The basic magnetic bearing unit, described in Chapter 3, is extended with an extra set of coils on the rotor. These “secondary coils” interact with the magnetic field provided for the magnetic suspension. Interaction of these coils with the magnetic field results in a

propulsion force. Thus, this magnetic field is used twice: one time for suspension and one time for propulsion.

4.2 The Lorentz force

When a conductor carrying a current is placed inside a magnetic field, a force will be generated, called the Lorentz force, that can be described by:

$$F_L = Q \cdot (E + v \times B) \quad (2.2)$$

where

F_L = the Lorentz force,

Q = the charge,

E = the electric field,

v = the velocity of moving charge, and

B = the magnetic field density.

The effects of the electric field E on a moving charge Q can be neglected in macroscopic systems. Neglecting E and writing $Q \cdot v$ as the current I results in:

$$F_L = I \times B \quad (2.3)$$

Figure 4.1 shows a layout of a Lorentz force generator.

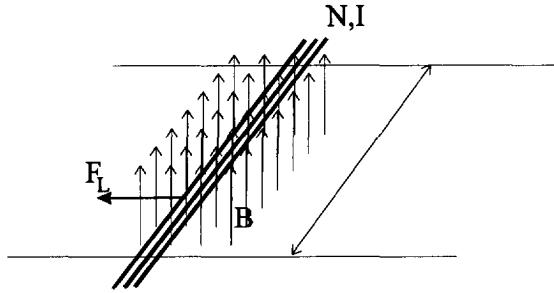


Fig. 4.1 A set of N parallel conductors carrying a current interacts with a magnetic field B and produces a Lorentz force F_L .

Figure 4.1 shows N wires, each of them carrying a current I . This results in a force generation of:

$$F_L = N \cdot I \times B \quad (4.1)$$

The outer product of current and magnetic field results in a force perpendicular to both current and magnetic field, whose direction can be found using the right-hand convention. The magnetic reluctance force resulting from these simplifications can be described as:

$$F_L = N \cdot l \cdot I \cdot B \quad (4.2)$$

where

l = the length of the conductor inside the magnetic field.

When a Lorentz force needs to be generated, a conductor is needed, (in combination with a current source) and a magnetic field. This magnetic field can be generated with a permanent magnet or with an electromagnet. Together with this magnetic source, a magnetic circuit is needed to guide the magnetic field to the desired location.

4.3 Secondary coil position within the SPU

When the magnetic bearing actuator of Figure 4.2a is considered, the question arises how the Lorentz force can be generated. Placing extra coils on the rotor, and assuring they interact with the magnetic field of the bearing, results in the generation of a Lorentz force. The generation of the Lorentz force takes place inside the air-gaps.

The magnetic field generated by the coils on the stator (from now on called primary coils) flows through the magnetic circuit and crosses the upper and lower air-gap at three places. At the central magnetic pole, the flux generated by the upper primary coil is directed in a upward direction, while at the outer two magnetic poles the flux is directed in a downward direction. This means that the current flowing through the coils placed on the rotor inside the air-gap (from now on called secondary coils) must have opposite directions near outer and center magnetic pole.

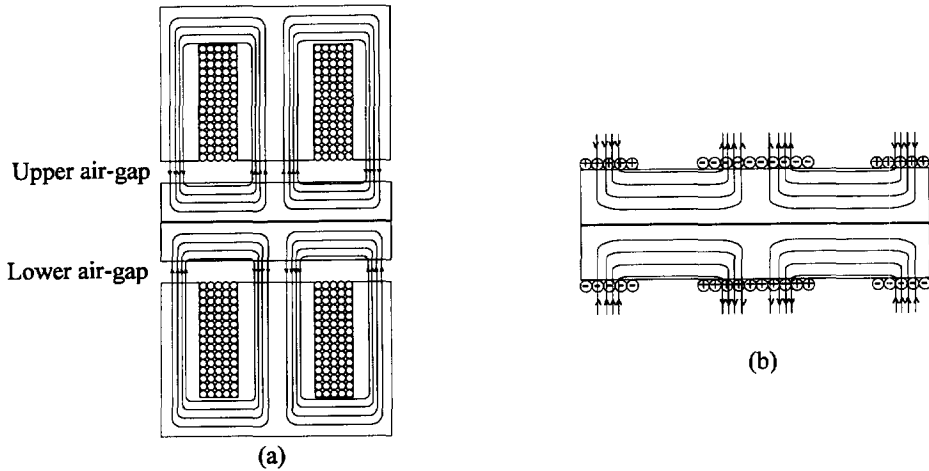


Fig. 4.2 The magnetic bearing actuator has an air-gap where the magnetic field can also be used for generating a propulsion force (a). A Lorentz force is generated when so-called secondary coils are placed on the rotor (b). The + and - signs show the direction of the currents flowing through the coils.

Figure 4.2b shows a schematic view of the Suspension and Propulsion Unit with the primary and secondary coils. The signs “+” and “-” show the direction of the current in the coils. A “+” indicates a current coming out of the plane of drawing, while a “-” means a current flowing into the plane of drawing. A complete picture of the suspension and propulsion unit is shown in Figure 4.3.

Figure 4.3 shows primary and secondary coils. The secondary coil is divided into three parts. The center part must be wound in opposite direction from the outer parts. Thus, the opposite direction of the magnetic field at the center magnetic pole, compared to the two outer magnetic poles, is compensated for.

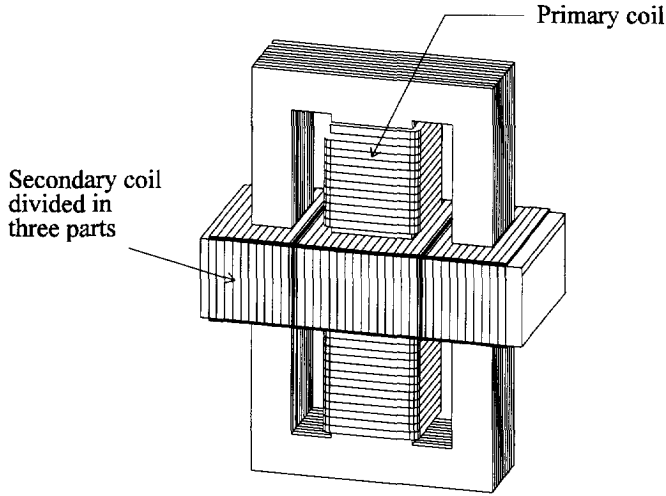


Fig. 4.3 The complete SPU. The secondary coils are wound around the rotor, thus assuring that the Lorentz force is generated inside the air-gap. Three parts of secondary coil can be distinguished. The central part is wound in an opposite direction from the two outer parts to compensate for the changing flux direction. The support structure of the stator parts is not shown.

The magnetic field density inside the air-gap of the magnetic bearing has been described in Chapter 3. There, it was found that the magnetic field density can be calculated with:

$$B = \frac{\mu_0 \cdot N \cdot i}{\frac{2 \cdot z}{\mu_{r,air}} + \frac{(l_{iron1} + l_{iron2})}{\mu_{r,iron}}} \quad (4.3)$$

If the effect of the iron on the magnetic path is neglected, this equation can be written as:

$$B = \frac{\mu_0 \cdot \mu_{r,air} \cdot N \cdot i}{2 \cdot z} \quad (4.4)$$

The magnetic field in the upper air-gap can be different from the magnetic field in the lower air-gap, when external forces are to be compensated. A distinction in

B_u and B_d must therefore be made. A combination of Equation (4.2) and Equation (4.4) results in:

$$F_l = \frac{\mu_0 \cdot \mu_{r,air} \cdot N \cdot I}{2Z} \cdot I_{sec} \cdot l \cdot N_{sec} \quad (4.5)$$

Figure 4.2a showed that there are three places in the upper air-gap that produce a Lorentz force of effectively four times F_l , and three places in the lower air-gap, also producing a Lorentz force of four times F_l . Therefore, an upper and a lower Lorentz force can be calculated assuming all secondary coils carry the same current I_{sec} :

$$F_{lu} = 4 \cdot B_u \cdot I_{sec} \cdot l \cdot N_{sec} \quad (4.6a)$$

and

$$F_{ld} = 4 \cdot B_d \cdot I_{sec} \cdot l \cdot N_{sec} \quad (4.6b)$$

where

F_{lu} = the Lorentz force generated in upper air-gap, and

F_{ld} = the Lorentz force generated in lower air-gap.

The magnetic field densities in the air-gaps can be found by combining Equation (4.4) with Equation (3.17) and Equation (3.18):

$$B_u = \mu_0 \cdot \mu_{r,air} \cdot N \cdot \frac{I_0 - \delta I}{2(S_0 + \delta Z)} \quad (4.7a)$$

and

$$B_d = \mu_0 \cdot \mu_{r,air} \cdot N \cdot \frac{I_0 + \delta I}{2(S_0 - \delta Z)} \quad (4.7b)$$

Substituting Equation (4.7) in (4.6) and adding the upper and lower Lorentz force, yields:

$$F_L = 2 \cdot N \cdot \mu_0 \cdot \mu_r \cdot I_{sec} \cdot N_{sec} \cdot b \cdot \left\{ \frac{(I_0 - \delta I)}{(S_0 + \delta Z)} + \frac{(I_0 + \delta I)}{(S_0 - \delta Z)} \right\} \quad (4.8)$$

4.4 Stabilization of the propulsion system

The propulsion force calculated in Section 4.3 can be used to position the rotor of the SPU. This can be done by measuring the position of the rotor and then controlling it in a feedback loop. The actuator that is created this way behaves exactly the same as a PM servo controlled linear DC motor. The control force can be calculated with Equation (4.8). By assuming that the magnetic bearing controls δZ to zero, Equation (4.8) can be simplified to:

$$F = K_M \cdot I_{sec} \quad (4.9)$$

Analysis of the assumption that δZ will be made in the next Section.

The constant K_M is called the motor constant and can be described by:

$$K_M = 2 \cdot N \cdot \mu_0 \cdot \mu_{r,air} \cdot I_{sec} \cdot N_{sec} \cdot b \cdot I_0 \cdot q \quad (4.10)$$

where

- K_M = a motor constant,
- N = the number of primary windings,
- μ_0 = the permeability of vacuum,
- $\mu_{r,air}$ = the relative permeability of air,
- I_{sec} = the secondary coil current,
- N_{sec} = the number of secondary windings inside the magnetic field,
- b = the width of secondary winding inside the magnetic field,
- I_0 = the primary coil stationary current, and
- S_0 = the nominal air-gap.

The equilibrium of forces can be calculated using Newton's law. This leads to the dynamic equation of motion:

$$m \cdot \ddot{x} = K_M \cdot I + F_{ex} \quad (4.11)$$

where

- m = the mass of the suspended rotor,
- x = the position of the rotor, and
- F_{ex} = the sum of the external forces.

Two transfer functions can be derived from Equation (4.11). These are the position transfer function:

$$H_x(s) = \frac{K_M}{m \cdot s^2} \quad (4.12)$$

and the compliance transfer function:

$$C_x(s) = \frac{1}{m \cdot s^2} \quad (4.13)$$

Controlling the position transfer function can be done in exactly the same way as controlling the position transfer function of the magnetic suspension. The same design strategy for the controller is used in this case. The application of the Lead-Lag filter will lead to the following closed loop transfer function:

$$H_{cl}(s) = \frac{a_0 + a_1s + a_2s^2}{b_0 + b_1s + b_2s^2 + b_3s^3 + b_4s^4} \quad (4.14)$$

and the closed loop compliance transfer function:

$$C_{cl,x}(s) = \frac{c_0 + c_1s + c_2s^2}{b_0 + b_1s + b_2s^2 + b_3s^3 + b_4s^4} \quad (4.15)$$

Both Equation (4.14) and Equation (4.15) are derived in Appendix A.

The static stiffness obtained with the proposed Lead-lag filter can be written as:

$$F_{clx}(0) = \frac{1}{C_{cl,x}(0)} = P \cdot K_i \cdot K_a \cdot K_{sens} \cdot M_i \quad (4.16)$$

The design strategy used here promises a wide range of closed loop characteristics. In practice, the characteristics of the closed loop system are restricted to variations in a certain range only. Section 4.7 will comment on these practical limitations.

4.5 Accuracy analysis of the Lorentz force

The accuracy of the propulsion force will be analyzed in this Section.

Equation (4.8) can be rewritten to:

$$\frac{\Delta F_l}{F_l} = \frac{\Delta N}{N} + \frac{\Delta \mu_0}{\mu_0} + \frac{\Delta \mu_{r,air}}{\mu_{r,air}} + \frac{\Delta I_{sec}}{I_{sec}} + \frac{\Delta N_{sec}}{N_{sec}} + \frac{\Delta l}{l} + \frac{\Delta \left\{ \frac{(I_0 - \delta I)}{(S_0 + \delta Z)} + \frac{(I_0 + \delta I)}{(S_0 - \delta Z)} \right\}}{\left\{ \frac{(I_0 - \delta I)}{(S_0 + \delta Z)} + \frac{(I_0 + \delta I)}{(S_0 - \delta Z)} \right\}} \quad (4.17)$$

Equation (4.17) indicates that the relative error of each component of the Lorentz force will contribute to the relative error of the Lorentz force itself. Therefore, each component will be analyzed. Analysis of N , μ_0 , $\mu_{r,air}$, I_0 and I_{sec} was done in Section 3.5. Three parts remain:

4.5.1 Length of current carrying conductor: l

The length l of the current carrying conductor is defined as the part of the coil that carries the current and is located inside the magnetic field. If the magnetic flux is confined to the air-gap (this can be done by keeping the recommendation of Section 3.5 in mind), then the length l equals the width of the magnetic pole.

If the magnetic field is not confined to the air-gap of the magnetic actuator, the stray flux may interact with the coil at positions outside the air-gap. An exact determination of this effect must be analyzed using a finite element analysis.

4.5.2 Number of secondary windings: N_{sec}

The number of secondary windings is unlikely to change during operation. The relative error can therefore be set to zero.

4.5.3 Primary currents and air-gaps: $\left\{ \frac{(I_0 - \delta I)}{(S_0 + \delta Z)} + \frac{(I_0 + \delta I)}{(S_0 - \delta Z)} \right\}$

$$\text{Analysis of } \left\{ \frac{(I_0 - \delta I)}{(S_0 + \delta Z)} + \frac{(I_0 + \delta I)}{(S_0 - \delta Z)} \right\}$$

shows a very interesting feature. When δZ equals zero, this equation reduces to:

$$2 \cdot \frac{I_0}{S_0}$$

Apparently, when the magnetic bearing reduces suspension errors to zero, the magnetic propulsion force will be constant, and not dependable on the control current δI . Unfortunately, the magnetic bearing will not function perfectly, and δZ will not be zero and a small effect remains.

Measurements on an SPU set-up have shown that δZ will vary about $2 \mu\text{m}$ at maximum (with a nominal air-gap S_0 of 1 mm) during normal operation, and that δI will vary up to one percent of I_0 . Assuming these variations as errors, the equation in brackets reduces to:

$$\left\{ \frac{(I_0 - 0.01 \cdot I_0)}{(S_0 + 0.002 \cdot S_0)} + \frac{(I_0 + 0.01 \cdot I_0)}{(S_0 - 0.002 \cdot S_0)} \right\} = 2.000048 \cdot \frac{I_0}{S_0}$$

Thus, the relative error during normal operation equals 24 ppm.

The air gap S_0 is also subject to close inspection. The influence of position deviations is not very critical, as shown above, but the influence of S_0 is of the first order. The air-gap S_0 has also been discussed in Section 3.5.5.

4.6 Mutual interaction between suspension and propulsion

An important issue is the interaction between Suspension and Propulsion. It is important that a stable and stiff magnetic bearing keeps its functionality if secondary coils are placed inside the air-gap and fed with a current. It is inevitable that the design approach of the SPU leads to interaction between the suspension and propulsion forces. The interaction can be described from two points of view. Both points of view will be discussed below.

4.6.1 The influence of the propulsion on the suspension

Figure 4.4 shows two finite element computations of the layout of the magnetic field. Figure 4.4.a shows the magnetic field plus the magnetic forces when no current flows through the secondary coils. Note the symmetry of the magnetic field.

Figure 4.4.b shows the magnetic field plus the magnetic forces when a relatively small current is sent through the secondary coils. Now the force changes a little bit. Note that the suspension force stays the same, while the propulsion force is generated. This indicates that the propulsion will not influence the suspension.

Things will change when too much current is sent through the coils. In this case the material of the rotor might saturate. The suspension forces can not increase any further and the magnetic bearing will become unstable. This is of course not permitted.

$F=63.5 \text{ N}$

$F=62.1 \text{ N}$

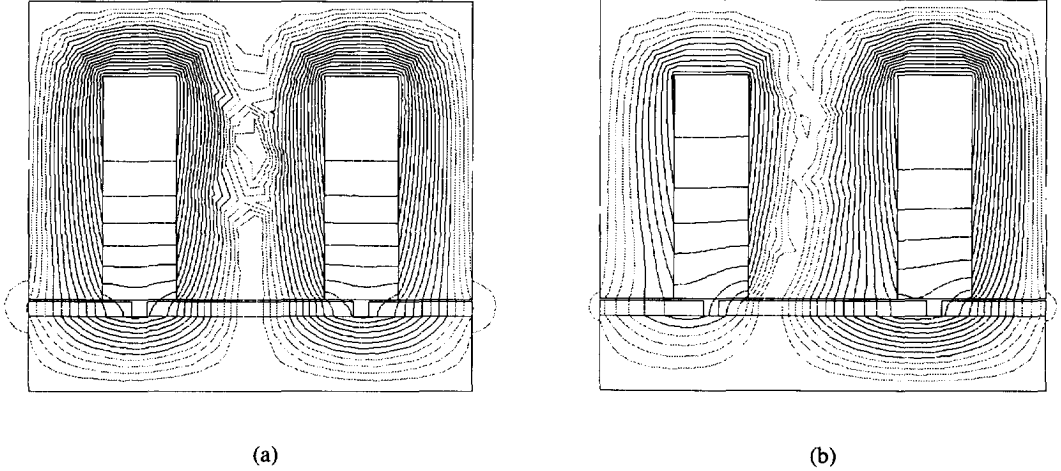


Fig. 4.4 Two Finite Element Analyses of the SPU. (a) shows the flux distribution when the secondary current I_{sec} equals zero. Note the symmetry of the distribution. The reluctance force (normal force) is indicated. (b) shows the flux distribution when the secondary coils carry a small current. The flux distribution is no longer symmetric, but the suspension force stays the same.

4.6.2 The influence of the suspension on the propulsion

The influence of the suspension on the propulsion can be analyzed using Equation (4.8). When the parameters outside the brackets are replaced by a constant k , Equation (4.8) can be written as:

$$F_L = k \cdot \left\{ \frac{(I_0 - \delta I)}{(S_0 + \delta Z)} + \frac{(I_0 + \delta I)}{(S_0 - \delta Z)} \right\} \quad (4.18)$$

Quite clearly, two parameters in Equation (4.18) are of importance in the amount of interaction. These two parameters are δI and δZ . If the magnetic

bearing functions perfectly, then $\delta Z = 0$, and the influence of δI will be canceled out completely. If this is not the case however, and δZ changes slightly, then changes in δI will be of influence. The theoretical analysis of this effect can be found in Section 4.5.

An experimental set-up was built in order to measure the propulsion force and to analyze whether the suspension would be influenced by the propulsion. This experimental set-up will be discussed in Chapter 6, as will be the test results.

4.7 Practical limitations to the propulsion force of the SPU

Several practical matters limit the performance of the SPU. These matters will be discussed here.

The first limitation considered here concerns the number and the layout of the secondary windings. There exists a strong correlation between the number of windings, the diameter of the copper and the air-gap of the magnetic bearing. When choosing the diameter of the copper winding and the number of secondary windings, the following design considerations should be taken into account:

- The maximum voltage supplied by the amplifier should fit the ohmic and inductive resistance of the coil.
- The maximum current supplied by the amplifier will limit the maximum force generated.
- The air-gap should be kept within reasonable size. Too wide an air-gap will result in flux loss, an inefficient magnetic circuit and an oversized effort to control the suspension forces (see Section 3.5).

When Equation (3.43) is reconsidered here, a consideration comparable to the one in Chapter 3 can be made. The contribution of $I \cdot R$ should be compared to the contribution for $L \cdot dI/dt$.

When the propulsion force is compared to the suspension force, the following relationship is derived:

$$\frac{F_L}{F_R} = \frac{8 \cdot N_{sec} \cdot I_{sec} \cdot x}{N \cdot I_0 \cdot b} \quad (4.19)$$

where

b = the width of magnetic pole.

Taking into account that I_{sec} and I_0 will be of the same magnitude and assuming that $x < 0.1 \cdot b$, the following conclusion can be drawn:

$$\frac{F_L}{F_R} < 0,8 \cdot \frac{N_{sec}}{N} \quad (4.20)$$

The area reserved for primary windings in a conventional E-I magnetic circuit equals:

$$Q = b \cdot d \cdot 3b = 3 \cdot b^2 \cdot d \quad (4.21)$$

where

d = the depth of the magnetic pole.

This is shown in Figure 4.5.

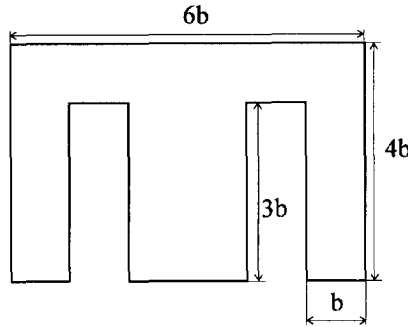


Fig. 4.5 The area reserved for primary windings around the center magnetic pole is created by the rectangular parts that are removed from the lamination. This magnetic circuit design is very common.

The area reserved for the secondary windings equals:

$$Q_{sec} = b \cdot d \cdot S_0 - 0.1 \cdot b^2 \cdot d \quad (4.22)$$

The assumption that half the area reserved for primary windings is filled with windings carrying I_0 (differentially wound coils), and that all the area reserved for secondary windings is filled, leads to:

$$\frac{F_L}{F_R} < 0,8 \cdot \frac{0.1 \cdot b^2 \cdot d}{1.5 \cdot b^2 \cdot d} = 0.053 \quad (4.23)$$

or

$$F_L < 0.053 \cdot F_R \quad (4.24)$$

This feature can be found in most literature on linear motors, where the authors mention the unfortunate fact that the “parasitic” force in suspension direction is always much larger than the desired propulsion force. Some designs exist where the attraction force is reduced to three times the propulsion force in single-sided motors. This is achieved by reducing the amount of iron on the moving part and thus reducing the magnetic attraction forces. This can of course not be done within the SPU.

Looking at the magnitude of the propulsion force, there seems to be no real limit. [38] reports about linear motors capable of generating 9 kN propulsion force, in the presence of the extremely high parasitic suspension forces.

The distribution of the secondary coils, together with the direction of the current flowing through them, is shown in Figure 4.6. The maximum stroke of the rotor is limited to the distance between the magnetic poles of the stator, d_m . Other coil layouts, commuting the current through various parts of the coils, or another magnetic circuit configuration allow for enlargement of the stroke of the rotor to twice the distance between the magnetic poles (without commutation) or even more with commutation of the current. This, however, was not part of this research.

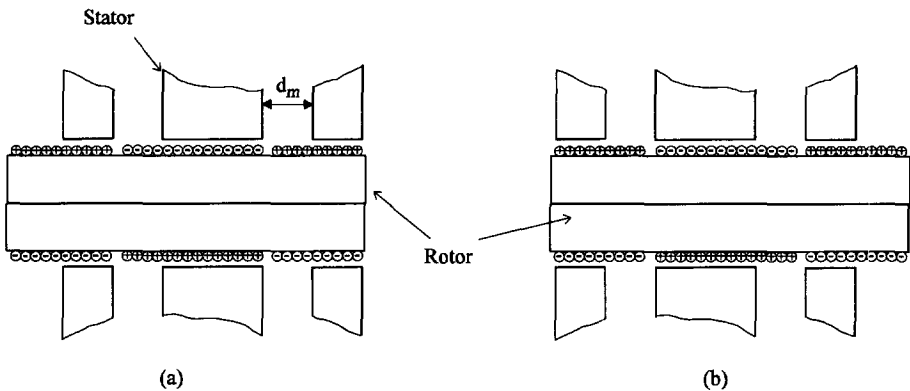


Fig. 4.6 The maximum stroke of the rotor is limited to d_m , the distance between the magnetic poles. Other coil configurations, commuting the current through various parts of the coil or another magnetic circuit allow for enlargement of the stroke.

The secondary coils carry a current and this current must be provided to the rotor by means of a flexible wire. This wire will introduce some parasitic forces to the rotor, which is unfortunate but can not be prevented. The flexile supply wires will also prevent the rotor from having an infinte stroke.

5 SPU components

5.1 Introduction

Figure 5.1 shows a simple magnetic bearing consisting of the following components:

- a magnetic circuit or actuator,
- a position sensor,
- a controller, and
- a power amplifier.

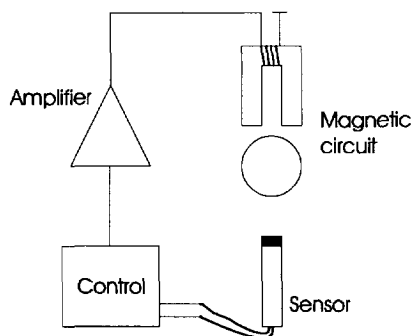


Fig. 5.1 A simple magnetic bearing needs a sensor, a controller, an amplifier and a magnetic circuit.

The components of the linear motor, described in the previous Chapter are the same as the components for the magnetic bearings.

5.2 Position sensors

Both the unstable nature of the magnetic bearing, which has been described in Chapter 3, and the marginally stable propulsion system, described in Chapter 4, need a position sensor to measure the actual position in order to realize a feedback loop. This sensor measures the position of the suspended object relative to the stator, or relative to another, arbitrarily chosen point. This way, information about the state of the rotor (here position and orientation information) can be obtained and used in the control feedback loop.

The position sensing method that is used is not allowed to physically contact the rotor. Physical contact would destroy the contact-free operation principle of the whole system.

There are several proximity sensing methods that are potentially applicable to magnetic bearing systems. The following sensors will be described in this Section:

- inductive sensors,
- eddy current sensors,
- capacitive sensors, and
- optical sensors.

Sensors using form standards will be treated in Section 5.3.

For certain applications, it may be possible to use the magnetic circuit itself as a position sensor. This feature, commonly called "Senseless Bearing" will be treated in Section 5.4.

The position sensors must have the following characteristics if they are to be used in combination with the Suspension and Propulsion Unit:

- a contact free operation,
- a range varying from a few millimeters for magnetic suspension up to several tens of millimeters for magnetic propulsion,
- an accuracy defined by the system requirements. For sub-micrometer applications, the sensor accuracy should of course also be sub-micrometer,
- the bandwidth of the sensors must be high enough to allow for a good controller bandwidth. Rule of thumb is a ten times higher bandwidth of the sensor compared to that of the controller.

5.2.1 Inductive sensors

The principle of operation of an inductive sensor involves a sensing coil on a stator having an inductance that is influenced by the distance between the stator and the ferromagnetic material on the rotor. Assuming that

- the relative permeability of the rotor is much higher than the relative permeability of air, and
- the distance between the rotor and the stator is not too large,

then the inductance of the sense coil can be found with:

$$L_s = \frac{A \cdot \mu_0 \cdot \mu_{r,air} \cdot N^2}{x} \quad (5.1)$$

where

- L_s = the sense coil inductance,
- A = the cross-sectional area of the sensor,
- μ_0 = the permeability of vacuum,
- $\mu_{r,air}$ = the relative permeability of air,
- N = the number of windings on the sensor, and
- x = the measured air gap length.

Figure 5.2 shows a simplified drawing of the inductive sensor.

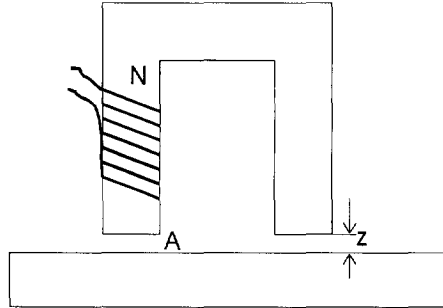


Fig. 5.2 Principle of operation of the inductive sensor. The air-gap, z , is determined by measuring the inductance of the coil that has N turns, being part of the magnetic circuit with cross-sectional area A .

Low permeability materials can be placed between the inductive sensor and the rotor. This way the rotor can be “canned” in a material, for example to keep the rotor in a vacuum, while the sensor is placed outside the vacuum. The canning material can be made of conductive material if the sensor electronics allow for this.

The accuracy of the measurement depends significantly upon:

- the quality of the sensor electronics,
- the influence of magnetic stray fields caused by the magnetic circuit, and
- the homogeneity of the target material.

Inductive sensors usually have quite a large amount of electronic noise, an accuracy as good as several μm , and a high bandwidth. They are very robust.

5.2.2 Eddy current sensors

The eddy current sensor is a variation of the inductive sensor. A coil is placed near a target material. The coil is part of a resonant circuit and has a resonant frequency somewhere between about 10 kHz and several hundreds of kHz. The coil is excited in its resonant frequency and placed in the proximity of the target material. The alternating magnetic field induces eddy currents in the target material, provided that this material is conductive.

The quality factor, Q , of the resonant circuit is influenced by the eddy currents induced in the target material. The factor Q , decreases with increasing eddy currents. Since eddy currents increase with decreasing distance to the target, a sensor is realized. The sensor electronics measures the quality factor and converts the information into a voltage, which is a linear measure for the distance.

The eddy current sense coils can be very small in comparison with the inductive sensors.

The target material must be electrically conductive to permit the generation of the eddy currents. The material does not need to be ferromagnetic.

A possible layout of this sort of sensor is shown in Figure 5.3. Three coils are arranged along a rod, made of laminated sheets of copper. The current, alternating at radio frequency, flows through the coil C1 and induces a signal in coils C2 and C3. The outer coils are connected counterclockwise. The voltage induced is:

$$U_2 = K_{c2} \cdot \frac{d\Phi_2}{dt} - K_{c3} \cdot \frac{d\Phi_3}{dt} \quad (5.2)$$

where

U_2 = the voltage induced in coil C2 and coil C3,

K_{c2} = a constant for coil C2,

K_{c3} = a constant for coil C3,

Φ_2 = the flux through coil C2, and

Φ_3 = the flux through coil C3.

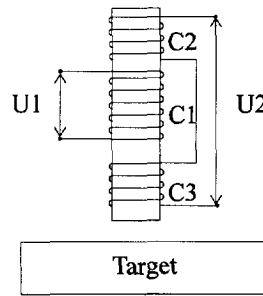


Fig. 5.3 Working principle of a three-coil eddy current sensor. The magnetic flux produced by coil C1 induces a voltage U_1 . Eddy currents produced in the target material influence the flux distribution and thus change the voltage U_2 .

When no target material is present, the flux through C2, Φ_2 , equals the flux through C3, Φ_3 , and no signal is produced. When a target material is present, eddy currents are induced in it. The flux through coil C2, is changed, resulting in a voltage U_2 , corresponding to Equation (5.2).

5.2.3 Capacitive sensors

The capacity between two electrodes is described by:

$$C = \frac{\epsilon \cdot A}{d} \quad (5.3)$$

where

- C = the capacitance between two electrodes,
- ϵ = the permittivity of the medium between the two electrodes,
- A = the overlapping area of the two electrodes, and
- d = the distance between the two electrodes.

Capacitive sensors can be used in two ways. The first principle uses the dependency of the capacitance on the distance d . By changing the distance d between the capacitor electrodes, the capacitance C changes proportional to $1/d$.

The second principle uses the dependency of the capacitance on the overlapping area A . By moving the capacitor electrodes parallel to each other, the area A changes. The capacitance C changes proportional to A . Both principles are shown in Figure 5.4.

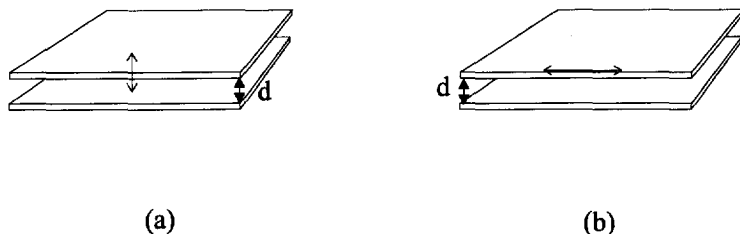


Fig. 5.4 Two measuring principles using capacitive sensors. a shows the principle based on changing the distance d , while the principle based on changing the overlapping area A is shown in b.

The first principle is suitable for measuring small distances with very high resolution. It is a typical implementation of the sensing principle for the magnetic bearing function of the SPU. If the rotor is not allowed to have an electrode placed on it, an alternative can be used. This is depicted in Figure 5.5. Two electrodes of the capacitive sensor are placed adjacent to each other, instead of opposite to each other. The proximity of a conducting rotor will influence the length of the electric flux lines and effectively the variable d in equation (5.3).

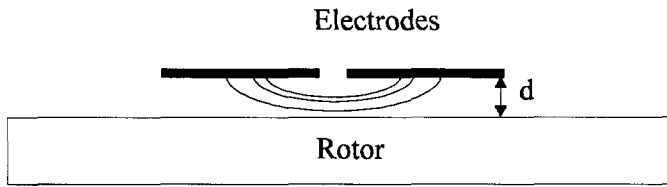


Fig. 5.5 Variation of the capacitance as a function of d without any electrodes placed on the rotor. The rotor material must possess a relative permittivity that differs from unity.

The second principle lends itself for measuring over a long range. Since the distance d can be kept small, the capacitance C will not become too small at long strokes. Using several electrodes in an array, a form standard or a multi axis sensor can be built. This will be treated in Section 5.2.5.

Moving an electrically grounded vane, placed between two stationary electrodes, will also result in a changing capacitance between the two electrodes. The vane blocks part of the electric field, thus effectively changing the overlapping area A . This is shown in Figure 5.6.

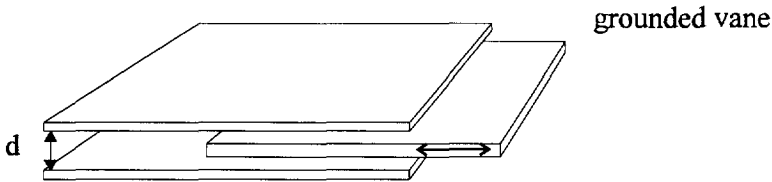


Fig. 5.6 Moving an electrically grounded vane between two fixed electrodes results in a variation of the capacitance. The electric field is blocked, thus effectively changing the overlapping area of the electrodes.

Main advantage of this configuration is its independency of variations in the vertical position of the grounded vane.

5.2.4 Optical sensors

Two types of optical sensors will be described here. One optical sensor type measures with a very small stroke only, and is usually used as a magnetic bearing sensor. The principle of operation is very simple.

A Light Emitting Diode (LED) is placed opposite to a Photo Diode (PD). The light beam is cut by the rotor. This is shown in Figure 5.7. The intensity of light that is detected by the PD is proportional to the position of the rotor.

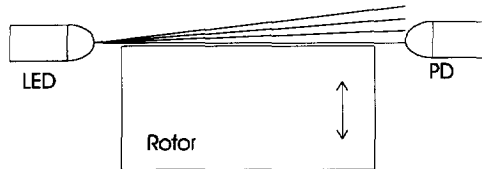


Fig. 5.7 A Light Emitting Diode (LED) emits light that is received by a Photo Diode (PD). The light beam is cut by the rotor, thus influencing the amount of light received by the PD. The intensity of the light received is a measure for the position of the rotor.

This principle does not depend on the material properties of the rotor. The only requirement is that the rotor material is not transparent.

The accuracy of this sensor type is very poor. Due to the fact that the intensity of the light is measured, every environmental condition that influences the light intensity, also influences the position signal. Any stray light received by the photo diode will be interpreted as a position deviation.

The second type of optical sensor that can be used is the laser interferometer. An interferometer is an optical measuring device that uses the interferential capability of light for measurement of a distance.

Interferometers split a beam of light in two or more beams, which have different optical paths, and combine them again to obtain an interference pattern. This interference pattern is defined by the differences of the optical path lengths. It is therefore possible to measure a distance variation with an interferometer.

For measurements of displacement of a rotor with a high precision (up to several nanometers) over a long range (up to several meters), there is essentially only one type of interferometer in use. This is the interferometer based on the Michelson interferometer, shown in Figure 5.8.

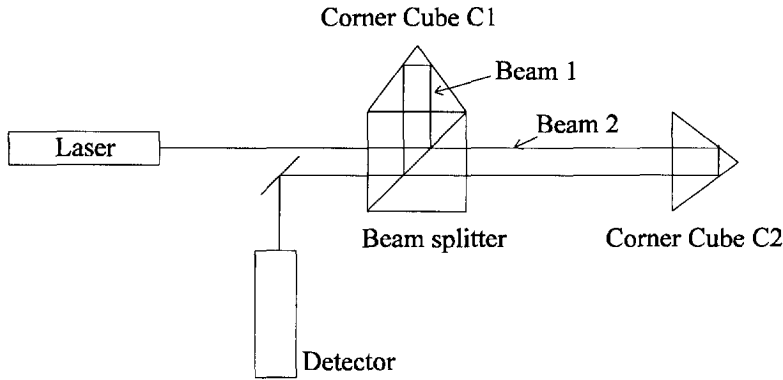


Fig. 5.8 Laser interferometer for distance measurement, based on the Michelson interferometer. A light beam is split by a beam splitter. The beams follow a different optical path. Variation in one optical path length is detected when the beams are recombined and form an interference pattern. The detector measures the displacement of the second corner cube by analyzing the interference pattern of the laser beam.

A laserbeam is divided into two separate, but coherent beams by a beam splitter. One beam is reflected towards a stationary corner cube or mirror, C1, and one beam is sent towards the moving object (corner cube C2). The beams follow different optical paths. The beams interfere in the beamsplitter and a detector analyzes the interference pattern.

When corner cube C2 moves, the interference pattern will change. Analyzing this pattern results in a distance measurement with $\lambda/2$ resolution. λ is the wavelength of the laser light (typically 632 nm). Using interpolation techniques [14], the resolution can be increased a hundred to a thousand times.

Interferometers are commercially available. They are accurate, have high bandwidth (several kHz), and are very expensive.

5.3 Form standards

A sensor based on form standards usually consists of two parts:

- a grid, grating or matrix structure placed on a stiff and stable underground, and
- a movable sensor measuring the position relative to the matrix.

The accuracy of the sensing method is highly dependable on the quality and accuracy of the grating. This grating is called the form standard. Two measuring systems using form standards will be discussed here: the capacitive form standard, [15], and the optical form standard, [28].

Capacitive form standard

The electrode structures in the transducer consist of a sensor head with nine (3x3) electrodes and a chessboard-like (10x14) reference electrode matrix, the form standard (Figure 5.9a). The electrodes of the matrix can be selected in such a way that columns and rows of electrodes are formed which can then be used respectively to determine the X- and Y position of the sensor head in a local coordinate system. Each sensor electrode combined with two columns or rows of the matrix electrode forms a simple differential (linear) position transducer (Figure 5.9b).

The electronic circuitry in this case consists of a solid-state electronic AC bridge, two multiplexers, a lock in amplifier and a microcomputer for signal processing. The accuracy obtained with this sensor is very high, 500 nm x 500 nm, over a long range, 85 mm x 69 mm, but state of the art is a very low bandwidth: 10 Hz [15].

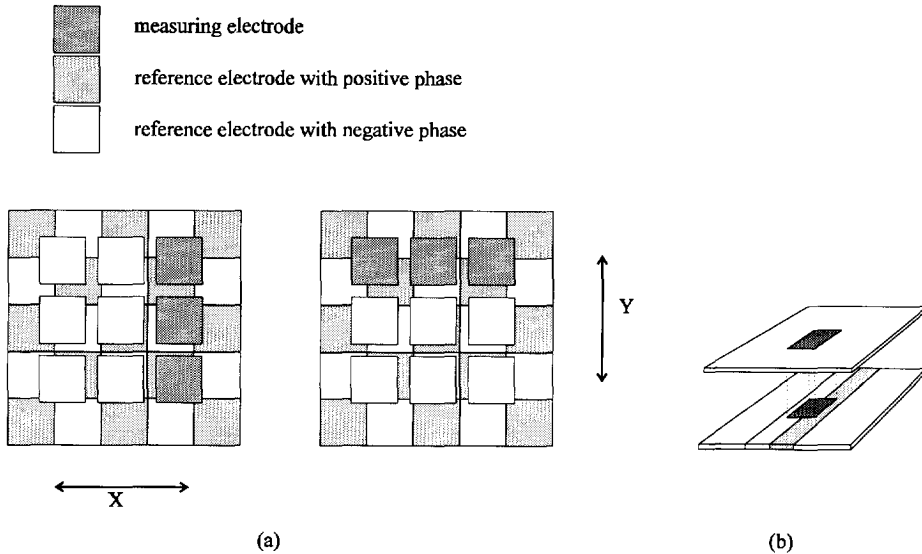


Fig. 5.9 Principle of the 2D position transducer. Nine sensor electrodes are shown above a part of the reference electrode matrix. Measurement in X-direction and Y-direction is possible by selecting columns and rows, respectively. (b) shows the principle of the differential plate capacitor, the measurement principle used by the rows and the columns.

Optical form standard

The optical form standard mentioned here is the PP109R from Heidenhain. The PP109R incremental, two coordinate measuring system has been developed for measuring and positioning tasks typical for the semi-conductor industry. This system can determine the position of an object with measuring steps of 10 nm in two perpendicular directions.

The PP109R consists of one grid plane and two scanning heads. Nearly square elevations, approximately 0.2 μm high and arranged at regular distances on the grid plane, serve as measuring standard. The squares are applied to a glass substrate at an angle of 45 degrees relative to the measuring direction. The edge length of one square is 2.83 μm . Scanning is without contact and is based on the interferential measuring principle. Each scanning head provides two 90 degrees phased shifted sinusoidal output signals with a signal period of 4 μm and one

reference mark signal. Interpolation electronics provide an interpolation of 800 times, thus creating a resolution of 5 nm. Figure 5.10 shows the basic layout.

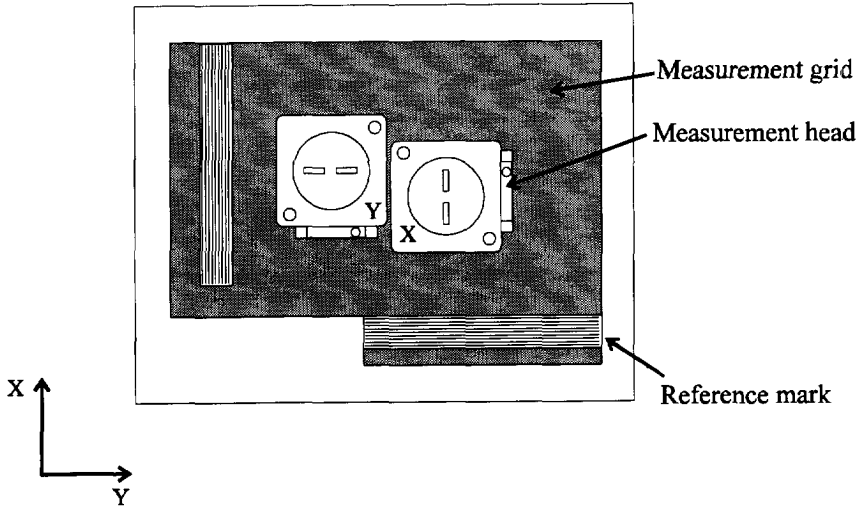


Fig. 5.10 Basic layout of the Heidenhain PP109R incremental encoder. Two sensor heads measure a displacement in the X- and the Y direction, respectively, using an interferential measuring principle [28].

A description of the exact working principal of the interferential measurement used can be found in [28].

5.4 Sensor-less magnetic bearing

It is possible to build a magnetic bearing that has no specific component that can be identified as a position sensor. Instead, the state of the magnetic circuit is used to determine the air-gap.

As has been calculated in Section 3.6, Equation (3.45), the self-inductance of the primary coil providing the magnetic field for the magnetic bearing is:

$$L = \frac{\mu_0 \cdot N^2 \cdot A}{\frac{2 \cdot x}{\mu_{r,air}} + \frac{l_{iron}}{\mu_{r,iron}}} \quad (3.44)$$

Equation (3.45) shows that the inductance L depends on the distance x .

The inductance L can be measured by observing how the current I in the coil changes in response to a voltage step:

$$L = \frac{V}{\left(\frac{di}{dt}\right)} \quad (5.4)$$

Neglecting the influence of the iron, Equation (3.44) can be rewritten into:

$$x = \frac{\mu_0 \cdot \mu_{r,air} \cdot N^2 \cdot A}{2L} \quad (5.5)$$

and the air-gap x can be calculated. Visscher [68] has shown that magnetic bearings can be built using this strategy. These bearings are commonly called "Senseless bearings", or "Sensor-less bearings".

Accurate inductive sensing of the rotor position through the senseless bearing is subject to the same constraints as stated for the inductive sensor. Several non-linear effects, especially if the magnetic circuit is operated over a long stroke, influence the accuracy and the stability of the magnetic suspension.

The senseless bearings are restricted to low current and low stiffness applications, according to Visscher [68].

5.5 Overview of sensors

This Section gives a brief overview of the various sensors discussed in the previous Sections. The overview, given in table 5.1, includes the price categories for several commercially available sensor types.

Sensor name	sensor type	acc. (μm)	range (mm)	bandwidth	target	sens. (V/m)	price
Micro-Epsilon Multi-NCDT 300	ind.	1	0.5	100 kHz	cond.	20,000	medium
Micro-Epsilon Digi-NCDT 1000	ind.	1	0.5	100 kHz	cond.	20,000	medium
Kaman KD-4000	eddy	0.1	0.5	?	cond.	4,000	medium
EPRO PR6422	eddy	1	1	20 kHz	CrMo4	16,000	low
EPRO PR6423	eddy	1	2	20 kHz	CrMo4	16,000	low
Focale Nanotech CST-50	cap.	0.5	1	100 Hz		?	medium
Micro-Epsilon Capa NCDT 600	cap.	0.002	0.05	6 kHz		200,000	high
Micro Eng. small stroke	cap.	0.002	0.025	5 kHz		?	medium
Micro Eng. long stroke	cap.	4	10	5 kHz		1,000	medium
LED/PD	opt.	high	0	100 kHz	non transp.		low
laser int.	opt.	0.001	100	100 kHz	mirror		very high
form standard	cap.	0.5	50 x 50	10 Hz			medium
Heidenhain	opt.	0.05	42 x 42	speed limit			medium

Table 5.1 Overview of the various sensors for the SPU. A few commercially available types are shown.

A few considerations arise with regard to the choice of the position sensor:

- Eddy current transducers use conductive targets that need not to be ferromagnetic. This may be useful in applications where the body of the SPU is made of aluminum (for weight reduction reasons).
- Inductive sensors need ferromagnetic targets, but can work through conductive canning materials. Canning of the rotor is useful when the rotor is placed inside an isolated environment (such as vacuum) while the stator is not. The isolation of the environment is achieved with the canning material.
- Capacitive sensing can be very sensitive to small gap width changes, but are very delicate. For very high resolution, the capacitive sensors can easily be used, but only with small air-gaps. The ratio between resolution and air-gap should not extend 10^{-5} , see [15]. The capacitive sensors are very sensitive to electrical noise generated by sources outside the set-up.
- For certain dedicated applications, operation without separate sensors may be feasible. The applications are restricted to set-ups with low stiffness and low bandwidth (typically a stiffness below 10^4 N/m and bandwidths below 50 Hz).
- Care should be taken with the absolute position accuracy of the sensor, for this is not the same as the resolution, and could be many orders of magnitude worse.

5.6 Power amplifiers

The adjustment of the magnetic forces in the SPU is achieved through controlling the current through in the coil. Since the control signal derived from the digital controller is a voltage signal, a Voltage Controlled Current Source (VCCS), or amplifier, is needed. Figure 5.11 shows a schematic view of the power amplifier in the magnetic bearing environment.

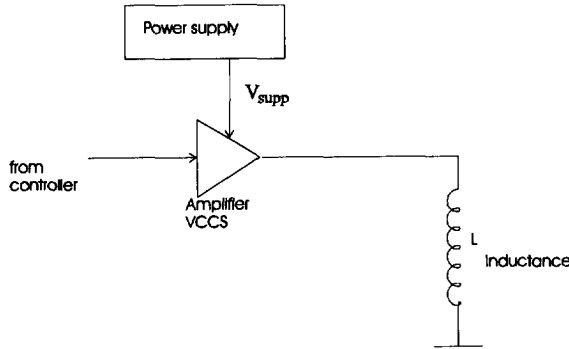


Fig. 5.11 The current control of the SPU needs a power amplifier and a power supply. The control signal is converted by the power amplifier into a current that is sent through the coil with inductance L .

The coil in the electromagnetic actuator appears electrically as an inductor. When a voltage V is applied across an inductor with inductance L , a current I is built up through the inductor. The relationship between the current and the applied voltage is given by:

$$I = \frac{1}{L} \cdot \int V \cdot dt + I_0 \quad (5.6)$$

Two important characteristics appear from this relationship:

- the rate at which the current in the inductor can change is limited by the voltage applied,
- the current in the inductor can not change instantly.

When an inductor is implemented as a coil, some resistance R will be included. The response of the current to a step-wise applied voltage V can be calculated with:

$$I(t) = \frac{V}{R} \cdot \left(1 - e^{-\frac{R}{L}t} \right) + I(0) \cdot e^{-\frac{R}{L}t} \quad (5.7)$$

where

- R = the resistance of the coil,
 t = time.

The time-constant of the electrical circuit, τ_e , is:

$$\tau_e = \frac{L}{R} \quad (5.8)$$

The time constant implies that 95% of the required current will be achieved at time $t = 3\tau_e$. This means that the magnetic actuator is limited in bandwidth by this factor τ_e . If higher bandwidths are to be achieved, the VCCS must actively measure the current through the coil and correct for the low bandwidth of the coil. This can be achieved by applying maximum voltage to the coil in order to achieve the desired current as soon as possible. This feature is of course the main objective of an amplifier.

An amplifier converts information received from the controller into a current through the coil. This current through the coil is measured, and compared with the required value. The error measured will be reduced with a feedback loop and possibly a PID controller. The maximum voltage, supplied to the amplifier by a power supply, will result in a maximum rate of change of the current, and therefore directly influences the bandwidth of the system.

The maximum rate of change of the amplifier, also called the slew rate, is given by:

$$\left(\frac{dI}{dt}\right)_{max} = \frac{V_{sup p}}{L} \quad (5.9)$$

where

$\left(\frac{dI}{dt}\right)_{max}$ = the maximum slew rate, and

$V_{sup p}$ = the maximum supply voltage.

The maximum current provided by the amplifier is given by:

$$I_{max} = \frac{V_{sup p}}{R} \quad (5.10)$$

The maximum current is usually smaller than equation (5.10) suggests. This is caused by limitations of the power electronics used in the amplifier.

Amplifiers can be divided into two categories: linear amplifiers and switching amplifiers. Both types will be discussed below.

5.6.1 Linear amplifiers

A linear amplifier is often mentioned as the most simple approach for control of the coil current. Figure 5.12 shows the basic diagram of its working principle.

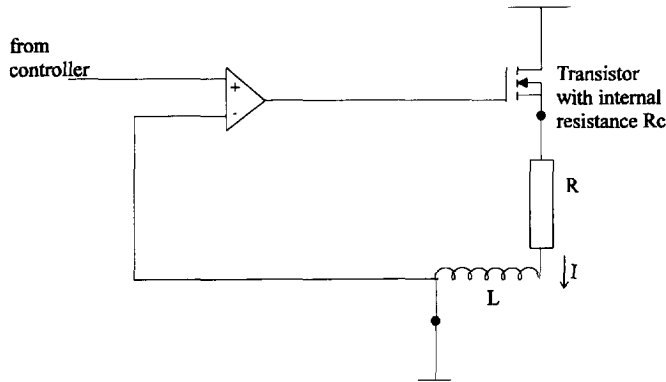


Fig. 5.12 Simplified representation of a linear amplifier in combination with a resistor and an inductor (represented by L and R). The current through the coil is regulated by controlling the variable resistance R_c in the amplifier.

The basic topology of a linear amplifier uses an active device to provide a controlled variable resistance in series between the fixed voltage of the power supply and the actuator coil. The variable resistance of the amplifier is controlled by measuring the actual current flow and tuning it to its desired value by changing the resistance R_c .

The current, I , supplied in combination with the variable resistance R_c results in a considerable amount of power dissipation in the amplifier. This means that the linear power amplifier becomes inefficient. The efficiency E_{lin} of the amplifier can be calculated with:

$$E_{lin} = \frac{I^2 R}{I^2 R + I^2 R_c} = \frac{I \cdot R}{V_{sup p}} \quad (5.11)$$

Equation (5.9) shows that the efficiency is very poor at low currents (most power is dissipated in the amplifier). The efficiency can be improved by lowering the power supply voltage, but this would also reduce the maximum slew rate of the current and the maximum current through the coil.

An advantage of linear power amplifiers is the very smooth and noise-free flow of the current through the coil. This is a prerequisite for high accuracy performance.

5.6.2 Switching power amplifiers

The basic topology for an alternative to the linear amplifier, i.e. the switching amplifier, is shown in Figure 5.13.

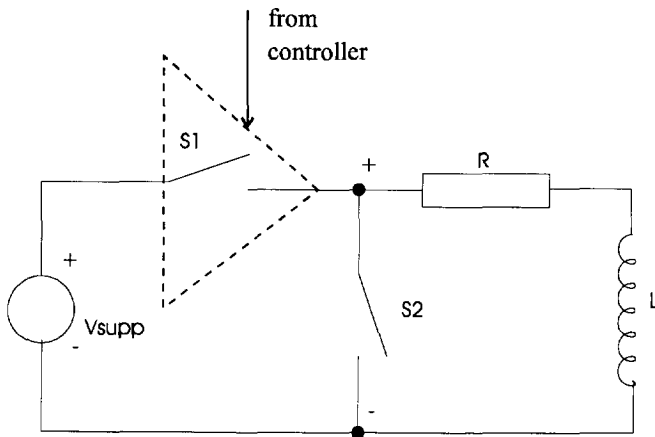


Fig. 5.13 Simplified representation of a switching amplifier in combination with a coil (L and R). The current through the coil is controlled by switching $S1$ and $S2$ alternately. When $S1$ is closed, $S2$ is open and vice versa.

The power amplifier includes two devices that act as actively controlled switches, $S1$ and $S2$. The switches are synchronized in such a way that always a switch is closed when the other is open. The switches are periodically alternated to force the current to flow through the coil.

The fact that a current flowing in a conductor that has inductance, L , does not immediately change with a voltage drop (see Equation (5.6)) is used in switching amplifiers. The switching sequence, or strategy, used in switching amplifiers, results in an average current flowing through the coil.

The switching amplifiers are very efficient. The fact that the current flows either through switch $S1$ (coming from the voltage supply) or flows through switch $S2$ (magnetomotive feedback, coming from the coil), combined with the

fact that the switches show very low resistance, results in little power dissipation in the amplifier.

The switching amplifier can take advantage of high power supply voltage to achieve rapid changes in current. The amplifier can also maintain an arbitrary current within the operating range. This arbitrary current, however, shows a current ripple. This ripple is caused by the switching of the amplifier.

The current ripple can be reduced by:

- reducing the supply voltage, or by
- increasing the switching frequency.

Reduction of the supply voltage reduces the maximum slew rate of the current and is therefore undesirable. The increase of the switching frequency is more promising, but can not be arbitrarily high: Real switches require a finite transition time between on and off. Increase of the switching frequency also reduces the efficiency of the amplifier. Still the efficiency is much higher than with linear amplifiers.

The current ripple produced by switching amplifiers is, taken from [23]:

$$I_r = \frac{0.5 \cdot V_{sup}}{f \cdot L} \quad (5.12)$$

where

- I_r = the current ripple,
- f = the switching frequency, and
- L = the inductance in mH.

[23] advises a maximum of 10% of the rated current as current ripple. This is totally unacceptable for high precision applications.

A compromise must be found, both for linear and switching amplifiers, with regard to the supply voltage. A high supply voltage will result in a high slew rate, but also in a low efficiency for linear amplifiers and a high switching noise in switching amplifiers.

5.7 Digital control

The modern trend in magnetic bearing design (discussed in Section 2.2) shows that analog control is abandoned in favor of the more flexible digital control. This can be understood especially in the case where:

- many different control parameters are tested on a magnetic bearing,
- different control strategies (modern and classic) need to be investigated and implemented, or
- additional features (safety features, information flows) are added to the product.

The work presented in this thesis was done on magnetic bearings and linear motors controlled with a digital controller. The controller, provided by dSpace GmbH, is based on a Digital Signal Processor (DSP), the TMS320C40 from Texas Instruments.

The control algorithms are written in the analog time domain or frequency domain with Matlab and Simulink. Simulink is a graphical simulation environment with strong links to Matlab, a mathematical tool for computing matrices. A typical strategy is shown below:

- calculate the controller parameters with Matlab,
- verify closed loop characteristics by simulation in Matlab,
- transfer controller to Simulink,
- add extra features (like input signal, reference signal, safety options, etc.) in Simulink,
- implement controller.

dSpace GmbH has provided their digital control environment with software that allows easy implementation of controllers designed with Simulink. A Simulink block diagram can be assembled from any standard Simulink blocks, optionally enhanced by user specific C language S-functions. The Mathworks' Real Time Workshop generates C-code for a selected part of a controller or simulation model. The dSpace Real Time Interface (RTI) handles the automatic download to the DSP system and starts the real-time test immediately. The software components for programming with Simulink are shown in Figure 5.14.

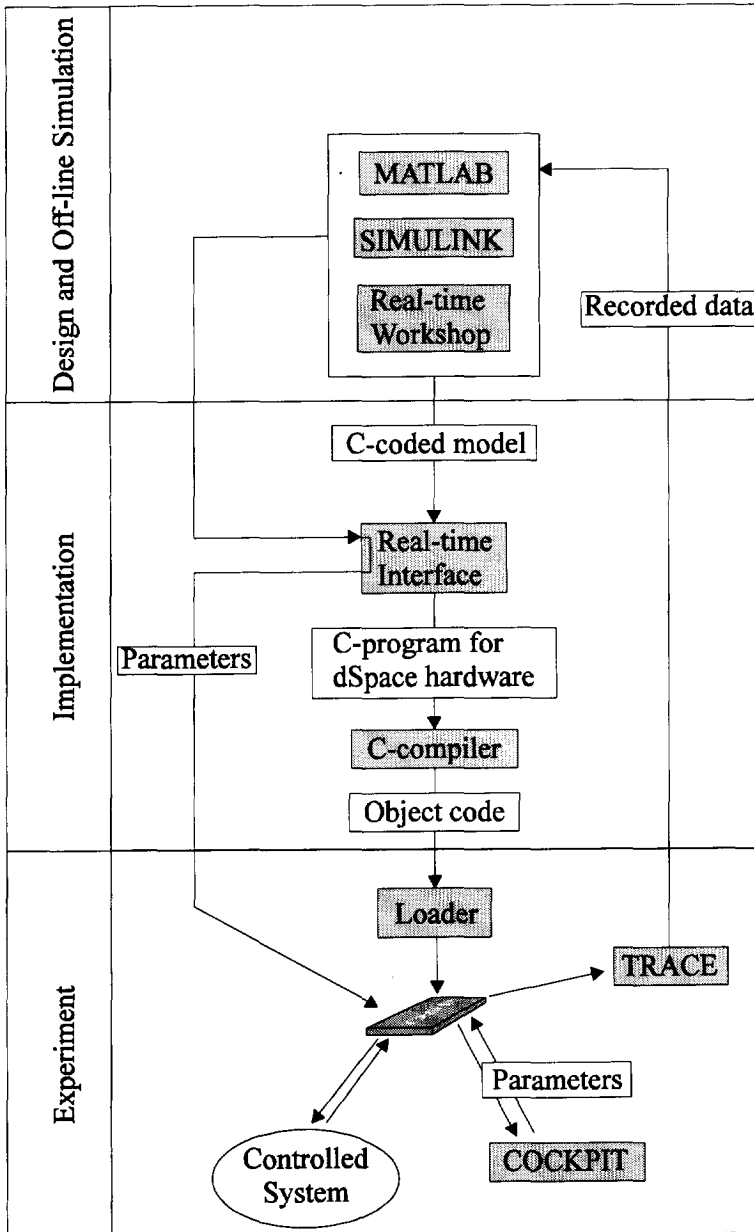


Fig. 5.14 Software components for a digital controller implementation.

After downloading a controller to the DSP processor, the experiment needs to be controlled and monitored. The software stores all the controller variables in the Dual Port Memory, supplied on the DSP hardware. Two tools are provided to monitor and to adjust parameters stored in Dual Port Memory. These tools are:

- Trace: for real-time signal monitoring and data acquisition, and
- Cockpit: graphical instrument panel for adjusting system parameters.

Cockpit and Trace give control over the experiment, without disturbing the closed-loop operation. Trace records and displays time histories of any variables in the DSP program. This data can be loaded into Matlab or other tools for detailed analysis.

Using Cockpit, individual graphical interfaces can be built for each application, without a single line of programming. Display instruments such as gauges and numeric displays are updated continuously, showing the current state of the system. Input instruments like sliders or numeric inputs allow parameters to be changed in the DSP during run-time.

Figure 5.15 shows the modular set-up of the dSpace system. The processor board, containing the DSP processor and the memory, is programmed via the host computer bus system. The DSP processor board works fully autonomous once it is programmed. Control of the program (start, stop and reset) and monitoring of the Dual Port Memory is done via the host computer bus by software running on the host computer.

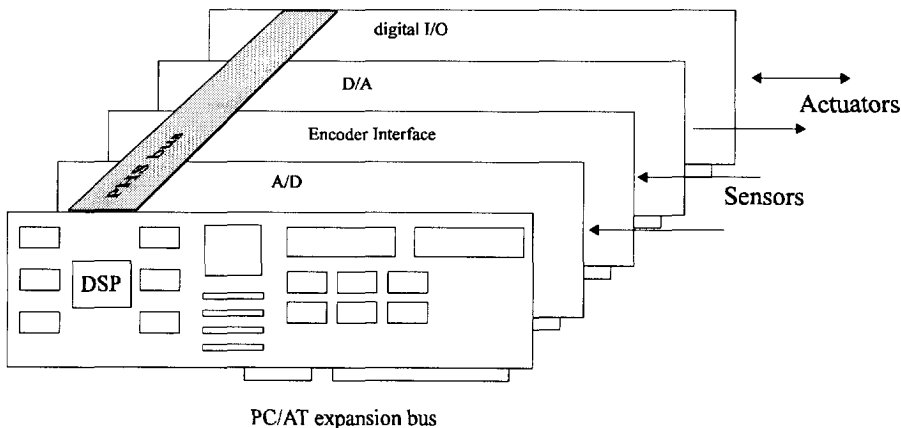


Fig. 5.15 Modular set-up of the dSpace system with the DSP mother board in the front and several AD and DA converters in the back.

Information about the state of the magnetic bearing and the magnetic propulsion is obtained via additional computer boards. These boards can be AD-converters, for analog inputs, and encoder interfaces, for incremental encoder readouts. The information obtained with these computer boards is sent to the DSP processor board via the PHS-bus (Peripheral High Speed bus).

After calculating the required controller outputs, the DSP processor sends the information to the DA converter or the digital I/O board. The digital signals are converted into analog outputs that control the experimental set-up.

The dSpace system currently in use at the Laboratory for Micro Engineering contains:

- one DS1003 processor board with a 50 Mflops TMS320C40 DSP processor from Texas Instruments, 60 KWords dual port memory.
- two DS2001 AD converters with 5 channels each, 16 bit, 5 μ sec conversion time, ± 10 V,
- one DS2102 DA converter with 6 channels, 16 bit, 2.5 μ sec conversion time, ± 10 V,
- one DS3001, incremental encoder board with 5 channels, 24 bit counters and 5 MHz maximum counting frequency.

Using this configuration, a six degrees of freedom, tame PID controller (in total: 12 states, 6 inputs and 6 outputs) can be implemented with a 10 kHz sampling frequency. All results in this thesis are obtained with this configuration.

6 Suspension and Propulsion Unit: the experimental set-up

6.1 Introduction

A first experimental set-up of the SPU was built at the Laboratory for Micro Engineering in 1992. The experimental setup was designed for two experiments. These experiments are:

- Proof that a horizontal propulsion force can be generated within predicted ranges, without destabilizing the magnetic bearing. This can be done by examining the interaction between suspension and propulsion.
- Measurement of the magnetic propulsion force.

This Chapter discusses the design of the experimental set-up, together with the results of the experiments performed with it.

6.2 Design of the experimental set-up

The sketch in Figure 6.1 shows the mechanical set-up with only the important parts drawn. Figure 6.2 shows a photograph of the experimental set-up.

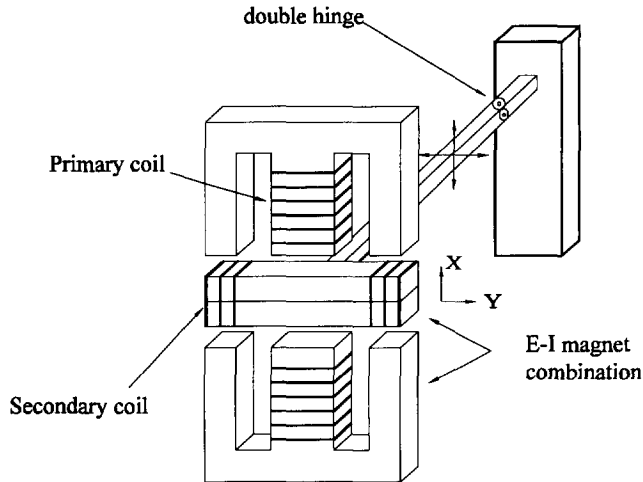


Fig. 6.1 Mechanical set-up of the SPU. Two E-core electromagnets exert forces on the rotor that carry the secondary coils. The support arm with the double hinge blocks four degrees of freedom, while the remaining two, X and Y, are controlled in the SPU. The center secondary coil, mentioned in Section 4.3, can not be applied in this set-up, and thus, is not shown.

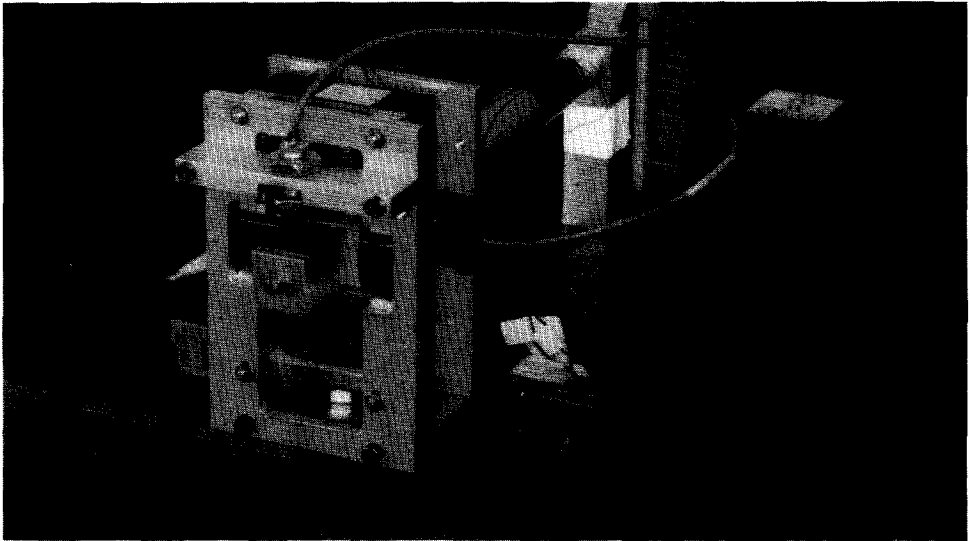


Fig. 6.2 Photograph of the experimental set-up of the SPU.

Clearly two E-cores can be distinguished in Figure 6.1. The E-cores are made of standard transformer sheets, and have the following dimensions:

- length: 60 mm,
- width: 20 mm, and
- height: 40 mm.

The center magnetic pole has a cross-sectional area of 20 mm x 20 mm, while the two outer magnetic poles have a cross-sectional area of 10 mm x 20 mm. The distance between inner and outer magnetic pole is 10 mm.

The area between the outer and center magnetic pole is reserved for the primary coils and has a cross-sectional area of 30 mm x 10 mm. This area is filled with a set of differentially wound coils with 120 turns each. The wire diameter is 0.4 mm.

The power amplifier used with this SPU element allows for a maximum output current of 1.2 A. The wire diameter was chosen according to the guidelines of Section 3.6.

The second E-core is placed opposite to the first. The space between the two E-cores is reserved for the rotor with the secondary coils.

Since the rotor has six degrees of freedom, and since only two of these can be controlled by the SPU, four degrees of freedom must be blocked. As a solution to this problem, the experimental set-up has a support arm of 180 mm length, connected to a double hinge, that on its turn, is connected to the real world. The double hinge effectively blocks four degrees of freedom (three translations and one rotation). The two remaining degrees of freedom (rotations) are controlled by the SPU. If the support arm is long enough, the rotations of the arm can be approximated as translations of the rotor within the SPU.

The secondary coils are placed on the rotor, but only at the outer magnetic poles. The fixation of the support arm to the rotor hinders the placement of a secondary coil at the center magnetic pole. This is unfortunate but plays no role in the experiments. Each coil consists of 75 windings of 0.3 mm diameter copper wire.

Only one sensor is used in this experimental setup. The sensor for controlling the suspension is placed at the front end of the SPU, just outside the rotor. The rotor is equipped with a small pad that the sensor uses as target. The sensor is not shown in the sketch, but can be distinguished in the photograph of Figure 6.2. The distance of the sensor to the double hinge (227.8 mm) is larger than the

distance of the magnetic circuit to the hinge (199.5 mm). The sensor is “non co-located”, meaning that the sensor does not measure the air-gap at the location of the magnetic circuit. This can have great impact on the controller design when modern controllers are used that can compensate for high frequency oscillations. The sensor used is an eddy current sensor, the EPRO PR6423, with 2 mm range and 1 μm accuracy.

The position of the SPU in horizontal (propulsion) direction is not measured and is not controlled.

The structure which fixes the sensor and the stator to the real world is not shown in Figure 6.1. The structure can be seen in the photograph of Figure 6.2. The structure is made of aluminum, and has a thickness of 5 mm. The support arm is also made of aluminum, and has a diameter of 20 mm. Experiments with a 5 mm diameter aluminum support arm showed that the 5 mm diameter has insufficient torsional stiffness. Sufficient torsional stiffness of the support arm is necessary to prevent any undesired oscillations around the axis of the arm.

6.3 Mathematical model

A simplified drawing of the experimental setup is shown in Figure 6.3. This simplified model is used for deriving the mathematical equations of the set-up. All mathematical parameters are shown.

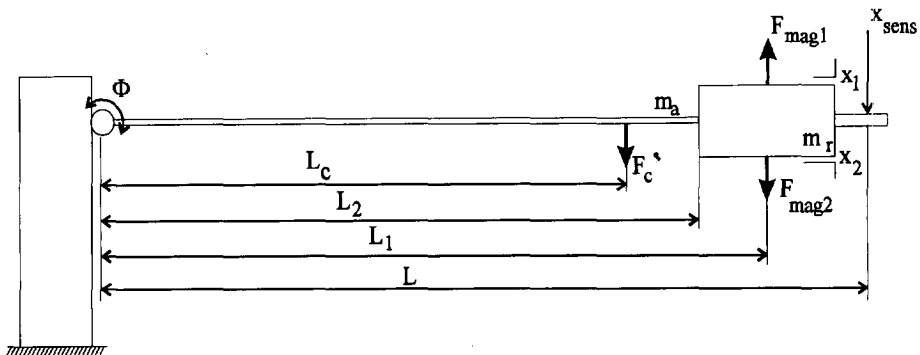


Fig. 6.3 Model of the SPU used for the mathematical derivation of the transfer function for the suspension.

The variables needed for the mathematical derivation of the transfer function for the suspension are shown in Figure 6.3. These variables are:

φ	= the rotation of the support arm,	[rad]
L	= the length of the support lever,	= 0.180 m
L_1	= the length of the sensor lever,	= 0.2278 m
L_2	= the length of the force lever,	= 0.1995 m
L_c	= the length of center of gravity lever,	[m]
m_a	= the mass of the lever,	= 0.143 kg
m_r	= the mass of the rotor,	= 0.246 kg
F_{mag1}	= the magnetic force in upward direction,	[N]
F_{mag2}	= the magnetic force in downward direction,	[N]
F_c	= the gravity force,	= 3.04 N
S_0	= the nominal air-gap,	= $0.85 \cdot 10^{-3}$ m
x_1	= the upper air-gap,	[m]
x_2	= the lower air-gap, and	[m]
x	= the measured position.	[m]

Equilibrium of moments around the flexible hinge gives:

$$\frac{1}{2}m_a \cdot L \cdot g + m_r \cdot L_2 \cdot g = F_c \cdot L_2 \quad (6.1)$$

This leads to the equivalent centroid Force F_c of:

$$F_c = \frac{\frac{1}{2}m_a \cdot L \cdot g + m_r \cdot L_2 \cdot g}{L_2} = 3.04 \text{ N} \quad (6.2)$$

Calculating the center of gravity with:

$$L_c \cdot g \cdot (m_a + m_r) = F_c \cdot L_2 \Rightarrow$$

$$L_c = \frac{F_c \cdot L_2}{g \cdot (m_a + m_r)} = 0.159 \text{ m} \quad (6.3)$$

results in a total parasitic moment M_c of:

$$M_c = F_c \cdot L_c = 0.48 \text{ Nm} \quad (6.4)$$

with

M_c = parasitic moment of the gravity force.

The dynamic equation of motion is written as:

$$J \cdot \ddot{\phi} = M_c - M_{mag} = M_c + L_2 (F_{mag1} - F_{mag2}) \quad (6.5)$$

with:

J = mass moment of inertia

M_{mag} = moment caused by the magnetic fields

Using the theory described in Chapter 3 and compensating for the non-co-location of the sensor leads to:

$$H_P = \frac{\frac{L_2 \cdot 4K_m \cdot I_0}{x_0^2}}{\frac{J}{L_1 \cdot K_{sens}} s^2 - \frac{L_2^2 \cdot 4K_m \cdot I_0^2}{L_1 \cdot x_0^3 \cdot K_{sens}}} = \frac{K_I}{M \cdot s^2 - K_C} \quad (6.6)$$

with

$$K_I = \frac{L_2 \cdot 4K_m \cdot I_0}{x_0^2} = 3.93 = \text{equivalent force/current index} \quad (6.7)$$

$$K_C = \frac{L_2^2 \cdot 4K_m \cdot I_0^2}{L_1 \cdot x_0^3 \cdot K_{sens}} = 0.786 = \text{equivalent negative stiffness} \quad (6.8)$$

$$M = \frac{J}{L_1 \cdot K_{sens}} = 1.94 \cdot 10^{-6} = \text{equivalent mass, and} \quad (6.9)$$

$$K_{sens} = 10303 \text{ V/m.}$$

The sensitivity of the EPRO6423 sensor was originally 16000 V/m. This sensitivity is changed in order to accomodate the sensor output voltage to the AD converter input range of +/- 10V. This attenuation is achieved by altering the gain of the anti-aliasing filter which is located prior to the AD converter. The resulting sensitivity, K_{sens} , is determined through calibration with an absolute sensor.

The closed-loop compliance transfer function is:

$$C_P = \frac{1}{\frac{J}{L_1 \cdot K_{sens}} s^2 - \frac{L_2^2 \cdot 4K_m \cdot I_0^2}{L_1 \cdot x_0^3 \cdot K_{sens}}} = \frac{1}{M \cdot s^2 - K_C} \quad (6.10)$$

6.4 Controller design

The controller is designed using the strategy from Section 3.4. The following specifications were set for the closed loop process for the suspension:

- bandwidth: 100 Hz,
- static stiffness: 10^6 N/m, and
- relative damping, β : 0.707.

These specifications were chosen in accordance with the theory on accuracy formulated in Chapter 1.

The cross-over frequency is found with Equation (3.24):

$$f_c = f_b \cdot \frac{(\sqrt{4\zeta^4 + 1} - 2\zeta^2)^{1/2}}{(1 - 2\zeta^2 + \sqrt{2 - 4\zeta^2(1 - \zeta^2)})^{1/2}} = 64.4 \text{ Hz}$$

The stability criterion of $\beta = 0.707$ leads to:

$$\alpha_m = \tan^{-1} \left(\frac{2\beta}{(\sqrt{4\beta^2 + 1} - 2\beta^2)^{1/2}} \right) = 65.5$$

and using (3.26)

$$M_d = \frac{1 + \sin \alpha_m}{1 - \sin \alpha_m} = 21$$

The time constant τ_d is calculated with Equation (3.27):

$$\tau_d = \frac{1}{2\pi f_c} \sqrt{M_d} = 0.0113 \text{ s}$$

Calculating the gain P of the controller is done by the computer program Matlab. This program yields:

$$P = 7.8137$$

The stiffness criterion is used to determine whether an integrating part should be added to the controller. Using Equation (3.35), M_i is calculated:

$$M_i = 24$$

The question remains where to start the integrating action. Allowing a maximum of 5 degrees phase-loss at the cross-over frequency, the value for K_{di} can be found from Appendix B:

$$K_{di} = 50$$

This will put the integration time constant at:

$$\tau_i = \tau_d \cdot K_{di} = 0.786s$$

A simulation of the system was performed with Matlab. The results of this simulation, together with measuring results, will be discussed in the next Section.

6.5 Simulation and measurement results

Experiments and measurements were performed on the experimental setup with regard to:

- closed loop performance,
- stiffness measurement, and
- accuracy analysis.

The closed loop performance is simulated with Matlab and measured with a HP dynamic signal analyzer. The results can be seen in Figure 6.4.

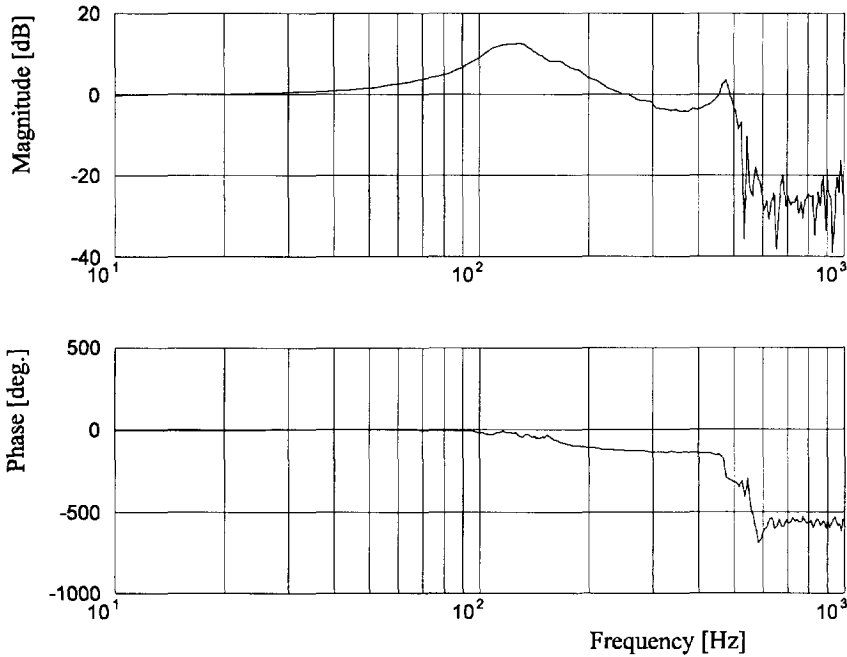


Fig. 6.4 Closed loop Bode diagram for the suspension function of the SPU.

From Figure 6.4 a very good behavior of the measured process can be concluded. The experimental set-up behaves the same as was predicted up to a frequency of 500 Hz. Here an additional eigenfrequency is found. This resonance is caused by an unmodelled high frequency oscillation. The source of this oscillation was not found.

The stiffness is measured by adding mass to the rotor. Figure 6.5 shows the effect of adding mass in the following order: 50 gram, 100 gram, 200 gram, and 300 gram. The displacement has been observed, corresponding to 0.4, 0.8, 1.7 and 2.5 μm respectively. This means that the setup has a static stiffness of approximately $1.13 \cdot 10^6 \text{ N/m}$.

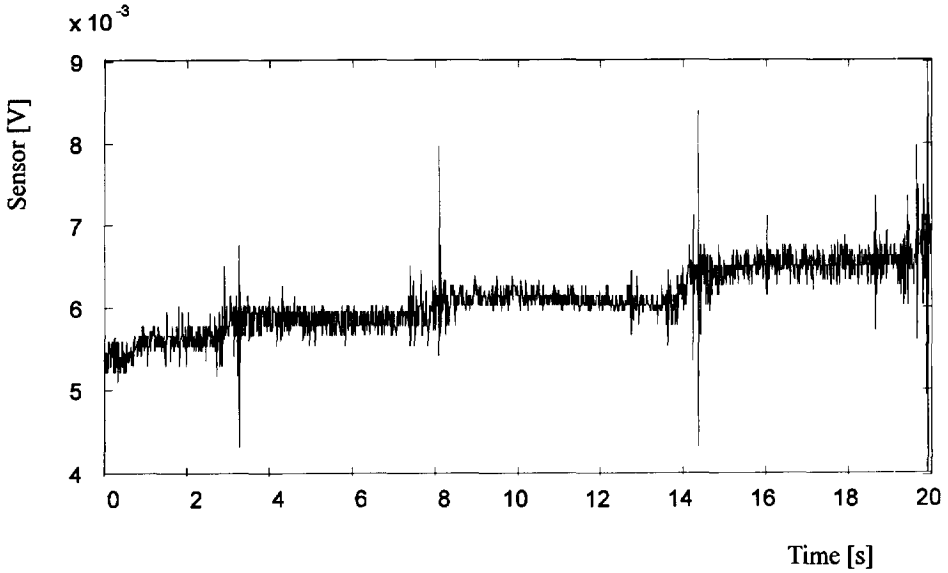


Fig. 6.5 Stiffness of the suspension of the rotor is measured by adding 50 gram, 100 gram, 200 gram and 300 gram to the rotor at resp. $t=1s$, $t=3s$, $t=8s$, and $t=14s$. The resulting displacement of $0.4 \mu m$, $0.8 \mu m$, $1.7 \mu m$ and $2.5 \mu m$ indicate a stiffness of $1.13e^6 N/m$.

The spiky appearance of the measurement results is caused by electronic noise measured with the sensor, and should be neglected for this experiment.

Measuring of the stiffness by adding mass to the rotor is not completely correct. By adding mass to the rotor, the mathematical model changes and the controller will mismatch. This can cause instability. Figure 6.6 shows such an effect. Here a mass of 400 gram is added to the rotor at $t = 12 s$, resulting in a drop of $3.5 \mu m$. At $t = 16 s$, an uncontrollable oscillation started, caused by the mismatch between controller and model.

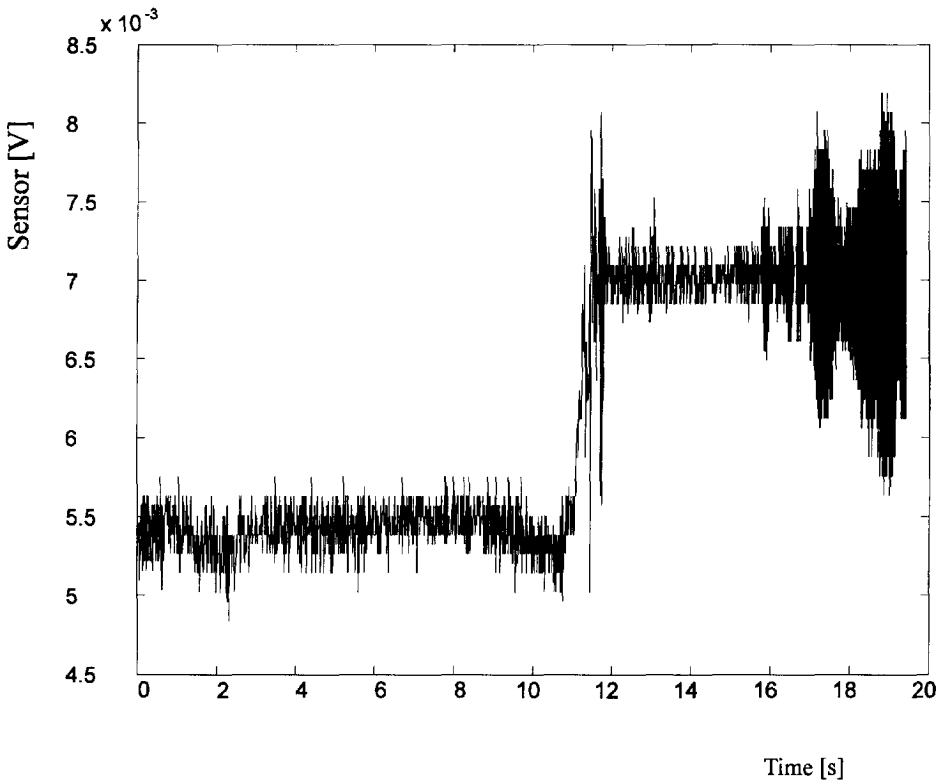


Fig. 6.6 Adding too much mass to the rotor can cause instability when the controller does not fit to the process any more. When 400 gram is added to the rotor at $t=12s$, the undesired oscillations starts at $t=16s$.

The last measurement performed with the suspension of the setup is presented in Figure 6.7. The noise measured with the position sensor is shown. The measured noise is approximately 4 mV peak to peak, corresponding to 800 nm position noise. This measurement was performed with a sensor gain of 5000 V/m. By adjusting this sensitivity from 10303 V/m to 5000 V/m, the loop gain decreases by a factor of 2 and the occurrence of high frequency oscillations at 500 Hz will vanish.

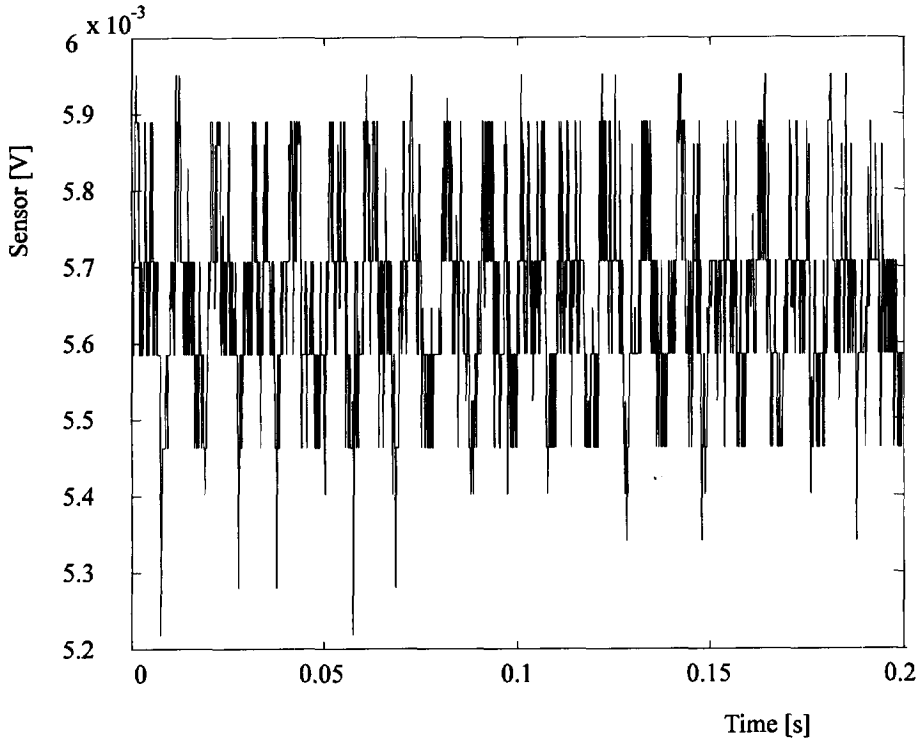


Fig. 6.7 Measured position noise with an eddy current sensor having 5000 V/m sensor sensitivity. The peak-peak value corresponds to 800 nm.

6.6 Propulsion

The experimental setup of Figure 6.1 was used to test the propulsion force characteristics and check whether the suspension would remain stable. Due to the layout of the experimental setup, not all locations were available to place secondary coils. Therefore, only two coils were placed, giving four locations where Lorentz forces are generated. Since the principle remains the same, Equation (4.8) can be used for the experimental set-up, provided the equation is divided by two to compensate for the missing center coil:

$$F_L = 2 \cdot N \cdot \mu_0 \cdot \mu_r \cdot I_{sec} \cdot N_{sec} \cdot b \cdot \left\{ \frac{(I_0 - \delta I)}{(S_0 + \delta Z)} + \frac{(I_0 + \delta I)}{(S_0 - \delta Z)} \right\} \quad (4.8)$$

Assuming that the magnetic bearings works perfectly, the following simplification can be made:

$$\begin{aligned} F_L &= N \cdot \mu_0 \cdot \mu_r \cdot I_{sec} \cdot N_{sec} \cdot b \cdot \frac{2I_0}{x_0} \\ &= K_{mot} \cdot I_{sec} \end{aligned} \quad (6.11)$$

with

$$K_{mot} = N \cdot \mu_0 \cdot \mu_r \cdot I_{sec} \cdot N_{sec} \cdot b \cdot \frac{2I_0}{x_0} = 2.27 \text{ N/A} = \text{motor constant.}$$

6.7 Experimental results of the propulsion force

Measuring the force produced by the SPU was the prime objective of the experimental set-up. Measuring the force at different levels of the secondary coil current was done. The results can be seen in Figure 6.7.

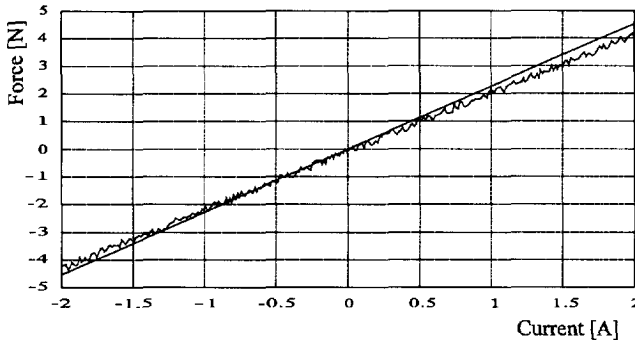


Fig. 6.8 Measured and predicted force/current diagram in propulsion direction. In the range of -2 A to 2 A the force is measured and the motor constant turned out to be slightly lower than predicted due to the air-gap being wider than nominal.

The motor constant measured is 2.10 N/A, which is less than predicted. The reason for this must be sought in a lower magnetic bearing field than was expected. The reason for this lower magnetic field must be sought in an air-gap being wider than nominal.

The maximum force is limited to approximately 5 N. This limitation is reached at 2 A, the maximum allowed current through the secondary coils. The magnitude of the force is according to the calculations done in Section 4.7. In combination with the mass of the rotor in the experimental set-up, the rotor must be able to achieve an acceleration of 20 m/s^2 , or twice the acceleration caused by gravity.

During these experiments, the behavior of the magnetic suspension was carefully watched. No change in magnetic bearing position was detected within $1 \text{ }\mu\text{m}$, so it was concluded that the mutual interaction can be neglected.

7 Application of the SPU: 6 degrees of freedom propulsion and suspension

7.1 Introduction

In order to show that the SPU can be used to form a contact free $XY\Phi$ positioning system, a second experimental set-up was built at the Laboratory for Micro Engineering, with three SPU's. The experience gained with a single SPU as described in Chapter 6, has been used. Figure 7.1 shows a photograph of the experimental set-up.

Since three degrees of freedom (X , Y and Φ) are controlled in the plane, and three degrees of freedom (Z , Ψ and ξ) are suspended (with a small stroke for tuning the height), the experimental set-up is, in fact, a six degrees of freedom, magnetically suspended and propelled positioning system.

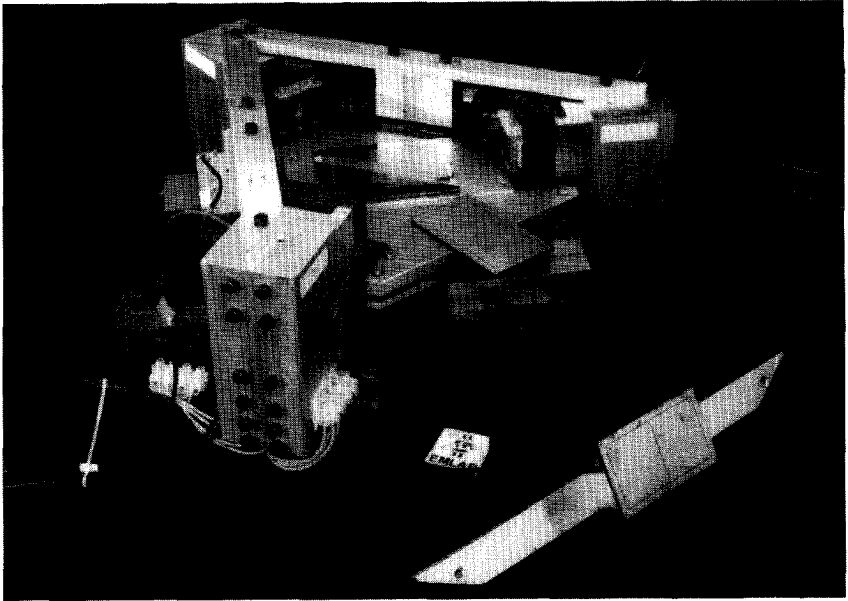


Fig. 7.1 Photograph of the experimental set-up equipped with three eddy-current sensors for the suspension and three capacitive sensors for positioning of the triangular platen in its plane. At the center the optical grid of the Heidenhain sensor, used in later experiments, is located.

7.2 Experimental set-up

Figure 7.2 shows that three SPU's are used to support and to propel a platen. The platen has three iron rotors with secondary coils on it.

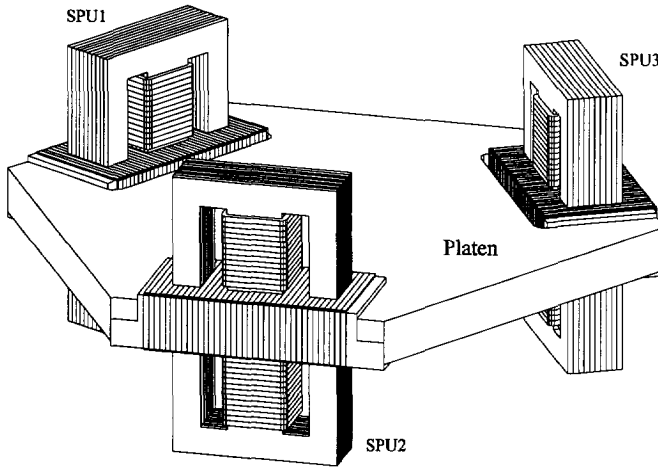


Fig. 7.2 Layout of the six degrees of freedom, magnetically suspended and propelled platen. Three SPU's are used. The sensors are not shown.

Each SPU has the following dimensions:

- E-core electromagnet dimensions: 60 mm x 20 mm x 40 mm,
- air-gap: 1 mm, and
- rotor dimensions: 80 mm x 20 mm x 40 mm.

The rotors are larger than the stators of the SPU's. This way a maximum travel of 10 mm in both the X and the Y direction is achieved. The dimensions of the E-core electromagnets are 60 mm x 40 mm x 20 mm. The platen is made of aluminum and is shaped the way shown in Figure 7.2. The thickness of the platen is 20 mm and its mass including the rotors is 3.07 kg. The three rotors are placed in the aluminum platen in a triangular configuration, at a center distance of 374 mm relative to each other.

The maximum current provided by the available amplifiers equals 1.2 A. This leads to a minimum wire diameter of:

$$d = \sqrt{\frac{1.2 \cdot 4}{\pi \cdot J_{max}}} = 0.4 \text{ mm} \quad (7.1)$$

with

$$J_{max} = 10 \text{ A/mm}^2$$

The number of windings that fits in the reserved space of 8 mm x 28 mm equals 896. The effective space is smaller than 10 mm x 30 mm (total space between magnetic poles) because the coil is wound on a coil-suspender. The resulting space equals 8 mm x 28 mm.

The reserved space was not completely filled, only 600 primary windings were used. Linearisation of the magnetic force is implemented using the differentially wound coils method described in Section 3.8. 300 primary windings are reserved for the control current and 300 windings are reserved for the stationary current. Combined with the maximum current of 1.2 A, the maximum force is calculated to be:

$$F_{max} = \frac{N^2 \cdot I^2 \cdot A \cdot \mu_0 \cdot \mu_{r,air}}{4 \cdot S_0} = 65 \text{ N} \quad (7.2)$$

and the average flux density:

$$B = \frac{\mu_0 \cdot \mu_{r,air} \cdot N \cdot I}{2 \cdot S_0} = 0.22 \text{ T} \quad (7.3)$$

The maximum flux density occurs when a current of 1.2 A is sent through the control coil, and the magnetomotive force becomes 720 Ampere-Turns. The average flux density occurs when no current is sent through the control coils and the magnetomotive force equals 360 Ampere-Turns.

The secondary coils are wound around the rotors. The secondary windings consist of 0.3 mm diameter wire, wound in three layers. This results in a height of 0.9 mm for 700 windings, of which 360 windings are always under the magnetic poles. The rest is in between or outside the poles. The center part of each secondary coil has an opposite winding direction compared to the outer parts of the coil. This compensates for the changing direction of the magnetic flux along the rotor.

The experimental set-up is controlled using the dSpace digital controller as discussed in Chapter 5. The power amplifiers are linear amplifiers and have the following specifications:

- maximum supply voltage: 80V,
- maximum output current: 1.2A, and
- bandwidth (low current): 20 kHz.

This results in a maximum slew rate of:

$$\left(\frac{dI}{dt}\right)_{max} = 3094 \text{ A/s}$$

With this slew-rate it will take approximately 1 ms to achieve a current level of 1.2 A, which is the maximum current output of the amplifier. This is fast enough to allow the system to have a bandwidth of 100 Hz.

The primary coils have a measured inductance of 22 mH at the operating point of the bearing and a resistance of 10 Ohm. The total power dissipation in the primary coils equals 86.4 Watt. A temperature rise of the primary coils was detected, but the coils stayed within working temperature.

The secondary coils have a measured inductance of 8 mH and a resistance of 18 Ohm. The slew rate can be calculated to be:

$$\left(\frac{dI}{dt}\right)_{max} = 8508 \text{ A/s}$$

and leads to a current change of 1.2 A in 0.36 ms. This is fast enough. The power dissipation is virtually none at standstill, and equals 26 Watt at full duty.

7.3 Dynamic equations of motion

Six forces are exerted on the platen by the six E-core electromagnets that provide the suspension. These six forces work in pairs, as described by Equation (7.4). Using a first order linearization, three forces are calculated. Each force is related to one SPU and can be described with:

$$F_s = 2K_c \cdot \delta z + 2K_i \cdot \delta i \quad (7.4)$$

where

F_s = the suspension force,

K_c = the negative stiffness, and

K_i = the force-current factor.

Newton's equilibrium laws yield the dynamic equations of motion:

$$\begin{aligned} m \cdot \ddot{z} &= F_1 + F_2 + F_3 - m \cdot g \\ J \cdot \ddot{\psi} &= F_1 \cdot l_f - (F_2 + F_3) \cdot \frac{1}{2} \cdot l_f \\ J \cdot \ddot{\xi} &= (-F_3 + F_2) \cdot \frac{1}{2} \sqrt{3} \cdot l_f \end{aligned} \quad (7.5)$$

where

- m = the mass of the platen,
- J = the mass moment of inertia of the platen,
- $F_{1,2,3}$ = the suspension forces for all three SPU's, and
- l_f = the force lever.

Substituting Equation (7.4) in Equation (7.5) and rewriting the dynamic equations of motion is necessary to come to a modal description of the transfer functions. Appendix C shows how the modal transfer functions are derived. For each of the three degrees of freedom for the suspension the following transfer functions are derived:

$$\begin{aligned} H_z(s) &= \frac{z}{I_z} = \frac{6K_i}{ms^2 - 6K_c} \\ H_\psi(s) &= \frac{\psi}{I_\psi} = \frac{6l_f K_i}{2Js^2 - 6l_f K_c} \\ H_\xi(s) &= \frac{\xi}{I_\xi} = \frac{6l_f K_i}{2Js^2 - 6l_f K_c} \end{aligned} \quad (7.6)$$

where

- $H_{z,\psi,\xi}$ = the transfer functions for Z , ψ and ξ , respectively,
- s = the Laplace operator, and
- $I_{z,\psi,\xi}$ = the virtual currents for Z , ψ and ξ , respectively.

The three virtual currents I_z , I_ψ and I_ξ must be transformed into currents I_1 , I_2 and I_3 that control the three SPU's. This can be done with the conversion matrices derived in Appendix C. The three sensor signals are transformed into Z , ψ and ξ information. When this strategy is used, a decoupled set of transfer functions is obtained that are controlled with a decoupled set of controllers.

The dynamic equations of motion for the propulsion of the platen are calculated using the the same strategy. Appendix C shows how the transfer functions are derived. Subsequently, three transfer functions are obtained that are decoupled. These transfer functions are:

$$\begin{aligned}
 H_x(s) &= \frac{X}{I_x} = \frac{K_{mot}}{ms^2} \\
 H_y(s) &= \frac{Y}{I_y} = \frac{K_{mot}}{ms^2} \\
 H_\phi(s) &= \frac{\phi}{I_\phi} = \frac{K_{mot} \cdot I_f}{Js^2}
 \end{aligned} \tag{7.7}$$

where

K_{mot} = the magnetic constant or motor constant,

$I_{x,y,\phi}$ = the virtual currents controlling X, Y and Φ , respectively.

Again, the virtual currents I_x , I_y and I_ϕ must be transformed into currents I_4 , I_5 and I_6 that control the propulsion forces generated by the SPU's. The capacitive sensor signals must also be converted in order to get correct XY Φ information for the controllers.

7.4 Sensor system layout

For the experimental set-up two types of sensors are used. Eddy current sensors are used for the suspension function and capacitive sensors are used for the positioning in the XY Φ plane. At a later stage the capacitive sensors are replaced by a Heidenhain incremental encoder.

The eddy current sensors chosen are commercially available from EPRO. They perform well for magnetic bearings. The stroke of the sensors is 2 mm, with a position accuracy of 1 μ m. The signal to noise ratio is 72 dB, allowing for sub-micrometer position stability.

For the positioning of the platen capacitive sensors are used. The accuracy of the sensor depends on the electronics used. A stroke of 10 mm of the sensors results in an accuracy of 0.1 mm, at a signal to noise ratio of 40 dB. This could be boosted when electronics were used with a much lower bandwidth and a better signal/noise ratio. The best results achieved with these better electronics imply an accuracy of 2.7 μ m at a range of 10 mm, or a signal/noise ratio of 71 dB.

The layout of the six sensors is shown in Figure 7.3. As can be concluded from their distribution along the set-up, the sensors do not measure the six degrees of freedom directly. This means that a coordinate transformation is needed to obtain correct position and angle information.

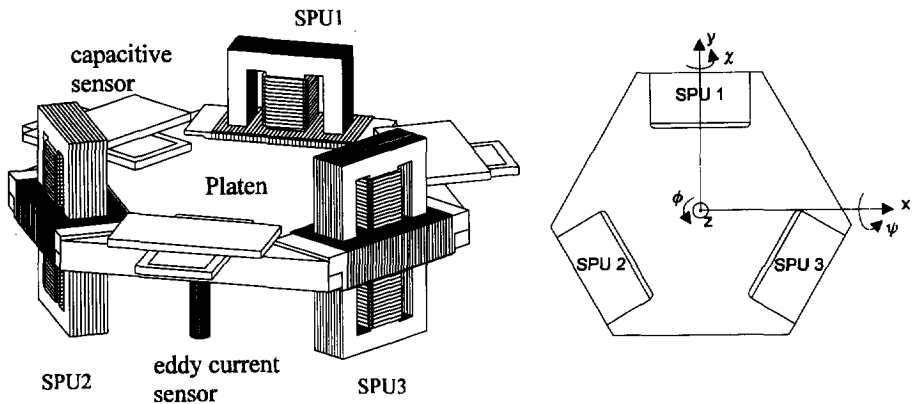


Fig. 7.3 Sensor layout of the experimental set-up. Three eddy current sensors are used to control the suspension; three capacitive sensors are used to control the propulsion.

The capacitive sensors that were available exhibit quite some noise. As a consequence the static stiffness had to be adjusted to a low value initially, (10^4 N/m), in order to prevent the system from becoming unstable due to the noise. Filtering the sensor signal had marginal effect only. High stiffness can be reached with a better sensor, the Heidenhain sensor.

7.5 Control of the six degrees of freedom

Each of the six transfer functions described with Equations (7.6) and (7.7) has a matching controller. The six controllers are all tame PID controllers or Lead-Lag filters. The controllers are designed to achieve the following characteristics for the closed loop system:

- suspension Bandwidth: 100 Hz,
- propulsion Bandwidth: 100 Hz,
- suspension Stiffness: $4 \cdot 10^6$ N/m,
- propulsion Stiffness: 10^6 N/m,
- overall damping: $\beta = 0.707$, and
- steady state error: smaller than the sensor resolution of $1 \mu\text{m}$.

The controller is designed with MATLAB software. The digital controller provided by dSpace GmbH has an interface with SIMULINK, allowing for a

simple connection to MATLAB. A simple push-button action implements the designed controller and makes the overall system ready for use. Figure 7.4 shows a diagram of the SIMULINK file, showing clearly the controllers, the transformation matrices and the input-output connections with the DA and AD converters. The controller is implemented on a TMS320C40 DSP processor board with 10 kHz sample rate, as discussed in Chapter 5.

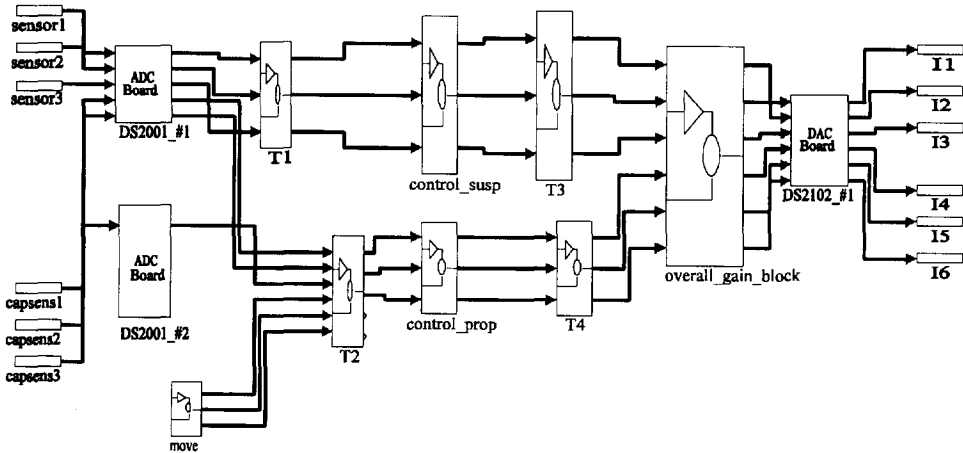


Fig. 7.4 Implementation of a six input- six output controller system for the control of the experimental set-up. Controllers, coordinate transformation matrices and AD/DA converters are shown. The overall_gain_block is added for computer controlled emergency shutdown.

The required phase margin of 67 degrees (due to the damping of $\beta=0.707$) leads to a M_d factor of 24. The time constant τ_d is derived with Equation (3.27) and becomes 0.0124 s for the suspension and 0.0005 s for the propulsion controllers. The design goal of the static stiffness for the suspension leads to an M_i of 10; the propulsion stiffness dictates an M_i of 15. Allowing a phase-loss of 5 degrees at the crossover frequency, τ_i becomes 0.1238 s for the suspension and $\tau_i=0.005$ s for the propulsion. With these values the controller parameters are fully determined.

7.6 Measurement results for suspension

The following experiments are performed on the suspension:

- The process transfer function, the loop gain function and the closed loop transfer function are measured in order to check the system's dynamic behavior.
- The static stiffness is determined by measuring the effect of adding mass to the rotor.
- The position accuracy is investigated by looking at the sensor signals under various conditions.

The measurements of all the dynamic transfer functions were performed with a HP dynamic signal analyzer. The results, Bode diagrams, of the measurements in suspension direction are presented in Figures 7.5, 7.6 and 7.7. Figure 7.5 shows the measured and the calculated Bode diagram for the process transfer function for the Z direction. Figure 7.6 shows the measured and the calculated transfer functions for the loop-gain and Figure 7.7 shows the calculated and measured closed loop transfer function for the Z direction.

Two features draw attention to the Bode plot of Figure 7.5, for these features were not predicted. The most obvious effect is observed in the phase diagram. Starting at approximately 80 Hz, extra phase lag is introduced. This is caused by eddy currents. The rotors of the SPU's are not laminated, thus allowing this possibility. The second oddity appears at 750 Hz. Clearly an extra eigenfrequency appears here, caused by unmodelled high frequency oscillations of either the platen or the stators of the SPU's.

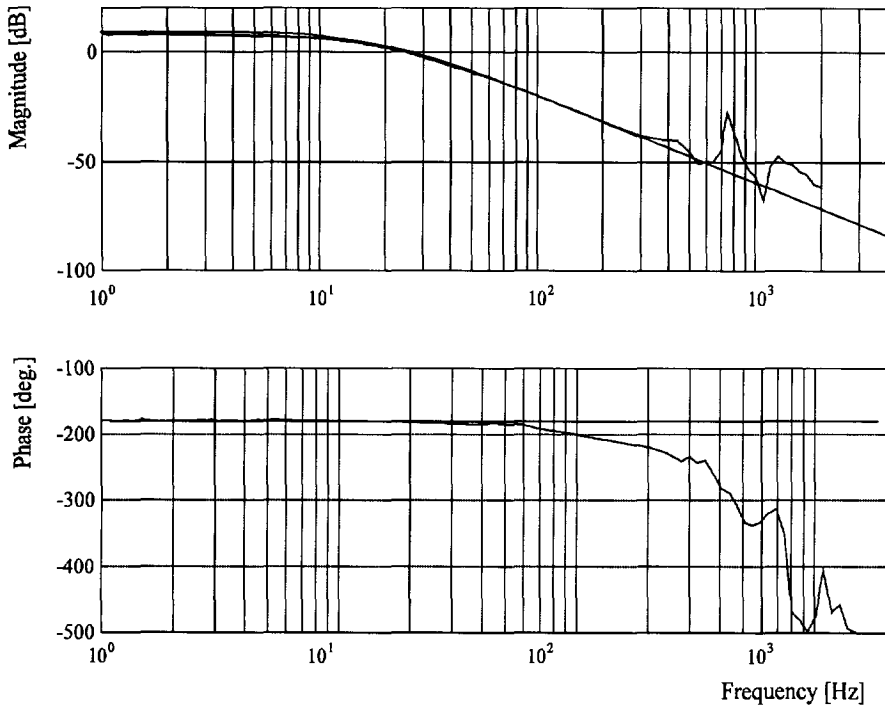


Fig. 7.5 Measured and calculated Bode diagram of the process transfer function in the Z direction. The prediction and the measurement coincide very well, except at the unmodelled high frequency oscillation of 750 Hz. Also an extra phase lag starting at 80 Hz is measured, caused by eddy currents.

The measured Bode plot of the loop-gain function shown in Figure 7.6 shows the same deviations from the predicted curve as was mentioned above. The eigenfrequency at 750 Hz can cause instability as soon as its magnitude increases beyond 0 dB. At 750 Hz insufficient phase margin is available, thus resulting in the oscillation at 750 Hz. This means that if more stiffness is required in the experimental set-up, increase of the magnitude of the loop-gain will not be possible. Some measures against the oscillation at 750 Hz must be taken first, before the stiffness can be increased.

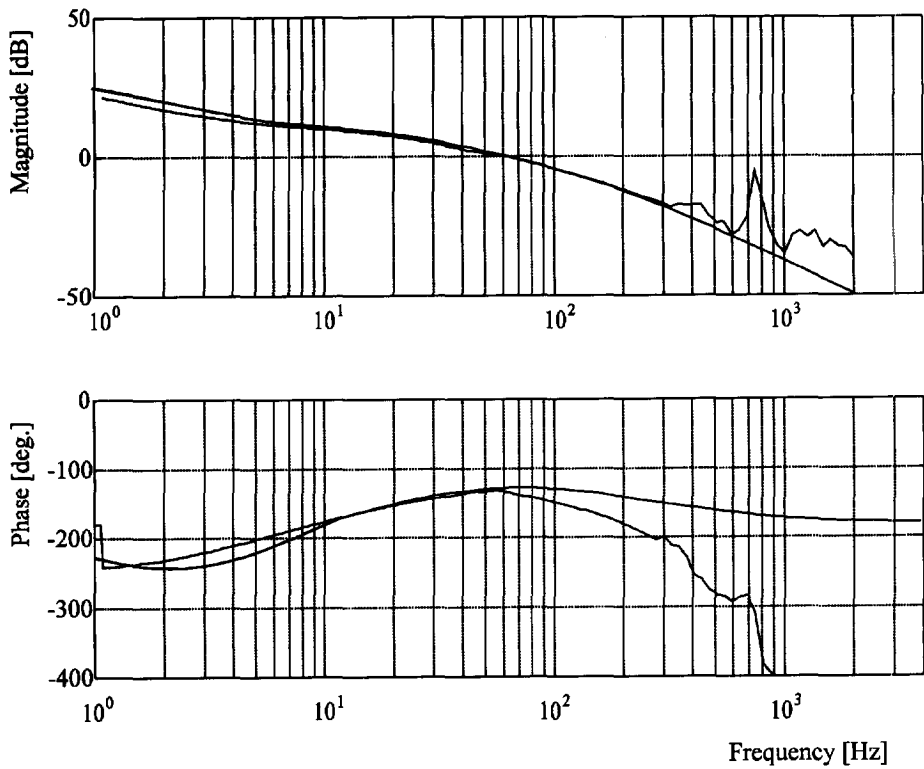


Fig. 7.6 Measured loop-gain transfer function in the Z direction, compared with the predicted loop-gain function. The deviations, exhibited in Figure 7.5, can be observed: the phase lag and the eigenfrequency at 750 Hz.

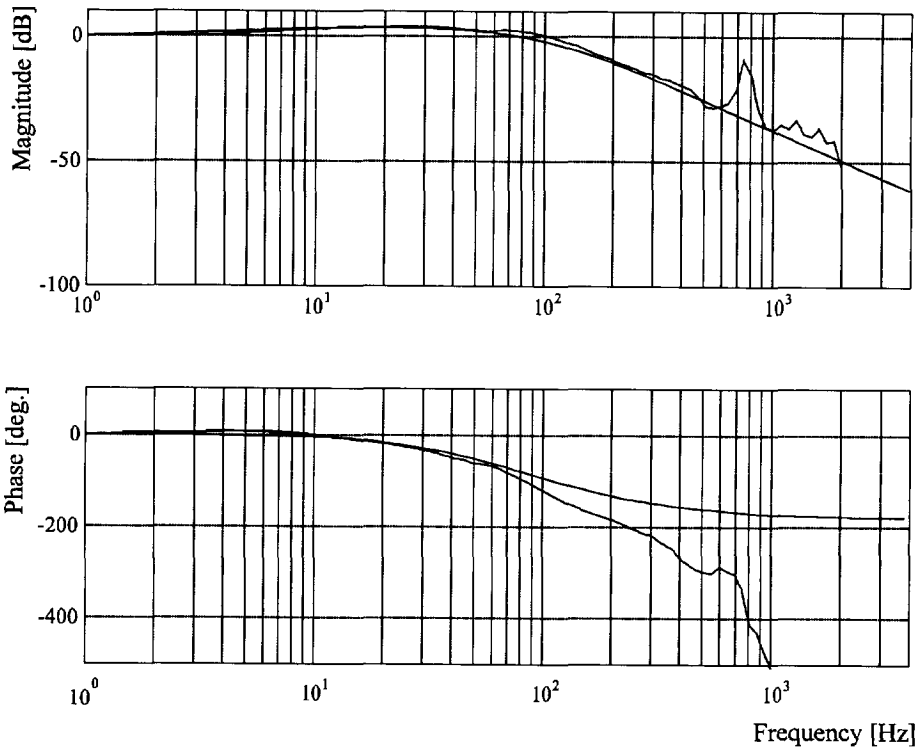


Fig. 7.7 Measured and calculated closed loop transfer function in the Z direction. The aim of a closed loop bandwidth of 100 Hz is achieved. The phase lag starting at 80 Hz is still present as well as the unmodelled high frequency oscillation at 750 Hz.

Analysis of the closed loop Bode diagram in the Z direction shows that the desired 100 Hz bandwidth has been achieved. Also visible is the extra phase lag starting at 80 Hz, introduced by the eddy currents and the effect of the unmodelled high frequency oscillation at 750 Hz. This eigenfrequency also introduces a phase shift, the value of which will amount to 180 degrees per eigenfrequency.

Analysis of the experimental set-up has resulted in two possible causes for the unmodelled high frequency oscillation. The oscillation is either caused by inadequate stiffness of the platen, resulting in a bending mode of the platen of 750

Hz, or by insufficient stiffness of the support structure of the SPU. This matter was not further researched.

The static stiffness is analyzed by adding mass to the platen and by measuring the position deviation using the sensors of the SPU. This measurement was not performed for the ψ and the ξ directions, but only for the Z direction. The results for this measurement are shown in table 7.1.

added mass [gr]	Z position [μm]	Z deviation [μm]	stiffness [10^6N/m]
0	8.916	-	-
100	9.151	0.235	4.25
300	9.623	0.472	4.23
400	9.864	0.241	4.14
500	10.11	0.246	4.06
600	10.36	0.25	4
800	10.87	0.51	3.92
900	11.152	0.282	3.54
1000	11.43	0.278	3.59
1100	11.72	0.29	3.44
1400	12.74	1.02	2.94

Table 7.1 Measurement results for the determination of the stiffness measurement of the platen in the Z direction.

The results obtained from the stiffness measurement are somewhat surprising. The stiffness was designed to be $4 \cdot 10^6$ N/m and this was easily obtained. But the stiffness seems to drop steadily when more mass is added to the table. It should be mentioned at this point that adding mass to the table is not entirely correct, as was mentioned in Chapter 6 already, and from there the cause could be explained.

The measurement was stopped when 1400 gram was added to the table for at this value the amplifier reached its maximum current level and the support of the

platen completely collapsed. So, the maximum payload for the platen turns out to be 1400 gram in this experiment.

The third measurement looks at the position accuracy measured with the eddy current sensors. Three measurements were done with the eddy current sensors themselves. These measurement results are presented in Table 7.2.

axis	no control	suspension	suspension and propulsion
Z	0.13 μm	0.4 μm	0.5 μm
Ψ	23 μrad	68 μrad	84 μrad
ξ	10 μrad	31 μrad	41 μrad

Table 7.2 Noise measurements performed on the three degrees of freedom of the suspension of the experimental set-up. The average position errors are shown.

The values shown in Table 7.2 indicate that the required position accuracy in the suspension direction can easily be achieved with the eddy current sensors. When the control is switched off, the sensors measure the least amount of noise, which is to be expected. When the suspension is turned on, the noise measured increases with a factor of three. This is caused by the movement of the platen, a fact that can also be heard acoustically. When the propulsion is also switched on, the currents that flow through the secondary coils add a little extra noise to the suspension. The overall system still behaves satisfactorily.

7.7 Measurement results for propulsion

The measurements performed on the propulsion part of the experimental set-up will be discussed in this Chapter. The following measurements were done:

- The process transfer function, the loop gain function and the closed loop transfer function are measured in order to check the system's dynamic behavior.
- Positioning accuracy is measured by looking at different types of sensors used in propulsion direction.
- Step responses were measured in order to determine the systems static behavior.

The position in propulsion direction is measured with capacitive sensors designed and manufactured at the Laboratory for Micro Engineering. These sensors do have, unfortunately, too much noise. This results in poor system dynamic behavior. Initially a closed loop bandwidth of 5 Hz was implemented in order to be able to analyze the experimental set-up. Higher bandwidths resulted in an unstable system.

At a later stage the noisy capacitive sensors were partly replaced by an optical grid made by Heidenhain, the PP109R optical encoder. This encoder only measures the X and the Y position, while the rotation Φ must be kept within a few mrad. The angle Φ can not be measured with the Heidenhain sensor, so the capacitive sensors were used for this purpose.

Figure 7.8 shows the result of the measurements on the process transfer function, with the measurement and the theoretical process transfer function shown together in one graph. The difference is clear. The real process seems to behave rather like a mass spring damper system than a double integrator. This results in the different behavior of the phase as well as the much lower gain of the actual process. By adjusting the process transfer function into a second order damped second order system, an adaptation is made so that a good controller can be designed. This adaptation is also shown in Figure 7.8.

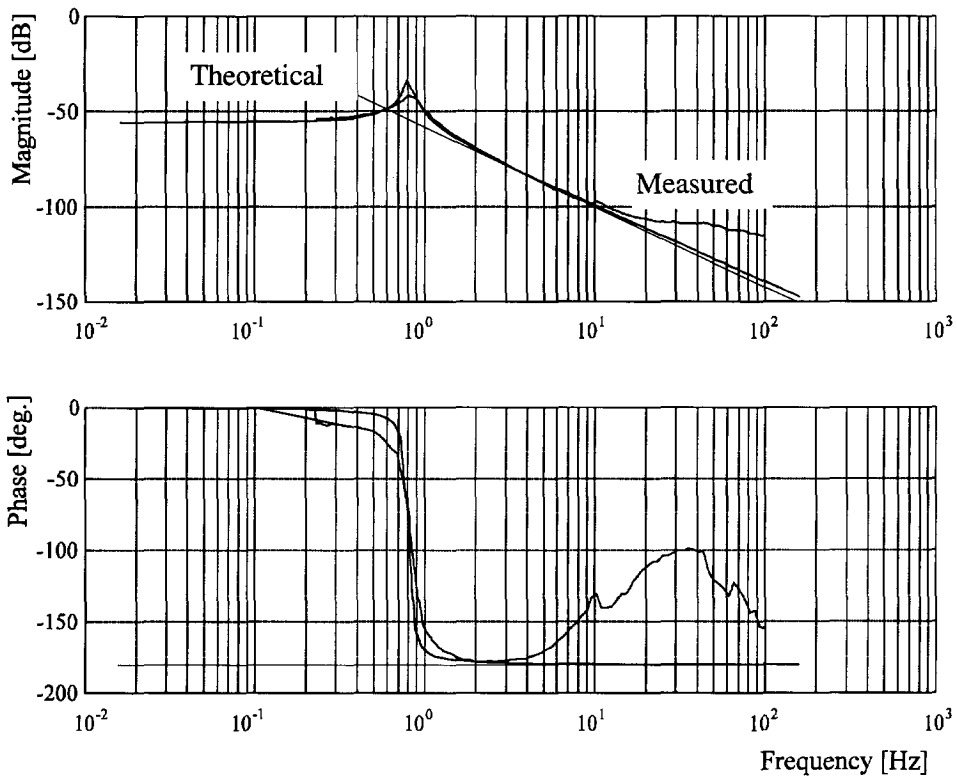


Fig. 7.8 Bode plot for the process transfer function in the Y direction. The predicted theoretical double integrator configuration of the system is replaced by an adapted damped second order configuration that shows better resemblance with the actual measured performance.

The loop gain is measured, and compared to the loop gain computed for the adapted process. The result is shown in Figure 7.9. The crossover frequency is found close to 5 Hz.

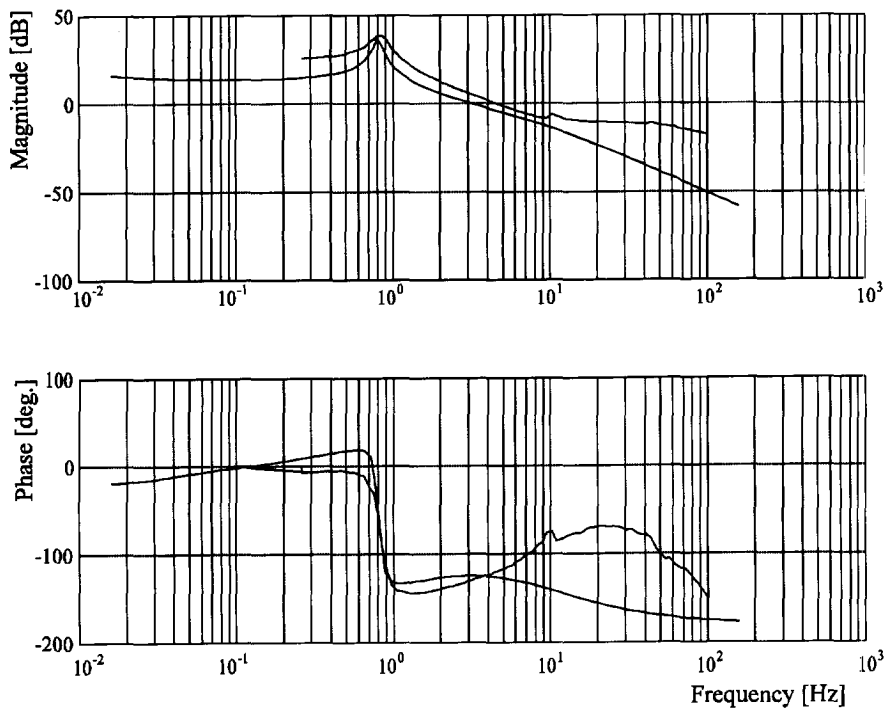


Fig. 7.9 The measured and calculated loop gain functions coincide reasonably well. The cross-over frequency is approximately 5 Hz.

The final measurement performed on the dynamic behavior of the propulsion of the platen is given in Figure 7.10. Here, the closed loop frequency response is shown. The closed loop bandwidth is approximately 7 Hz, which coincides with the specified bandwidth of these experiments. A higher bandwidth could not be reached with this set-up where capacitive sensors are used.

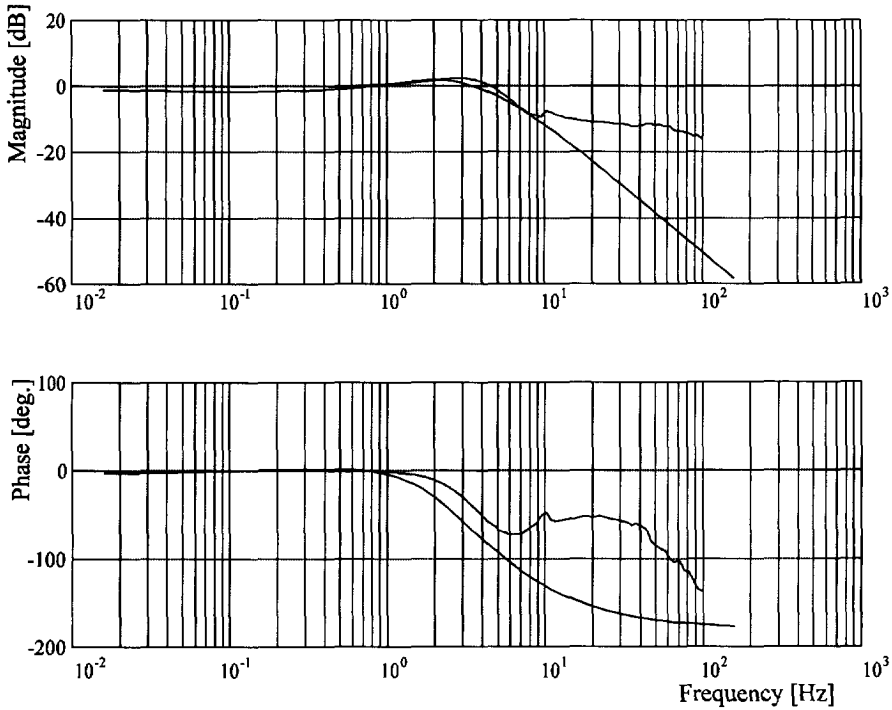


Fig. 7.10 Measured and theoretical Bode plots of the closed loop response in the X direction. A closed loop bandwidth of 7 Hz is achieved. At frequencies above 10 Hz the noise generated by the capacitive sensors dominates the frequency response and further increase of both the stiffness and the closed loop bandwidth is not possible.

At this stage it was decided to add a better sensor to the experimental set-up. The objective is still to achieve the 100 Hz bandwidth and the 10^6 N/m stiffness. The sensor is the Heidenhain PP109R sensor, as was mentioned before and as described in Chapter 5. This sensor has a much better signal-noise ratio and therefore a higher bandwidth could be achieved. A bandwidth of 100 Hz was implemented for both the X and the Y direction, together with a closed loop bandwidth in the Φ direction of 7 Hz. The static stiffness was set to 10^6 N/m. The implementation showed no further difficulties, so it was concluded that the two specifications are indeed met. Unfortunately, the digital controller does not allow a dynamic behavior measurement when the incremental encoder is used, so the

closed loop response could not be measured. An extension of the digital controller will be necessary before this measurement can be performed.

The Φ direction was still measured with the capacitive sensors because at the time of the experiments no other sensors were available. The influence of the noise in the Φ direction still has its influence on the performance in the X and the Y direction. The measurement results on the position noise are shown in Table 7.3.

axis	no control	suspension	suspension and propulsion	Heidenhain
X	23 μm	66 μm	101 μm	0.3 μm
Y	15 μm	35 μm	46 μm	0.2 μm
Φ	1.9 mrad	4.9 mrad	6.8 mrad	-

Table 7.3 Position accuracy in the propulsion direction with the platen under control with the capacitive sensors and with the Heidenhain sensor.

As can be concluded from Table 7.3, the position accuracy observed with the Heidenhain sensor is much better than the position observed with the capacitive sensors. The noise measured with the Heidenhain sensor exceeds the resolution of the sensor due to the fact that noise in Φ direction still influences the positioning accuracy of the platen. A clear conclusion can be drawn: The position stability is strongly dependent on the quality of the sensor used.

The last experiment performed on the XY Φ stage deals with the step response. A typical measurement of a step response is shown in Figure 7.11.

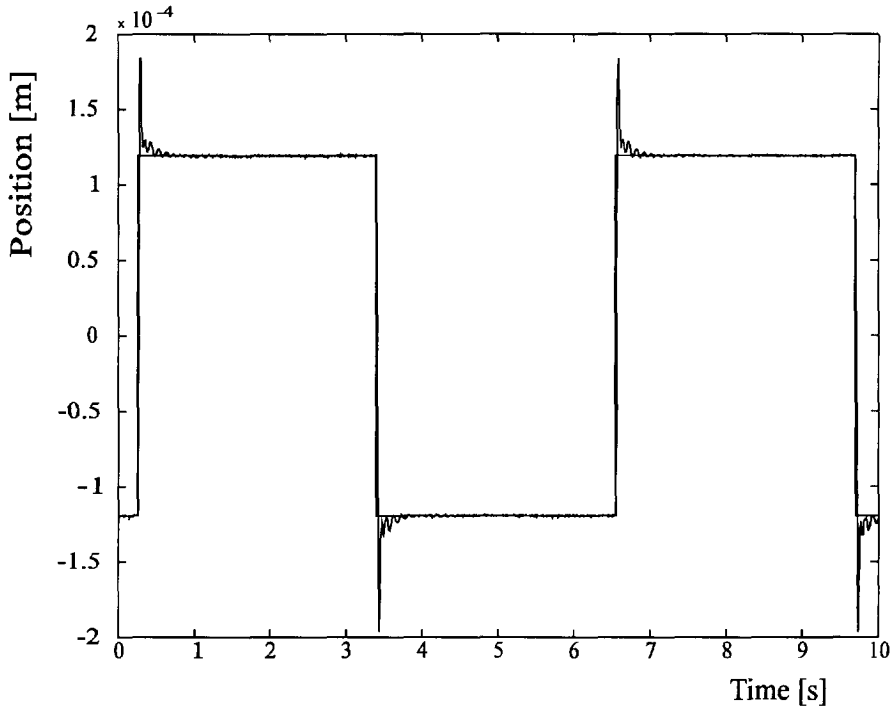


Fig. 7.11 Measured step response in the X direction. This measurement is performed with the Heidenhain PP109R incremental encoder.

The following parameters can be determined from the step-response:

- maximum overshoot: 27%,
- peak time: 12 ms, and
- steady state error: 0.3%

The “Peak time”, T_p , can be used to make an estimate of the closed loop bandwidth. Using

$$T_p = \frac{\left(1 - 2 \cdot \beta^2 + \sqrt{2 - \beta^2 \cdot (1 - \beta^2)}\right)^{1/2}}{2 \cdot f_b \cdot (1 - \beta^2)} \quad (7.8)$$

derived in [32], the estimated closed loop bandwidth is 95 Hz.

8 Scaling factors and Design rules

8.1 Introduction

Scaling of the SPU is important for estimating how wide the field of application of the SPU can be, without changing the relative geometrical sizes of the mechanical set-up.

This Chapter deals with the scaling factors related to the SPU element. It starts by deriving a scaling factor for the maximum current through a coil. The scaling factors were confirmed by [40] and [32] by realizing scaled experimental set-ups of the magnetic bearing actuator and the $XY\Phi$ positioning system, respectively. Other important factors will be summarized in a table. The Chapter concludes with design rules for an SPU. These design rules are preceded by focus points and boundary conditions that must be taken into account.

8.2 Scaling factors for the SPU

8.2.1 Geometric scaling factors

In order to correctly analyze the changes of different parameters of the SPU, it is assumed that all geometrical measures are scaled isometrically. This means that if the model is scaled with a factor S , every dimension is scaled with a factor S . This isometric scaling leads to the following:

- the air-gap $S_0, \delta S, x, z$ scale with S ,
- the cross-sectional area A scales with S^2 , and
- the volume and the mass m scale with S^3 .

8.2.2 Electric circuit scaling factors

The scaling of the electric parameters of the SPU are derived from a theoretical analysis made by M. Lazeroms [40], member of the project team. The temperature of the coils plays a key role in the following analysis.

When the diameter of the wire of a coil decreases while the current through that coil remains the same, the temperature of the coil will rise and eventually the isolation will melt. The current should therefore be scaled.

In order to analyze the relationship between the scaling factor S and the current through the coil, the assumption of a constant maximum temperature of the coil is assumed. Figure 8.1 shows an intersection of the wire.

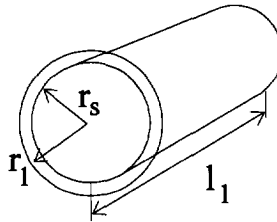


Fig. 8.1 Sketch of a wire with the geometrical parameters used for the scaling factors.

The equation for the conduction of heat in a wire is:

$$\frac{dQ}{dt} = -k \cdot A \cdot \frac{dT}{dx} \quad (8.1)$$

with:

- Q = the energy generated by the current,
- t = time,
- k = the conduction of heat to the surrounding environment,
- A = the area of the wire,
- T = the temperature in the wire, and
- x = the distance from the center of the wire.

For a cylinder with radius r_l , dQ/dt is equal to the dissipated power of this cylinder:

$$\frac{dQ}{dt} = P = I_t^2 \cdot R = (J \cdot A_{el})^2 \cdot \frac{\rho l_t}{A_{el}} = J^2 \cdot \rho \cdot \pi \cdot r_t^2 \cdot l_t \quad (8.2)$$

with:

R = the electrical resistance,
 ρ = the specific resistance, and
 J = the current density.

The dissipated power at the surface of the wire can be written as:

$$\frac{dQ}{dt} = J^2 \cdot \rho \cdot \pi \cdot r_s^2 \cdot l_t \quad (8.3)$$

Outside the wire, there is no increase of energy, so for every fictitious cylinder outside the thread, the dissipated power is the same as on the surface of the thread. The area of the surface of the cylinder with radius r_l is $A = 2\pi \cdot r_l \cdot r_t$, while dx can be replaced by dr , so Equation (8.1) can be written as:

$$J^2 \cdot \rho \cdot \pi \cdot r_s^2 \cdot l_t = -2 \cdot \pi \cdot k \cdot l_t \cdot r_l \cdot \frac{dT}{dr} \quad (8.4)$$

Integration of Equation (8.4) gives:

$$\frac{1}{2} J^2 r_s^2 \int_{r_t}^{r_l} \frac{1}{r_l} dr_l = \int_{T_t}^{T_l} -k dT \quad (8.5)$$

where r_f is the radius of a fictitious cylinder outside the thread where the temperature is T_f . From Equation (8.5) the following expression for the difference of temperature between two fictitious cylinders can be derived:

$$\Delta T = -\frac{J^2 \cdot \rho \cdot r_s^2}{2k} \left(\ln \frac{r_f}{r_s} \right) \quad (8.6)$$

When the radius r_f is assumed to scale with a factor S and the difference of temperature is independent of the scaling, Equation (8.6) in terms of scaling factors becomes:

$$[S^0] = -\frac{J^2 \cdot \rho \cdot [S^2]}{2k} \left(\ln \frac{[S]}{[S]} \right) \quad (8.7)$$

The current density thus scales with a factor $J=[S^{-1}]$, so the current through the coil scales as $i=[S^1]$.

The ohmic resistance of the coil is given by:

$$R = \frac{\rho \cdot l}{A} \quad (8.8)$$

and scales as:

$$[R] = \frac{\rho \cdot [S]}{[S^2]} = [S^{-1}] \quad (8.9)$$

Using Equation (3.45):

$$L = \frac{\mu_0 \cdot N^2 \cdot A}{2 \cdot x \cdot \frac{l_{iron}}{\mu_{r,air}} + \frac{l_{iron}}{\mu_{r,iron}}} \quad (3.44)$$

and assuming no change in the number of windings N , the scaling of the self inductance L is:

$$[L] = \frac{\mu_0 \cdot N^2 \cdot [S^2]}{2 \cdot [S] + \frac{[S]}{\mu_{r,iron}}} = [S] \quad (8.10)$$

The electric time constant of the coil:

$$\tau_e = \frac{L}{R} \quad (5.8)$$

changes with scaling and has a scaling factor of:

$$[\tau_e] = \frac{[S]}{[S^{-1}]} = [S^2] \quad (8.11)$$

8.2.3 Magnetic circuit scaling factors

The magnetic constant, K_m , representing the magnetic circuit is, given by:

$$K_m = \frac{1}{4} \cdot \mu_0 \cdot \mu_{r,air} \cdot N^2 \cdot A \quad (3.14)$$

This scales as:

$$[K_m] = \frac{1}{4} \cdot \mu_0 \cdot \mu_{r,air} \cdot N^2 \cdot [S^2] = [S^2] \quad (8.12)$$

The magnetic force,

$$F = K_m \cdot \frac{I_0^2}{S_0^2} \quad (3.14)$$

scales with:

$$[F] = [S^2] \cdot \frac{[S]^2}{[S]^2} = [S^2] \quad (8.13)$$

Two other factors of importance are the negative stiffness:

$$K_c = \frac{2 \cdot K_m \cdot I_0^2}{S_0^3} \quad (3.16)$$

that scales as:

$$[K_c] = \frac{2 \cdot [S^2] \cdot [S]^2}{[S]^3} = [S] \quad (8.14)$$

and the force-current factor:

$$K_i = \frac{2 \cdot K_m \cdot I_0}{S_0^2} \quad (3.16)$$

scaling with:

$$[K_i] = \frac{2 \cdot [S^2] \cdot [S]}{[S]^2} = [S] \quad (8.15)$$

8.2.4 Control scaling factors

This Section summarizes the scaling factors of the controller characteristics, assuming that no change is desired in the closed loop performance of the suspension and of the propulsion.

The poles of the open-loop transfer function of the suspension:

$$p_{1,2} = \sqrt{\frac{2K_c}{m}} \quad (3.21)$$

scale as:

$$[p_{1,2}] = \sqrt{\frac{[S]}{[S^3]}} = [S^{-1}] \quad (8.16)$$

The design of the closed loop characteristics do not depend on the open-loop poles. Therefore, it is concluded that $\tau_i, \tau_d, M_i, M_d, P$ and K_{di} remain unchanged.

The static stiffness, closed loop bandwidth and steady state error also remain unchanged.

8.2.5 Overview of scaling factors

Table 6.1 shows the scaling factors for various parameters of the process and the electromagnetic force, based on the equations given in Chapter 3.

variable	symbol	scaling factor
air-gap length	$S_0, \delta S, x, z$	S
cross-sectional area	A	S^2
mass	m	S^3
current density	J	S^{-1}
currents	$I_0, I_{sec}, \delta I$	S
ohmic resistance	R	S^2
self inductance	L	S
electrical time constant	τ_e	S^2
magnetic constant	K_m	S^2
electromagnetic suspension force	F	S^2
negative stiffness	K_c	S
current -force constant	K_i	S
poles of the process transfer function	$p_{1,2}$	S^{-1}

Table 8.1 Overview of the scaling factors, applicable to the SPU. All other factors not mentioned scale with $[S^0]$.

8.3 Mechanical design rules for the SPU

8.3.1 Focus points

When trying to design an SPU using the design rules described in this Section, several points of attention must be taken into account. These points of attention, or focus points, will be mentioned below.

- The scaling of the coil does not take into account that the isolation of the wire stays at a constant thickness. In fact, this isolation is not taken into account at all. A correction for this must be made, using Figure 3.12. The design rules can be used accurately, with a maximum error of 10%, for wire diameters ranging from relatively large down to 1 mm. For smaller wire diameters the correction based on Figure 3.12 must be taken into account.
- Scaling the electrical properties will affect the choice of the amplifier. Using the same amplifier for different scales of an experimental set-up will automatically result in non-optimal designs, since the amplifier is designed for a certain L , R , and τ_e .
- The poles of the transfer function play a more important role in the scaling than might be suspected. A control strategy, suggested in [32], places the zero of the PD controller at the pole of the process transfer function. Using this alternative strategy, the controller parameters will certainly change with scaling. Future research will involve more complex controllers where this alternative strategy might be useful.

8.3.2 Rules for designing the SPU

A design of an SPU can be made in seven consecutive steps. Each step will be discussed below, with reference to the Sections of this Thesis.

Step 1

Make an estimate of the necessary suspension force. This force is needed to:

- lift the mass,
- accelerate the mass to achieve position, and
- compensate for external disturbance forces.

Use a high saturation magnetic material and calculate the cross-sectional area of the central magnetic pole with:

$$A = \frac{2 \cdot \mu_0 \cdot F}{B^2} \quad (8.17)$$

and use $B = B_{sat} / 2$ of the material applied. For very high accuracy, $B = B_{sat} / 4$ is recommended.

Consider Sections 3.2, 3.5, 3.6, and 3.7.

Step 2

Choose an appropriate air-gap. Several considerations can be taken into account:

- The air-gap must be large enough to allow for room for the secondary coils. An iteration with design step 6 might be appropriate.
- Room must be reserved for a small operating range of the bearing. This way the bearing can be used to correct manufacturing errors in a guideway or in the magnetic circuit, and for in-focus correction in some specific applications.
- The air-gap (room for secondary coils plus operating range) must be kept within 10% of the magnetic pole width. If this can not be achieved, then the stray effects of the magnetic field will result in a bad magnetic circuit.

Step 3

Decide on the number of primary windings. The area reserved for the primary windings plays a key role in this decision. If thin wires are used, the influence of the isolation, Figure 3.2, must be taken into account. The magnetomotive force, $N \cdot I$, can be calculated with Equation (3.42) and using Figure 3.10 helps to decide on the wire diameter and the number of windings.

The amplifier plays a major role in this step. If the amplifier will be designed to match the magnetic circuit characteristics, then the considerations of Section 3.6 are not important. Usually, however, the amplifier is bought and the magnetic circuit is designed to match the amplifier specifications. In this case, Section 3.6 is very important.

Consider Sections 3.2, 3.6, 3.8 and 5.6. Calculate I_0 , N , and wire diameter d .

Step 4

Choose the closed loop bandwidth, stiffness and damping of the magnetic suspension. These characteristics are entirely free to choose for the designer. Care must be taken with systems that have high stiffness, for they tend to show a greater sensitivity to unmodelled high frequency oscillations than normal stiffness systems. Calculate the appropriate controller using Section 3.4. Check the stability of the designed servo system with the Nyquist criterion [67] or with computer simulations.

The support structure must be designed to be stiff enough, otherwise system performance will be degraded by unmodelled high frequency oscillations.

Step 5

Estimate the necessary propulsion force. This force is the sum of:

- the forces needed for propelling the suspended mass, and
- a force needed for compensation of parasitic forces.

Note that the propulsion force is limited to maximally 5% of the suspension force, as was shown in Section 4.7.

Step 6

Calculate a wire diameter, a maximum current and the number of windings of the secondary coil using Sections 4.2, 4.3, 4.5 and 4.7. The size of the air-gap decides on the maximum current and the number of ampere-windings that fits in the SPU. An iteration with step 2 may be necessary.

Step 7

Choose the closed loop bandwidth, stiffness and damping of the magnetic propulsion. Similar to Step 4, the designer is completely free to choose these characteristics. A Nyquist criterion check is not necessary but simulations are recommended. Calculate the appropriate controller characteristics using Section 4.4.

9. Conclusions and Recommendations

9.1 Conclusions

A conceptual design for a suspension and propulsion unit, to be used for sub-micrometer positioning, has been investigated, realized and tested with success, in order to make a step forward in the field of sub micrometer positioning and guiding in general.

The design strategy for the SPU, in combination with the controller design algorithms, leads to a stable SPU. This has been tested with success on several experimental set-ups.

The stroke of the SPU is limited to the distance between the magnetic poles of the magnetic circuit. This is caused by the fact that a standardised E-shaped core has been used. Redesign of the magnetic circuit and commutation of the current through the secondary coils will result in a larger stroke.

The SPU uses no commutation for the linear motor in propulsion direction. This makes the design easy and allows for the usage of simple control and amplifiers. By using some method of commutation, the stroke will be enhanced, but the electronic design will be more complex.

The SPU needs a set of wires leading to the supported mass. These wires must be flexible or loose, for they may not influence the contact free operation principle.

The limit of accuracy in suspension direction of the SPU has not yet been reached. Research done by de Veer [60] has shown that in the suspension direction a position stability of 5 nm can be reached when using a better sensor.

In this additional research a Heidenhain Exposed Incremental Encoder was used. This confirms the statement of Slocum [59] referred to in Section 3.9.

In general, a magnetic bearing has unequalled characteristics that make it a very promising candidate for positioning in high-accuracy systems. Not only the contact free principle of operation, but also the continuously adjustable bearing characteristics contribute to its uniqueness.

The magnetic suspension function of the SPU works properly. Even when a propulsion force is generated.

Application of three SPU's leads to an $XY\Phi$ stage with magnetic suspension and magnetic propulsion.

The scaling factors help to understand the behaviour of the SPU. Together with the design rules given in Chapter 8, a working SPU can be built with any desired dimensions.

Classical methods of control are sufficient for most applications of the SPU. It will be interesting to apply modern control strategies to the SPU in order to enhance its performance.

Precise knowledge of all the parameters of the SPU is not essential. The PID controller shows quite some robustness to parameter changes. Measurement of parameters and correction of the controller settings will enhance the overall system performance.

The quality of the sensors is of great importance on the achievable position accuracy. Both the minimum resolution and the signal/noise ratio determine the final accuracy of the closed loop system.

A compromise must be found for the supply voltage of an amplifier: A high supply voltage results in a high slew rate (desirable) but in a low efficiency for linear amplifiers (undesirable) and a high current ripple for switching amplifiers (very undesirable).

Much can be said about the scaling of magnetic forces, but the fact remains that the application of the force dictates whether scaling down is of positive or negative effect on the required system characteristics.

A very important feature of the developed Suspension and Propulsion Unit (SPU) can be found in the fact that it contains no accurately machined parts. This

will make the SPU competitive with conventional guiding elements with sub-micrometer accuracy.

9.2 Recommendations

A few recommendations are given here for future research in the SPU.

The amplifier plays a very important role in the SPU. When higher accuracy is sought, the need for better sensors will be obvious, but a better amplifier will be needed too. The current amplifier design used for this research operates satisfactorily for micrometer accuracy applications, but must be enhanced for higher accuracy aims.

Unmodelled high frequency oscillations occur in every design. These oscillations are introduced by, either eigenfrequencies of the support structure, or by eigenfrequencies of the supported mass. The influence of unmodelled high frequency oscillations can be reduced by designing support structures with high stiffness and subsequently high eigenfrequencies, or by incorporating the mechanism into the controller. Cooperation with experts in the field of control engineering is advised when a model the high frequency oscillations are incorporated into magnetic bearing model.

Research in different winding techniques, both for the suspension direction and for the propulsion direction, is needed if more optimal designs are to be made. The implementation in this thesis of a set of differentially wound coils with equal amount of windings has performed well, but does not reflect an optimal design.

The wires that lead to the supported mass of the SPU (necessary to provide the secondary coils with current) can not easily be removed. Investigation in methods of contact free energy supply to the rotor is not recommended. Instead, the SPU is meant for applications with limited stroke only. For long-stroke applications, a different propulsion method with permanent magnets on the rotor for instance, may be considered.

The fact that the secondary windings are made of copper automatically leads to a large air-gap. This air-gap can be reduced if the copper windings are replaced by windings made of a high permeability material. Preliminary experiments conducted at the Laboratory for Micro Engineering indicate that a propulsion force can be generated, but the effect of the high permeability material on the suspension characteristics must be further researched.

10. References

- [1] ACTUATOR'94, 4th International Conference on New Actuators, 1994 AXON Technologie Consult GmbH, Bremen, 15-17 June 1994
- [2] Amik, A., Bui S.K., *A review of several methods for processing vibration data*, Vibration Control in Micro-electronics, Optics and Metrology, Proc. SPIE 1619, 1992, p. 253-264
- [3] Auer F., Beek H.F. van, *Combined Linear Propulsion and Suspension Using a Single Active Magnetic Bearing Unit*, Proceedings of MAG'93 Magnetic Bearings, Magnetic Drives and Dry Gas Seals, July 29-30, 1993, p. 74-84
- [4] Auer F., Beek H.F. van, *Practical Application of a Magnetic Bearing and Linear Propulsion Unit for Six Degrees of Freedom Positioning*, MAG'94, Fourth International Symposium on Magnetic Bearings, Proceedings, August 1994, p. 183-188
- [5] Auer F., Beek H.F. van, *A Linear Active Magnetic bearing Unit for Combined (Frictionless) Suspension and Propulsion*, ACTUATOR'94, 4th International Conference on New Actuators, 1994, p. 66-60
- [6] Auer F. et al., *XYΦ Stage with Nanometer Accuracy, Using Magnetic Bearing Actuators for Positioning*, Proceedings of MAG'95, Magnetic Bearings, Magnetic Drives and Dry Gas Seals, August 1995, p. 167-175
- [7] Auer F. et al., *A Magnetically Levitated, Six Degrees of Freedom High Accuracy Positioning System*, Proceedings of MAG'95, Magnetic Bearings, Magnetic Drives and Dry Gas Seals, August 1995, p. 176-185

- [8] Baatz M., Hyrenbach, *Method of Calculating the Magnetic Flux Density and Forces in Contact-Free Magnetic Bearings*, ETEP Vol. 1, No. 4, July/August 1991, p. 195-199
- [9] Personal conversation with Professor H.F. van Beek
- [10] Bichsel J., *Beiträge zum Lagerlosen Elektomotor*, Dissertation ETH Nr. 9303 ETH Zürich, Switzerland, 1990 (in German)
- [11] Bleuler H., et al., *Micromachined Active Magnetic Bearings*, Fourth International Symposium on Magnetic Bearings, August 1994, p. 349-352
- [12] Bolton H., *An Electromagnetic Bearing*, Source unknown
- [13] Bonnema G.M., *Design of an XY-($\Phi=0$) Stage with Sub-micrometer Resolution*, Laboratory for Micro Engineering, Delft University of Technology, 1995
- [14] Bonse, J.E., *Linear Displacement Interferometers*, Laboratory for Micro Engineering, Delft University of Technology, S03/B21, 1995
- [15] Bonse M.H.W., *Capacitive Position Transducers; Theoretical Aspects and Practical application*, Dissertation Delft University of Technology, To be published
- [16] Bornstein K.R., *Dynamic Load Capabilities of Active Electromagnetic Bearings*, Transactions of the ASME, Vol. 113, July 1991, p. 598-603
- [17] Braunbek W., *Freischwebende Körper im Elektrischen und Magnetischen Feld*, Z. Phys. Bd. 112, 1939, p. 753-763
- [18] Cool J.C. et al., *Regeltechniek*, Delta Press B.V., ISBN 90-6674-002-7, 1985 (in Dutch)
- [19] Coren R.L., *Basic Engineering Electromagnetics, An applied approach*, Prentice Hall, Englewood Cliffs, N.J. 07632, ISBN 0-13-060369-4, 1989
- [20] Cox H.H.M., *Aktieve Magneetlagering: Toepassing in een Precisierechtegeleiding*, Eindhoven University of Technology, 1991 (in Dutch)
- [21] Earnshaw, S., *On the Nature of the Molecular Forces which regulate the constitution of the lumiferous ether*, Trans. Camb. Phil. Soc. 7, 1842, p. 97-112

- [22] Eisenhaure D., Hockney R., *Magnetic Bearings for Precision Linear Slides*, Proceedings of the First International Symposium on Magnetic Bearings, ETH Zurich, 1988, p. 67-79
- [23] ELMO Motion Control Ltd., SSA-series amplifier reference manual
- [24] Encyclopedia Britannica USA, Instant Research Service, *Linear Motors*
- [25] Harner L.L., Dietrich D.W., Masteller M.S., *An Overview of Soft Magnetic Materials for Magnetic Bearings*, Proceedings of MAG'93 Magnetic Bearings, Magnetic Drives and Dry Gas Seals, July 29-30, 1993, p. 141-150
- [26] Heidenhain, *NC linear encoders*, Catalog April 1994
- [27] Herzog R., *Ein Beitrag zur Regelung von Magnetgelagerten Systemen mittels positiv reeler Funktionen und Hoo - Optimierung*, Dissertation ETH Nr. 9399 ETH Zürich, Switzerland, 1991 (in German)
- [28] Higuchi T., et al., *Super-clean actuator for machines and robots*, IECON'87 Motor control and power electronics, 1987 International conference on industrial electronics, control and instrumentation, 1987
- [29] Jayawant B.V., Rea D.P., *New electromagnetic Suspension and its Stabilisation*, Proceedings of the IEE, Vol. 115, No. 4, April 1968, p. 549-554
- [30] Jin J., Higuchi T., *Dynamics and Stabilisation of Magnetic Suspension using Tuned LC Circuit*, Fourth International Symposium on Magnetic Bearings, August 1994, p.321-326
- [31] Kaplan B.Z., *Analysis of a method for Magnetic Levitation*, Proceedings of IEE, Vol. 114, No. 11, November 1967, p. 1801-1804
- [32] Kooij v.d. J.M., *Realisatie van een XYΦ-tafel, gebaseerd op de Suspension and Propulsion Unit*, Laboratory for Micro Engineering, Delft University of Technology, 1995 (in Dutch)
- [33] Personal conversation with Professor M.P. Koster
- [34] Kuijk van J., *Lineaire elektromotoren*, Laboratory for Micro Engineering, Delft University of Technology, K15, 1990 (in Dutch)

- [35] Kuzin A., Holmes M., Trumper D.L., *Analysis of the Control System for a Precision Magnetically Suspended Six-Degree-of-Freedom Motion Control Stage*, Source unknown
- [36] Laithwaite E. R., *Transport without wheels*, Westview Press Boulder, Colorado, 1977
- [37] Laithwaite E. R., *Linear electric machines - a personal view*, Proceedings of the IEEE, vol. 63, no. 2, February 1975, p. 250-290
- [38] Lange de J., *Lineaire motoren*, Laboratory for Micro Engineering, Delft University of Technology, L13-S045, 1994 (in Dutch)
- [39] Larssonneur R., *Design and Control of Active Magnetic Bearing Systems for High Speed Rotation*, Dissertation ETH Nr. 9140 ETH Zürich, Switzerland, 1990
- [40] Lazeroms, M.C.J., *One dimensional micro-positioning system based on magnetic bearings*, Laboratory for Micro Engineering, Delft University of Technology, A034-L12, 1994
- [41] Lorrain P., et al., *Electromagnetic fields and waves*, W.H. Freeman and Company 0-7167-0331-9, 1988
- [42] Luda G., *Drehstom Asynchron Linearantriebe*, Wurzburg, Vogel, 1981 (in German)
- [43] *Magnetic Bearings: A short course*, Introductory course in magnetic bearings, presented at MAG'93
- [44] Proceedings of MAG'95 Magnetic Bearings, Magnetic Drives and Dry Gas Seals, Conference and Exhibition, Technomic Publishing Co., August 10-11, 1995
- [45] Maslen E.H., et al., *Permanent Magnet Biased Active Magnetic Bearings*, Proceedings of the First International Symposium on Magnetic Bearings, ETH Zurich, Switzerland, June 6-8, 1988, p. 117-128
- [46] Maslen E.H., et al., *Practical Limits to the Performance of Magnetic Bearings: Peak Force, Slew Rate, and Displacement Sensitivity*, Journal of Tribology, April 1989, Vol. 111, p. 331-336

- [47] Monteiro A.F., et al., *A Super-Precision Linear Slideway with Angular Correction in Three Axis*, Proceedings of the 8th International Precision Engineering Seminar, Compiègne, France, May 1995, p. 525-528
- [48] Moon F.C., *Magneto-solid mechanics*, Wiley-Interscience, New York, ISBN 0-471-88536-3, 1984
- [49] Nagaya K., Arai N., *Analysis of a Permanent Magnet Levitation Actuator with Electromagnetic Control*, Transactions of the ASME, Journal of dynamic systems, measurement and control, Vol. 113, no. 3, September 1991, p. 472-478
- [50] Nasar S.A., Boldea I., *Linear motion electric machines*, John Wiley & Sons, ISBN 0-471-63029-2, 1976
- [51] O'Connor L., *Active Magnetic Bearings give Systems a Lift*, Mechanical Engineering, July 1992, p. 52-57
- [52] Oka K., Higuchi T., *Magnetic Suspension System with Permanent Magnet Motion Control*, MAG'94, Fourth International Symposium on Magnetic Bearings, Proceedings, 1994, p. 131-137
- [53] Schweitzer G., Bleuler H., Traxler A., *Active Magnetic Bearings, Basics, Properties and Applications of Active Magnetic Bearings*, Hochschulverlag AG an der ETH Zürich, ISBN 3-7281-2132-0, 1994
- [54] Sebestyen I., *Analysis and Measurement of Ball Screw Drives*, Proceedings of the 8th International Precision Engineering Seminar, Compiègne, France, May 1995, p. 302-305
- [55] Siegwart R., et al., *Eddy Current Bearings for Micro-Structure Levitation*, MAG'94, Fourth International Symposium on Magnetic Bearings, Proceedings, 1994, p. 359-363
- [56] Siegwart R., *Aktive magnetische Lagerung einer Hochleistungs-Frässpindel mit digitaler Regelung*, Dissertation ETH Nr. 8962 ETH Zürich, Switzerland, 1989 (in German)
- [57] Slocum A.H., *Precision Machine Design*, Prentice Hall, ISBN 0-13-690918-3, 1992

- [58] Sortore C.K., et al., *Permanent Magnet Biased Magnetic Bearings - Design, Construction and Testing*, Proceedings of the First International Symposium on Magnetic Bearings, ETH Zurich, Switzerland, June 6-8, 1988, p. 175-182
- [59] Studer P.A., *A practical Magnetic Bearing*, IEEE Transactions on Magnetics, Vol. MAG-13, No. 5, September 1977, p. 1155-1156
- [60] Thronton R.D., *Magnetic Levitation and Propulsion, 1975*, IEE Transactions on Magnetics, Vol. MAG-11, no. 4, July 1975, p. 981-995
- [61] Tomita Y., et al., *Precise Positioning Mechanism with Surface Motor*, Source unknown
- [62] Traxler A., *Eigenschaften und auslegung von Berührungsfreien Elektromagnetischen Lagern*, Dissertation ETH Nr. 7851, ETH Zürich, Switzerland, 1986 (in German)
- [63] Personal conversation with D.L. Trumper, during MAG'94 conference
- [64] Trumper D.L., Queen M.A., *Precision Magnetic Suspension Linear bearing*, NASA International Symposium on Magnetic Suspension Technology, NASA Langley Research Center, Hampton, VA, August 19-23, 1991
- [65] Trumper D.L., Slocum H.S., *Five Degree-of-Freedom control of an Ultra-Precision Magnetically-Suspended Linear Bearing*, NASA International Symposium on Magnetic Suspension Technology, NASA Langley Research Center, Hampton, VA, September 25-27 1990
- [66] Veer B. de., *XYΦ manipulator met sub-micrometer nauwkeurigheid gebaseerd op elektromagnetische reluctantie actuatoren*, Laboratory for Micro Engineering, Delft University of Technology, V8-A050, 1995 (in Dutch)
- [67] Vegte J. van de, *Feedback control systems*, Prentice Hall, ISBN 0-13-313495-4, 1990
- [68] Vischer D., *Sensorlose und Spannungsgesteuerte Magnetlager*, Dissertation ETH nr. 8665, Zurich, 1988 (in German)
- [69] Vullings H.J.L.M., *Enkelzijdige magneetlagering*, Laboratory for Micro Engineering, Delft University of Technology, V7-A038, 1994 (in Dutch)

- [70] Willigen de R., *Magnetische Materialen: Belangrijke eigenschappen voor magnetische lagers*, Laboratory for Micro Engineering, Delft University of Technology, W11-S040, 1994 (in Dutch)

Mathematical derivation of the closed loop transfer functions

In this appendix the closed loop transfer functions for the suspension and the propulsion directions of the SPU are calculated. The compliance transfer functions are also derived.

Figure A.1 shows the layout of the magnetic actuator. The system is represented by a closed loop servo system, with a controller, an amplifier, a proces and a sensor. The representation can be for either the suspension direction or for the propulsion direction.

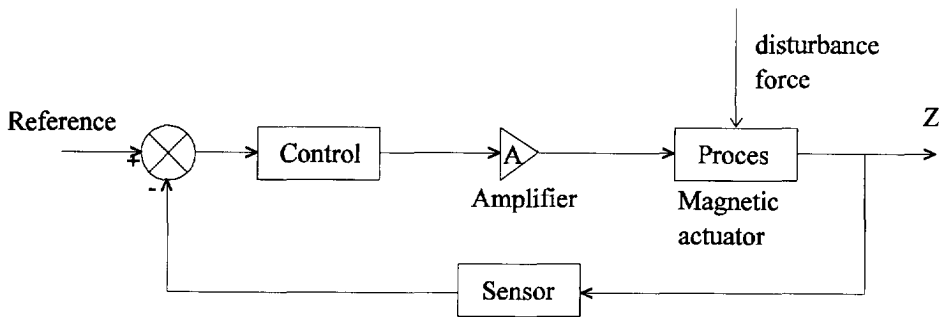


Fig. A.1 Block diagram representing the closed loop Suspension and Propulsion Unit. The block diagram is identical for both the suspension and the propulsion direction.

The closed loop transfer function for the suspension of the SPU is given by:

$$H_{cl}(s) = \frac{H_c(s) \cdot K_a \cdot H_p(s)}{1 + H_c(s) \cdot K_a \cdot H_p(s) \cdot K_{sens}} \quad (A.1)$$

The compliance transfer function is:

$$C(s) = \frac{1/(ms^2 - K_c)}{1 + H_c(s) \cdot K_a \cdot H_p(s) \cdot K_{sens}} \quad (A.2)$$

where

$H_c(s)$ = controller transfer function,

$H_p(s)$ = proces transfer function,

K_a = amplifier gain, and

K_{sens} = sensor gain.

The transfer function of the controller, a Lead-Lag filter, is:

$$H_c(s) = P \cdot \frac{(\tau_i s + M_i)}{(\tau_i s + 1)} \frac{M_d(\tau_d s + 1)}{\tau_d s + M_d} \quad (A.3)$$

where

M_i = lag action index,

τ_i = integration time constant,

M_d = lead action index,

τ_d = derivative time constant, and

P = proportional gain.

The process transfer function of the magnetic bearing is derived from Equation (3.20) in Chapter 3:

$$H_p(s) = \frac{2K_i}{m \cdot s^2 - 2K_c} \quad (A.4)$$

Substitution of both Equation (A.3) and Equation (A.4) in Equation (A.1) results in:

$$H_{cl}(s) = \frac{P \cdot M_d \cdot 2K_i \cdot A \cdot (\tau_i s + 1) \cdot (\tau_d s + 1)}{(\tau_i s + 1) \cdot (\tau_d s + M_d) \cdot (m \cdot s^2 - 2K_c) + P \cdot M_d \cdot 2K_i \cdot A \cdot (\tau_i s + 1) \cdot (\tau_d s + 1) \cdot K_{sens}} \quad (A.5)$$

Calculation of all factors and rearranging leads to:

$$H_{cl}(s) = \frac{a_0 + a_1 s + a_2 s^2}{b_0 + b_1 s + b_2 s^2 + b_3 s^3 + b_4 s^4} \quad (3.32)$$

where

$$\begin{aligned} a_0 &= M_i \cdot P \cdot M_d \cdot 2K_i \cdot A \\ a_1 &= (\tau_i + \tau_d \cdot M_i) \cdot P \cdot M_d \cdot 2K_i \cdot A \\ a_2 &= \tau_i \cdot \tau_d \cdot P \cdot M_d \cdot 2K_i \cdot A \end{aligned} \quad (\text{A.6})$$

and

$$\begin{aligned} b_0 &= -M_d \cdot 2K_c + P \cdot M_d \cdot 2K_i \cdot A \cdot K_{sens} \cdot M_i \\ b_1 &= -2K_c \cdot (\tau_i \cdot M_d + \tau_d) + P \cdot M_d \cdot 2K_i \cdot A \cdot K_{sens} \cdot (\tau_d \cdot M_i + \tau_i) \\ b_2 &= M_d - 2K_c \cdot \tau_i \cdot \tau_d + P \cdot M_d \cdot 2K_i \cdot A \cdot K_{sens} \cdot \tau_i \cdot \tau_d \\ b_3 &= m \cdot (\tau_i \cdot M_d + \tau_d) \\ b_4 &= m \cdot \tau_i \cdot \tau_d \end{aligned} \quad (\text{A.7})$$

The closed loop compliance transfer function is found by substituting the value of K_i in the equations derived above with one. The compliance transfer function can be written as:

$$C(s) = \frac{c_0 + c_1 s + c_2 s^2}{b_0 + b_1 s + b_2 s^2 + b_3 s^3 + b_4 s^4} \quad (3.33)$$

where

$$\begin{aligned} c_0 &= M_d \\ c_1 &= \tau_i \cdot M_d + \tau_d \\ c_2 &= \tau_i \cdot \tau_d \end{aligned} \quad (\text{A.8})$$

The closed loop transfer function and the closed loop compliance function of the propulsion of the SPU are found by substituting the suspension transfer function (A.4) by the propulsion transfer function:

$$H_x(s) = \frac{K_M}{m \cdot s^2} \quad (\text{A.9})$$

This leads to the closed loop transfer function for propulsion:

$$H_{cl}(s) = \frac{d_0 + d_1 s + d_2 s^2}{e_0 + e_1 s + e_2 s^2 + e_3 s^3 + e_4 s^4} \quad (4.14)$$

and the closed loop compliance transfer function for propulsion:

$$C(s) = \frac{f_0 + f_1 s + f_2 s^2}{e_0 + e_1 s + e_2 s^2 + e_3 s^3 + e_4 s^4} \quad (4.15)$$

where

$$\begin{aligned} d_0 &= M_i \cdot P \cdot M_d \cdot 2K_m \cdot A \\ d_1 &= (\tau_i + \tau_d \cdot M_i) \cdot P \cdot M_d \cdot 2K_m \cdot A \\ d_2 &= \tau_i \cdot \tau_d \cdot P \cdot M_d \cdot 2K_m \cdot A \end{aligned} \quad (A.10)$$

and

$$\begin{aligned} e_0 &= P \cdot M_d \cdot 2K_m \cdot A \cdot K_{sens} \cdot M_i \\ e_1 &= P \cdot M_d \cdot 2K_m \cdot A \cdot K_{sens} \cdot (\tau_d \cdot M_i + \tau_i) \\ e_2 &= M_d P \cdot M_d \cdot 2K_m \cdot A \cdot K_{sens} \cdot \tau_i \cdot \tau_d \\ e_3 &= m \cdot (\tau_i \cdot M_d + \tau_d) \end{aligned} \quad (A.11)$$

and

$$\begin{aligned} f_0 &= M_d \\ f_1 &= \tau_i \cdot M_d + \tau_d \\ f_2 &= \tau_i \cdot \tau_d \end{aligned} \quad (A.12)$$

Placement of the integration action in the controller

This appendix shows how the important control design parameter K_{di} can be found. Figure B.1 through Figure B.4 show four sets of curves for different M_d . Vertically the phase-loss for different values of K_{di} is shown, while horizontally the value of M_i is shown.

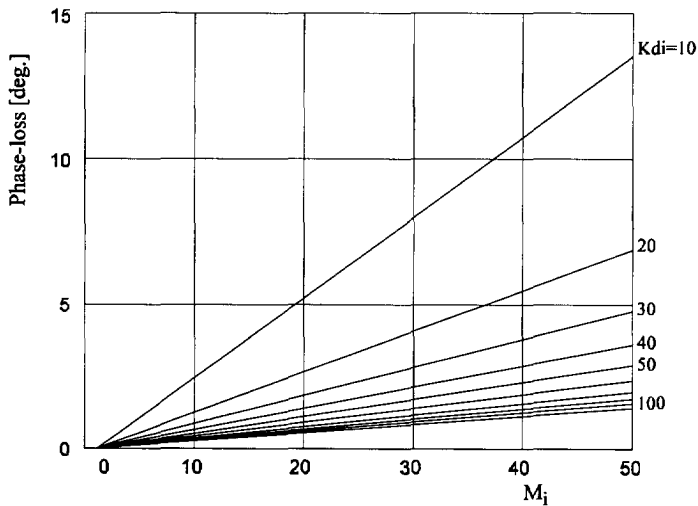


Fig. B.1 The phase-loss caused by the integrating action at the cross-over frequency for $M_d = 10$. Too much phase-loss ($>5\%$) will result in poor damping of the closed loop response of the magnetic bearing.

Selecting the appropriate Figure and looking up the permitted phase loss and the calculated M_i will lead to a value for the K_{di} .

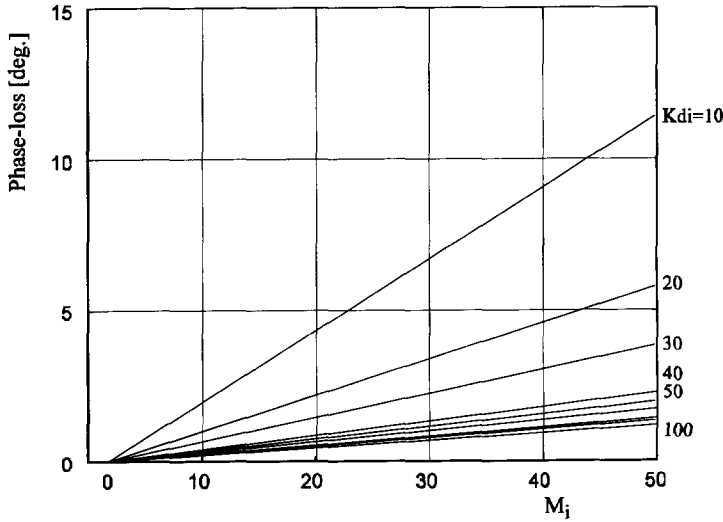


Fig. B.2 The phase-loss caused by the integrating action at the cross-over frequency for $M_d = 15$. Too much phase-loss ($>5\%$) will result in poor damping of the closed loop response of the magnetic bearing.

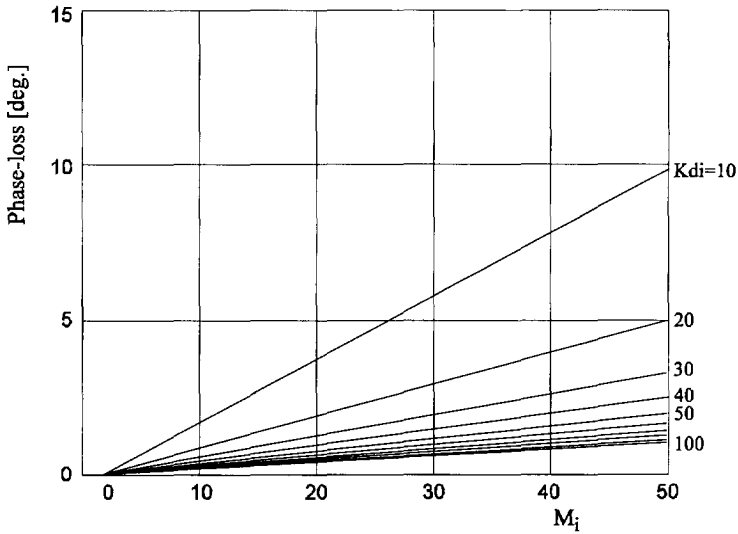


Fig. B.3 The phase-loss caused by the integrating action at the cross-over frequency for $M_d = 20$. Too much phase-loss ($>5\%$) will result in poor damping of the closed loop response of the magnetic bearing.

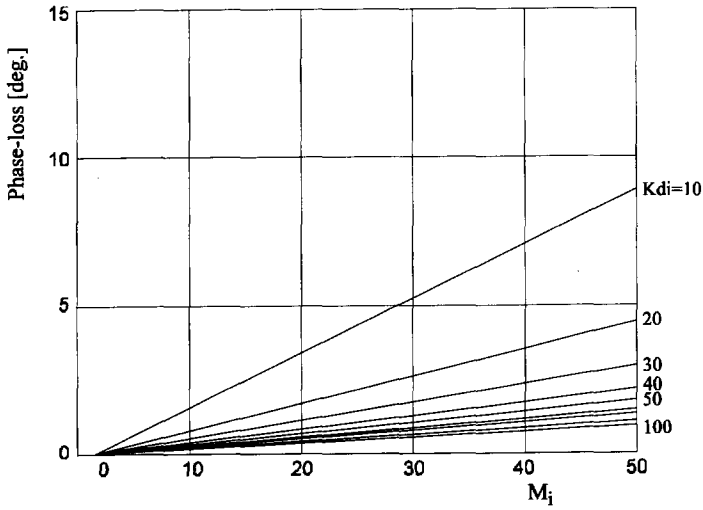


Fig. B.4 The phase-loss caused by the integrating action at the cross-over frequency for $M_d = 25$. Too much phase-loss ($>5\%$) will result in poor damping of the closed loop response of the magnetic bearing.

Derivation of the transformation matrices

This Appendix describes the transformation matrices used for obtaining the modal controller transfer functions of the experimental set-up described in Chapter 7. The transformations matrices must transform:

- the eddy current sensor information in to $Z\Psi\xi$ modal coordinates (transformation T1),
- the capacitive sensor information into $XY\Phi$ modal coordinates (transformation T2),
- the controller outputs into currents I_1 , I_2 and I_3 through the primary coils (transformation T3), and
- the controller outputs into the currents I_4 , I_5 and I_6 through the secondary coils (transformation T4).

Figure 7.5 shows where the transformation matrices are placed within the overall controller layout.

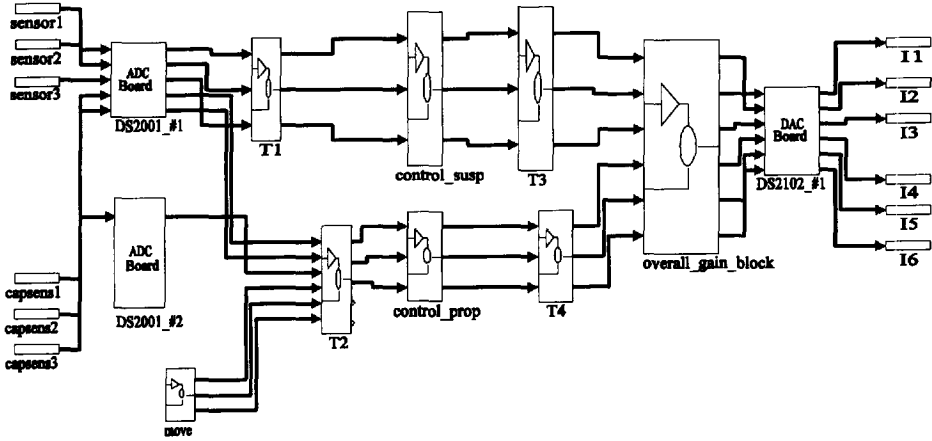


Fig. 7.5 Overview of the controller with conversion matrices for the modal control of the six degrees of freedom positioning system.

The eddy current sensor information is transformed into $Z\Psi\xi$ information using Figure C.1.

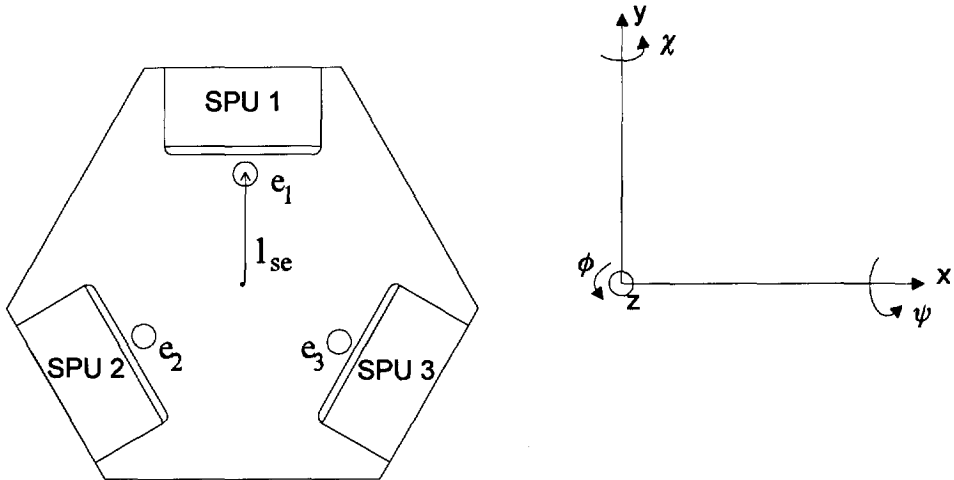


Fig. C.1 Derivation of the transformation matrices $T1$ and $T3$.

The eddy current information can be written as:

$$\begin{aligned}
e_1 &= z + l_{se}\Psi \\
e_2 &= z - \frac{1}{2}l_{se}\Psi + \frac{1}{2}\sqrt{3}\xi \\
e_3 &= z - \frac{1}{2}l_{se}\Psi - \frac{1}{2}\sqrt{3}\xi
\end{aligned} \tag{C.1}$$

or

$$\begin{bmatrix} e_1 \\ e_2 \\ e_3 \end{bmatrix} = \begin{bmatrix} 1 & l_{se} & 0 \\ 1 & -\frac{1}{2}l_{se} & \frac{1}{2}\sqrt{3}l_{se} \\ 1 & -\frac{1}{2}l_{se} & -\frac{1}{2}\sqrt{3}l_{se} \end{bmatrix} \tag{C.2}$$

Taking the inverse of the matrix in Equation (C.2) gives:

$$Tl = \begin{bmatrix} \frac{1}{3} & \frac{1}{3} & \frac{1}{3} \\ \frac{3}{2} & \frac{-1}{3} & \frac{-1}{3} \\ \frac{3l_{se}}{0} & \frac{3l_{se}}{\frac{1}{3}\sqrt{3}\frac{1}{l_{se}}} & \frac{3l_{se}}{-\frac{1}{3}\sqrt{3}\frac{1}{l_{se}}} \end{bmatrix}$$

with

l_{se} = the distance of the eddy current sensor to the center of the platen.

The capacitive sensor information is transformed into $XY\Phi$ information using Figure C.2.

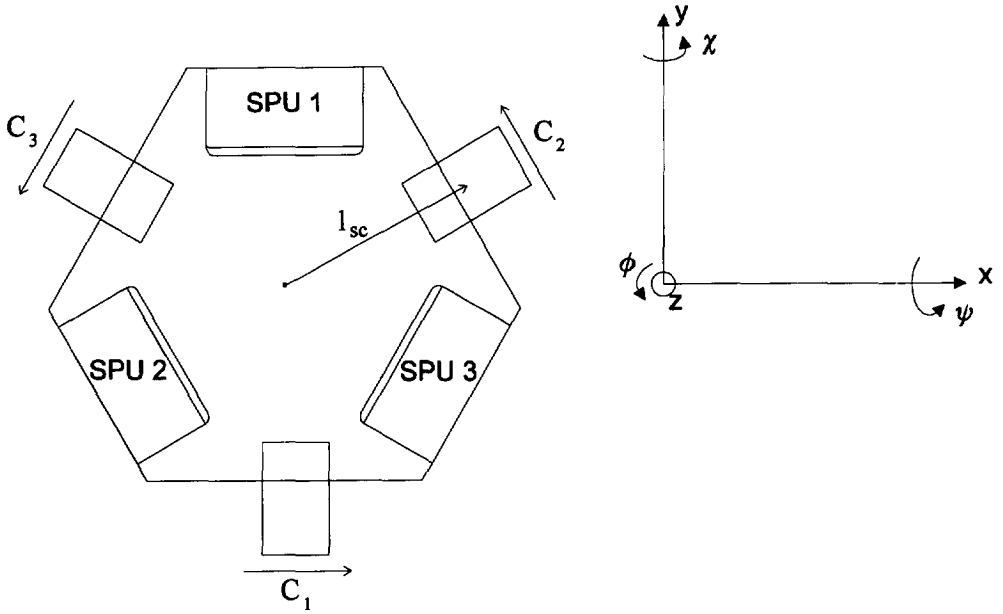


Fig. C.2 Derivation of the transformation matrix T2.

$$\begin{aligned}
 x &= c_1 - \frac{1}{2}c_2 - \frac{1}{2}c_3 \\
 y &= \frac{1}{2}\sqrt{3}c_2 - \frac{1}{2}\sqrt{3}c_3 \\
 \Phi &= \frac{1}{l_{sc}} \cdot (c_1 + c_2 + c_3)
 \end{aligned} \tag{C.3}$$

or

$$T2 = \begin{bmatrix} 1 & -\frac{1}{2} & -\frac{1}{2} \\ 0 & \frac{1}{2}\sqrt{3} & \frac{1}{2}\sqrt{3} \\ \frac{1}{l_{sc}} & \frac{1}{l_{sc}} & \frac{1}{l_{sc}} \end{bmatrix}$$

with

l_{sc} = the distance from the capacitive sensor to the center of the platen.

The transformation matrix that converts the control currents into the primary coil currents, T3, is the inverse of matrix T1. The non-co-location of the sensor with the SPU is compensated for by replacing the distance l_{se} with the force lever, l_{fr} :

$$T3 = \begin{bmatrix} 1 & l_{fr} & 0 \\ 1 & -\frac{1}{2}l_{fr} & \frac{1}{2}\sqrt{3}l_{fr} \\ 1 & -\frac{1}{2}l_{fr} & -\frac{1}{2}\sqrt{3}l_{fr} \end{bmatrix}$$

Using Figure C.3, the last transformation matrix, T4, is derived.

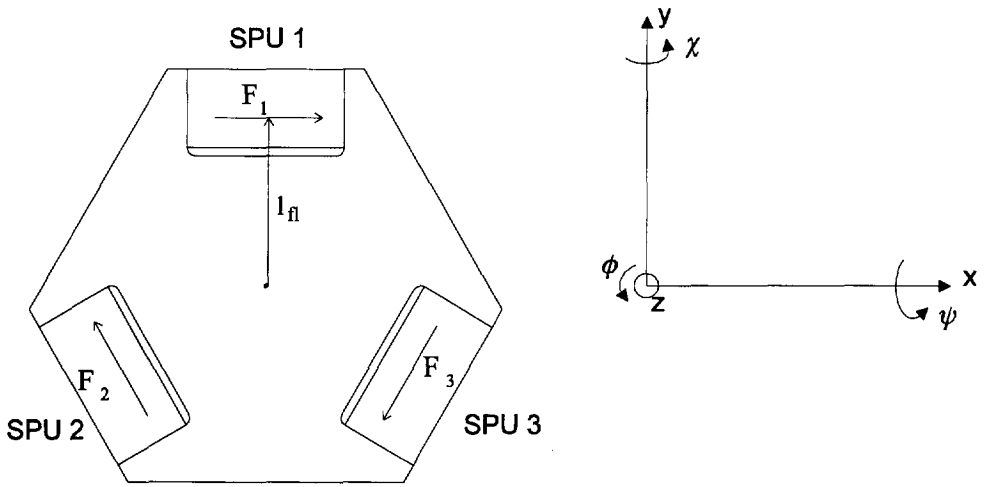


Fig. C.3 Derivation of the transformation matrix T4.

Using:

$$\begin{aligned} F_x &= -F_1 + \frac{1}{2}(F_2 + F_3) \\ F_y &= -\frac{1}{2}\sqrt{3}F_2 + \frac{1}{2}\sqrt{3}F_3 \\ M &= l_{fr} \cdot (F_1 + F_2 + F_3) \end{aligned} \tag{C.4}$$

The current is proportional to the force, so Equation (C.4) can be rewritten into:

$$\begin{bmatrix} I_x \\ I_y \\ I_\Phi \end{bmatrix} = \begin{bmatrix} -1 & \frac{1}{2} & \frac{1}{2} \\ 0 & -\frac{1}{2}\sqrt{3} & \frac{1}{2}\sqrt{3} \\ l_f & l_f & l_f \end{bmatrix} \begin{bmatrix} I_1 \\ I_2 \\ I_3 \end{bmatrix} \quad (\text{C.5})$$

Taking the inverse of the matrix in Equation (C.5) gives T4:

$$T4 = \begin{bmatrix} -\frac{2}{3} & 0 & \frac{1}{3l_f} \\ \frac{1}{3} & -\frac{1}{3}\sqrt{3} & \frac{1}{3l_f} \\ \frac{1}{3} & \frac{1}{3}\sqrt{3} & \frac{1}{3l_f} \end{bmatrix}$$

Combined Electromagnetic Suspension and Propulsion for Positioning with sub-Micrometer Accuracy

Summary

Magnetic bearings are actively controlled bearings with a rapid growth in applications. Digital control hardware that is now commercially available is fast and accurate and power electronics is cheap and powerful enough for magnetic bearings.

The operation principle of a magnetic bearing for linear movement is very simple. Two E-core shaped electromagnets are placed opposite to each other and an I-core shaped "rotor" is placed between them. A current flowing through the coils on the E-core electromagnets generates a magnetic field and thus exerts forces on the rotor. By measuring the position of the rotor and by controlling the current through the coils, the system is stabilized and its desired characteristics are established.

The contact free actively controlled principle of operation of the magnetic bearings provides for the following, characteristics:

- absolutely no friction or wear,
- low energy loss at high operation speeds, and
- adjustable bearing characteristics.

This thesis treats the design of a Suspension and Propulsion Unit (SPU), where suspension is obtained with a magnetic bearing, and propulsion is added by means of a linear motor. The two functions of the SPU:

- suspension of a mass in one degree of freedom, and
- propulsion of a mass in a degree of freedom, perpendicular to the direction of suspension,

are created within one SPU using only one magnetic field. The accuracy achieved is less than micrometer, depending on the signal to noise ratio of the sensors used in the SPU.

The magnetic bearing is controlled like a closed loop servo system. Four elements can be found in the loop: a sensor, a controller, an amplifier and a magnetic circuit. The resulting closed loop controlled active magnetic bearing

behaves like a mass-spring-damper system, where all characteristics are controlled by a tame PID controller.

The magnetic bearing characteristics can be tuned by means of a digital controller within the following ranges:

- bearing load capacity: from a few grams up to multi-ton loads,
- bearing stiffness: between 0 and 10^8 N/m, and
- relative damping: between 0 and 5.

A propulsion force is applied to the suspended mass by means of a Lorentz force. A set of coils is wound around the I-core and a current flowing through it interacts with the magnetic field of the suspension. The generation of this magnetic field, with a set of differentially wound coils carrying static and control current, results in a very low coupling between the suspension and the propulsion forces.

The positioning system is realized by adding a sensor and a feedback loop. Thus, a servo controlled positioning system is obtained. An experimental set-up consisting of one SPU has the following characteristics:

- bearing load capacity: 700 g,
- bearing stiffness: 10^6 N/m,
- damping: $\beta = 0.7$,
- bearing position inaccuracy: 1 μm ,
- propulsion force: 5 N,
- propulsion positioning inaccuracy: 1 μm , and
- closed loop bandwidth: 100 Hz.

Performed simulations and measurements show very good resemblance.

The sensors form an important part in the SPU. An overview of contact-free sensors, including inductive, eddy-current, capacitive, optical and form standard sensors is given. Eddy-current sensors are used in the suspension direction, while capacitive sensors are used in the propulsion direction.

Two types of amplifiers can be chosen for the SPU: linear amplifiers, showing a high accuracy but a low efficiency, and switching amplifiers with a high efficiency and a low accuracy. The current ripple produced by switching amplifiers limits the accuracy in both the propulsion and the suspension force, and is therefore not used in this research.

A link between simulation and experiment can be made with dSpace. dSpace is a digital control system with a highly developed interface to Matlab and Simulink. The DSP-based controller available in the laboratory has been used to obtain all the data measured.

A six degrees of freedom, magnetically suspended and propelled $XY\Phi$ stage was built in order to show the practical applicability of the SPU. Three SPU's are combined to form the $XY\Phi$ stage. Tuning of the position in the suspension direction can be done with the SPU's along a range of 1 mm in vertical (suspension) direction and 10 mm in the horizontal (propulsion) direction.

The last part of this thesis concentrates on the scaling factors of magnetic forces. It is shown that downscaling affects the uncontrolled negative stiffness and poles of the magnetic bearing. This results in a controller with higher bandwidth. The forces scale with S^2 , both for suspension and propulsion, but the mass scales with S^3 , resulting in a positive effect on the accelerations that influence the object in the suspension and in the propulsion direction.

Finally a set of seven consecutive design rules is described. Using these rules, all the mechanical properties of the SPU can be designed, meeting the specifications of the designer.

Frank Auer

Magnetische Lagering en Aandrijving, gecombineerd in één Element voor Positioneren met sub-Micrometer Nauwkeurigheid

Samenvatting

Magnetische lagers vallen in de categorie van de actief geregelde lagers en kenmerken zich door een grote groei aan toepassingen en toepassingsgebieden. Dit is voornamelijk te danken aan de recente ontwikkelingen op het gebied van de digitale regeltechniek (snellere computers en nauwkeurigere omzetting) en de vermogenselectronica (goedkoper en met meer vermogen).

Het werkingsprincipe van een magnetisch lager is zeer eenvoudig. Twee E-vormige elektromagneten staan tegenover elkaar en een I-vormige rotor bevindt zich daartussen. Een stroom door de spoelen van de E-magneten resulteert in een magnetisch veld dat krachten uitoefent op de rotor. Door de positie van de rotor te meten en door de stromen te sturen kan het systeem gestabiliseerd worden en krijgt het de gewenste eigenschappen.

Het actief gelagerde, kontakt vrije werkingsprincipe van magnetische lagers geeft de volgende, ongeëvenaarde eigenschappen aan het lager:

- geen wrijving en slijtage,
- laag energieverbruik bij hoge snelheden en
- regelbare lagering karakteristieken.

Dit proefschrift behandelt het ontwerp van de Suspension and Propulsion Unit (SPU), waarin de lagering is verkregen met een magnetisch lager en waarin een aandrijving is toegevoegd met een lineaire motor. De twee functies van de SPU:

- lagering van een massa in één graad van vrijheid en
- aandrijving van die massa in één graad van vrijheid, loodrecht op de lagerrichting,

zijn zo ontworpen dat zij binnen een 1 micrometer brede nauwkeurighedsband werken.

Het magnetisch lager wordt geregeld als een teruggekoppeld servo systeem. Vier onderdelen zijn te onderscheiden: een sensor, een regelaar, een versterker en

een magnetisch circuit. Het resulterende teruggekoppelde, actief geregelde magnetische lager gedraagt zich als een massa-veer-demper systeem waarvan alle eigenschappen met een tamme PID regelaar geregeld kunnen worden. De regelaar wordt digitaal geïmplementeerd.

De eigenschappen van het magnetische lager kunnen afgeregeld worden binnen de volgende bereiken:

- lager draagkracht: variërend van een paar gram tot een paar ton,
- lager stijfheid: tussen de 0 en de 10^8 N/m en
- relative damping: tussen de 0 en 5.

Een aandrijfkraft van het Lorentz-type wordt aan het magneetlager toegevoegd. Een set spoelen wordt rond de I-vormige rotor gewikkeld en een stroom door deze spoelen genereert een kracht in samenwerking met het aanwezige magneetveld. Het magneetveld wordt zodanig geregeld dat een sterke interactie tussen aandrijfkraften en lagerkrachten wordt voorkomen.

De aandrijfkraft wordt gebruikt om een positioneersysteem te creëren door een sensor en een terugkoppellus toe te voegen. Op die manier wordt een servo geregeld positioneersysteem verkregen. Een proefopstelling met de volgende eigenschappen is gebouwd:

- lager draagkracht: 700 g,
- lager stijfheid: 10^6 N/m,
- damping: $\beta = 0.7$,
- lager positie onnauwkeurigheid: $1 \mu\text{m}$,
- aandrijfkraft: 5 N,
- aandrijf positie onnauwkeurigheid: $1 \mu\text{m}$ en
- bandbreedte gesloten lus: 100 Hz.

Diverse simulaties zijn uitgevoerd en de resultaten komen goed overeen met verrichte metingen.

De sensoren vormen een belangrijk onderdeel van de SPU. Een overzicht van contactloze sensoren, waaronder inductieve-, wervelstroom-, capacatieve-, optische- en vormstandaardsensoren wordt gegeven. In de proefopstelling worden wervelstroomsensoren in de lagerrichting gebruikt, terwijl in de aandrijfrichting capacatieve sensoren worden toegepast.

Voor magneetlagers kunnen twee soorten versterkers worden gekozen: lineaire versterkers met hoge nauwkeurigheid en lage efficiëntie en schakelende versterkers met hoge efficiëntie en lage nauwkeurigheid. De stroomrimpel geproduceerd door de schakelende versterkers beperkt de maximaal haalbare nauwkeurigheid en deze versterker wordt in dit onderzoek niet gebruikt.

De koppeling tussen simulatie en experiment wordt verzorgd door dSpace. dSpace is een digitaal regelsysteem met een goed ontwikkelde interface naar MATLAB en SIMULINK. Het systeem is gebaseerd op een DSP processor en alle meetresultaten in dit proefschrift zijn verkregen met het dSpace-systeem zoals dat momenteel in het laboratorium beschikbaar is.

Een magnetisch gelagerd en aangedreven $XY\Phi$ -positioneersysteem is gebouwd om de praktische toepasbaarheid van de SPU te testen. Hiervoor zijn drie SPU's gebruikt die tezamen de zes graden van vrijheid van het systeem regelen. In de lagerrichting kan de SPU over een bereik van 1 mm worden geregeld, terwijl het bereik in aandrijfrichting 10 mm bedraagt.

Het laatste hoofdstuk gaat in op schaalfactoren voor magnetische krachten. Het neerschalen van de afmetingen heeft invloed op de negatieve stijfheid en de ongeregelde polen van het magneetlager. Dit resulteert in een regelaar met een hogere bandbreedte. De magneetkrachten schalen met S^2 , zowel voor de lagerrichting als voor de aandrijfrichting, maar de massa schaalt met S^3 , zodat het netto resultaat toch gunstig is.

Als laatste wordt een set ontwerpregels gegeven. Met behulp van deze regels kan een SPU in zeven opeenvolgende stappen, geheel naar specificatie van de ontwerper, worden gebouwd.

Frank Auer

Acknowledgements

The work presented in this thesis has had many contributors during the four years it took to write it.

The following people deserve some credit for this:

Jan van Eijk for making the whole project possible by financially supporting the research with money from Philips CFT, of the Nederlandse Philips Bedrijven B.V.,

Frank van Beek for his neverending support in technological and personal matters,

Sjao Ju Woo, Bert de Veer, Marc Lazeroms, Erik Vullings, Johannes de Lange, and Jos van der Kooij for their contributions too this research,

Jos deserves special credit for he has drawn most 3-D figures of this thesis.

Mario and Antonio, La Bamba for their fruitful discussions about real-world problems,

and especially

Suzan for comfort and stability at home.

Frank Auer
Delft, October 1995

Curriculum Vitae of the Author

I was born on October 16th 1967, in a small village called Leimuiden, but I grew up in Alphen aan den Rijn, The Netherlands. In Alphen aan den Rijn I attended primary school. In 1977 my parents moved to Madrid, Spain, and I finished primary school there. When we moved back to Alphen aan den Rijn in 1980, I had managed to finish the first year of high school at the international english school called Runneymede College. Back in Alphen aan den Rijn I finished high school in 1985. I started my technical career at the Delft University of Technology, department for Mechanical Engineering and Marine Technology in 1985. It took me six years to graduate at the university. During my graduation at the Laboratory for Micro Engineering, my interest in mechatronics grew, and I am glad to have been given the opportunity to do my PHD work on magnetic bearings, a very mechatronic product, at the Laboratory, under supervision of Professor van Beek.

Frank Auer
Delft, October 1995